AN ABSTRACT OF THE THESIS OF

Tsung-Wen Chen for the degree of Master of Science in Nuclear Engineering presented on May 29, 2019.

Title: A New Approach of Computational Fluid Dynamics Studying Power Transient Critical Heat Flux

Abstract approved:

_____
Wade R. Marcum

Power transient boiling has been studied for decades, however, the mechanistic understanding of phenomena which occur during such an event remains incomplete. Due to a dearth of systematic researches, the information of studied phenomenon, detailed physics and applicable hypothesis are very limited. Transient critical heat flux (CHF) is paramount in determining the safe operations of a nuclear reactor. The Transient Reactor Test Loop (TRTL), serves as an out-of-pile facility which supports the testing of conditions experienced in the Transient REActor Test (TREAT) facility at the Idaho National Laboratory (INL). Specifically, the TRTL was designed and operates with the focus on the power transient boiling phenomenon under the Pressurized Water Reactor (PWR) condition. Since the direct application of power transient experiments may lead to a potential safety concern, it is crucial to develop a Computational Fluid Dynamics (CFD) model and simulation method that provides a feasible way to recognize the irregular type of boiling processes that takes place in the TRTL facility and would therefore take place within the TREAT facility as well. With the expensive computational cost and heavy instability from the fast-changing boundary conditions and complicated two-phase physics, the available literature associated with studying transient boiling via CFD is limited. In this study, a new approach is developed with the consideration of heating and temporal behavior. An integral view of the CFD study includes model selection, grid independent study and stability maintenance. To develop a qualitatively confident result from the new approach, a brief data benchmark via available past experimental studies is provided. In addition, a new hypothesis which is able to solve the current debating of the transient boiling phenomenon based on the simulation is discussed as well.

A New Approach of Computational Fluid Dynamics
Studying Power Transient Critical Heat Flux

by
Tsung-Wen Chen

A THESIS

submitted to

Oregon State University

in partial fulfillment of
the requirements for the
degree of

Master of Science

Presented May 29, 2019
Commencement June 2020

Master of Science thesis of <u>Tsung-Wen Chen</u> presented on <u>May 29, 2019</u>.

APPROVED:

_____

Major Professor, representing Nuclear Engineering

_____

Head of the School of Nuclear Science & Engineering

_____

Dean of the Graduate School

I understand that my thesis will become part of the permanent collection of Oregon State University libraries. My signature below authorizes release of my thesis to any reader upon request.

_____

Tsung-Wen Chen, Author

ACKNOWLEDGEMENTS

TABLE OF CONTENTS

TABLE OF CONTENTS

TABLE OF CONTENTS

TABLE OF CONTENTS

LIST OF FIGURES

LIST OF FIGURES

LIST OF FIGURES

LIST OF FIGURES

LIST OF TABLES

A New Approach of Computational Fluid Dynamics Studying Power Transient Critical Heat Flux

1   INTRODUCTION

In any engineering industry safety is always crucial in the design considerations leading to successful operational outcomes. This is especially true in the nuclear industry. Different from other industries, the nuclear industry has assembled itself with some of the strictest safety standards. These strict standards and regulations have led the industry to become one of the safest within the energy vertical.

Nuclear Power Plants (NPPs) have one of the most reliable forms of sustained energy commercially available. The high power densities associated with this technology require an appropriate balance of heat removal under normal and off-normal operating conditions. The comprehensive and accurate understanding in thermal balance within a multiphase thermodynamic system and therefore the onset of conditions which lead to an imbalance is paramount to a reactor's safety. A traditional light water reactor relies heavily on convective heat removal during normal operation, however, if this is compromised phase change results and may lead to a departure from nucleate boiling (DNB). Departure from nucleate boiling refers to a change of the state from a liquid coolant phase cooling a heated structure via local nucleate boiling to a vapor coolant phase which 'blankets' the heated structure thereby reducing the heat removal rate and increases the temperature of the heat structure. The heat flux of said structure necessary to onset DNB is referred to as the critical heat flux (CHF). The result of this rapid increase in surface temperature commonly results in the mechanical failure of that structure and thereby compromises the integrity of the system.

Presently, a study is underway at Oregon State University (OSU) using a new experimental test loop referred to as the Transient Reactor Test Loop (TRTL) to identify and study the CHF which produces DNB during transient conditions relevant to light water reactors such as Reactivity Initiated Accident (RIA) scenarios. A RIA can occur when a control rod

within a NPP is ejected due to a mechanical or electrical malfunction. During a RIA, surface temperature of fuel rods suddenly increased due to the abrupt increasing change in reactivity within the core. The TRTL facility has been built to study transient CHF under representative thermal hydraulic conditions which would be experienced in an operating NPP. In the test section, a unique electrically-heated heater rod has been designed and developed to provide the representative heat generation needed for such a study.

In a RIA scenario, thermal power is generated in such a rapid form that the heat source is approximated to be an adiabatic system (with very little heat-loss); this results in the likelihood that fuel rods may approach their melt temperature limitation. The characteristic of the power pulse is determined by the unique cause of a RIA and, more crucial, maximum thermal power experienced during the transient. Typically, a transient is characterized by the pulse power's full width half maximum (FWHM) and can take place of the order of 50 *ms* or less and the amplitude of pulse (maximum power generation) can be up to the order of a thousand mega-joules. To simulate the pulse with extremely narrow FWHM and large amplitude, an exponential ramp pulse of power generation is adopted in TRTL in order to focus on the beginning of RIA (the rising power before attained maximum power output) where transient CHF phenomenon takes place. The power transient produced by TRTL can be less than 100 *ms* and result in similar linear heat generation rates to that in an NPP during a RIA.

The maximum operating temperature of TRTL can be up to 300 °*C*, and maximum operating pressure can be up to 2250 *psi*. Therefore, the use of the TRTL facility restricts the transient CHF phenomenon to occur within those operating conditions. This represents a challenge because mapping the comprehensive transient CHF phenomenon requires a close look at variations in both temperature and pressure. Furthermore, physically modifying any test facility to accommodate a different set of pressures and temperatures from its original operating conditions is a costly and time-consuming endeavor.

Computational Fluid Dynamics (CFD) studies are often employed as an alternative approach in acquiring a solution when compared against experimentation. CFD uses

established mathematical models to simulate the conditions experienced by the flow across many scenarios. Particularly, interactions within two phase flow for a broad range of pressures and temperatures can be simulated with an acceptable degree of accuracy. Star-CCM+ is a recognized CFD industry software and will be utilized throughout this work. It is intended that the output from the Star-CCM+ simulations be compared with future experimental data collected from TRTL in an effort to validate the CFD models implemented within the software package for transient CHF conditions.

1.1 Motivation

Presently, CHF correlations for quasi-steady state boiling have been developed and are commonly applied within many industry applications, however CHF phenomenon under transient scenario have yet to be well understood. In the nuclear industry, transient CHF phenomenon is key for the development of rigorous safety standards regarding the operation of nuclear reactors. Transient CHF describes the process of heat removal from the core which is crucial in preventing the fuel cladding from melting. The most prominent example involving failure to remove heat from the core includes the Chernobyl accident in 1986 which resulted in core melt-down and the release of radioactive material into the atmosphere. Studies revealed that the RIA scenario was the primary cause of failure. Understanding RIA-induced transient CHF is crucial and is also the motivation behind the TRTL. More specifically, this study will result in a credible CFD model which may represent the transient CHF phenomenon experienced at the TRTL facility. Once the model is validated, it may then be used to fill the gap between existing experimental studies across many pressures and temperatures.

The study of transient CHF through application of CFD is, however, not well developed for several reasons. First, the limitations from the nature of the CFD software, the complicated physics behind the two-phase flow and the dramatically changing of the boundary conditions due to the fast-transient phenomenon, lead to an extremely unstable process of the computation. Second, in order to provide a solution through use of most CFD software tools, the needed computational cost becomes extremely expensive and, in some cases, uneconomic. A standard process must be developed for the purpose of

balancing the computational cost and stability concern, especially, for the type of the simulation discussed in this study. In addition, with the limited number of the transient CHF studies during past decades, the transient heat generating, and removal is not well understood. This leads to a challenge in the fundamental validation of the solution from a CFD software package even if the simulating result is produced. It is suggested by several experimental studies that the mechanism behind the transient boiling is very different from quasi-steady state boiling. The algorithms and the models adopted by the CFD software is therefore needed to be verified and validated.

1.2   Objectives

The objective of this study is to develop a base-line approach for studying transient CHF by using the CFD software. The approach developed by this study may serve as a new standard for future CFD studies. In addition, the most credible CFD models feasible while utilizing Star-CCM+ are verified through application of best-practices, industry vetted verification and validation standards, parametric comparison of available models within the software package and the computational stability maintaining under the acceptable computational cost. These are accomplished through the following tasks:

- A comprehensive review of available literature including quasi-steady state and transient CHF. For quasi-steady state CHF, the models and correlations developed in past decades are compared and discussed. Meanwhile, the experiments and hypothesis for transient CHF revealing in the past are also completely discussed.

- A discussion of the simulating geometry and refinement method based on the TRTL facility is detailed for the purpose of demonstrating the basis and application of appropriate boundary condition setting.

- A detailed and logical approach to the down-selection of the most credible two-phase heat transfer models available within Star-CCM+ for the purpose of predicting transient CHF is presented. This results in a path to the development of this model and the outcome of the selected parameters chosen to support this model.

- An effort of maintaining the stability with respect to the unstable computational process offered by the complicated physics of two-phase models and the dramatically changing of the boundary condition is provided. The solutions of the

stability issue are developed under the consideration of balancing the computational cost.

- A grid independent study for several unique two-phase models is conducted. This is done in order to perform a complete effort on the refinement of the numerical spatial-temporal how grid and its influence on the solution resulting from the models.

- A comparison of model results to one another with qualitative discussion against how their results compare to limited available experimental data at present to develop a qualitative confidence of the predicted solutions.

- An indication of the most suitable setting of models, grid refinement, setting of boundary condition under the frame of Star-CCM+ by discussing the result from all the above-mentioned objectives and providing the simulation of detailed mechanism of two-phase heat transfer under micro scale which could not be measured experimentally.

2   SURVEY OF LITERATURE

There is an abundance of literature discussing detailed phenomenon occurring under the scope of CHF. The work herein focuses on deciding the proper models that are utilized within Star-CCM+ for the purpose of most accurately and credibly simulating transient CHF phenomenon. To achieve a better understanding of transient CHF phenomenon under two phase CFD simulation, this chapter will be organized in three topical areas:

- First, critical heat flux phenomenon. Critical heat flux is a thermal limit that causes a phase change of coolant on the heating surface. In a PWR, such phase change may lead to a fuel failure or even a leakage of radioactive material. The knowledge from the ordinary CHF may serve as a key to a better understanding of transient CHF and, thus, should be well discussed.

- Second, transient boiling. Transient boiling is referred to a boiling phenomenon introduced in a short period herein. One of the most significant differences between quasi-steady state boiling and transient boiling is the mechanism of CHF. The physics behind quasi-steady state CHF is reviewed herein. To achieve a more rigorous understanding of transient CHF, a review of those experiments corresponding to the transient boiling, especially the power type transient boiling is made.

- Third, two-phase computational fluid dynamics in CHF. Recently, CFD has become an important approach to acquire phenomenological information which is not available via experiments. However, CFD does have its own limit and should be discussed. While a solution may be feasible through use of a CFD package, the models that are applied to acquire the solution create a contentious discussion around their validity, particularly when investigating two phase problems by using of two-phase models. Therefore, those models related to this study and two-phase transport will be discussed.

2.1 Critical Heat Flux Phenomenon

Over the past few decades, several different theories on the prediction of and physics leading up to CHF have been postulated and a great number of studies about transient boiling have also been published. However, no study has yet to explain CHF perfectly. Regardless of the model developments to predict the CHF itself, a generally accepted relationship between all phases of boiling heat transfer is shown in Fig. 1. Specifically, Fig. 1 shows the "boiling curve" associated with low-pressure, quasi-steady state pool boiling (i.e. no, or insignificant hydrodynamic flow). From this figure one can see four unique regions and six unique characteristic points denoted A through F through the relation of the wall temperature (T_w) on the *x*-axis and the wall heat flux (q'') on the *y*-axis. Honing in on the regions and points of interest for this study one can see that at the end of nucleate boiling, transition boiling starts with CHF being reached (located at point *C*). Under these conditions, film boiling starts to be introduced locally on the heated surface. For a general case, when this occurs, it results in a rapid significant increase in the heated wall's surface temperature. It is this transition that is the focus of the study and one's ability to predict the heat flux (q'') needed to reach point *C* during a power transient.

Region AB: Natural convection
Point B: Onset of nucleate boiling (ONB)
Region BC: Nucleate boiling
Point C: Critical heat flux (CHF)
Region CD: Transition boiling
Region DE: Film boiling
Line CE: Superheat transition
Line DF: Subcooling transition
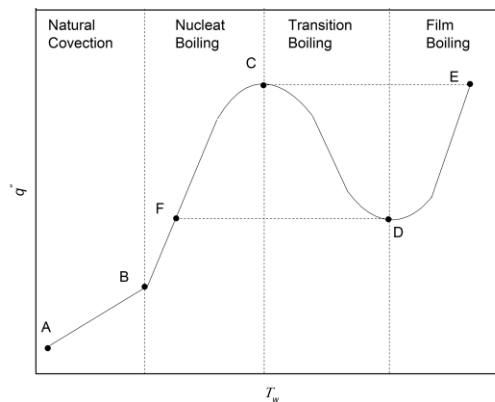
Fig. 1. Sketch of the pool boiling curve

2.1.1 Boiling Curve

The earliest boiling curve was proposed by (Nukiyama, 1934) and graphically resembled similar trends to that shown in Fig. 1. This first curve was empirically developed through

many experiments conducted in an atmospheric pool being heated with a 3 *mm* copper wire. During the experiment the glass pool was covered by sand and surrounded by another heater outside to keep the bulk water temperature near saturation. The result of Nukiyama's early experiments indicated that there is a maximum heater power (Q_{max}) which abruptly leads to a rise of approximately 20 to 30 °*C* on the heater wire. This Q_{max} was ultimately referred as CHF in later studies. However, the boiling curve proposed by Nukiyama terminated at Q_{max} (point *C* in Fig. 1). Following Nukiyama, (Drew &Muller, 1937) finished the curve by boiling carbon tetrachloride and comparing those results to that acquired by Nukiyama. The outcome of this was that steady film boiling curve was first provided and several speculations on the theory of film boiling were made.

2.1.2   Hydrodynamic Instability Models

Since these initial fundamental boiling studies were performed numerous efforts have been made to explain and predict pool boiling CHF. These have been done via theoretical approaches, empirical means and combinations thereof; most resulting in correlations or look-up charts which require one to input an appropriate set of known parameters to acquire the predicted critical heat flux. Phenomenologically, a separation of models developed over years of study. These models can be generally classified into two categories: Hydrodynamic instability (HI) models (Fig. 2) and macrolayer/sublayer dryout/thinning models (Fig. 3).
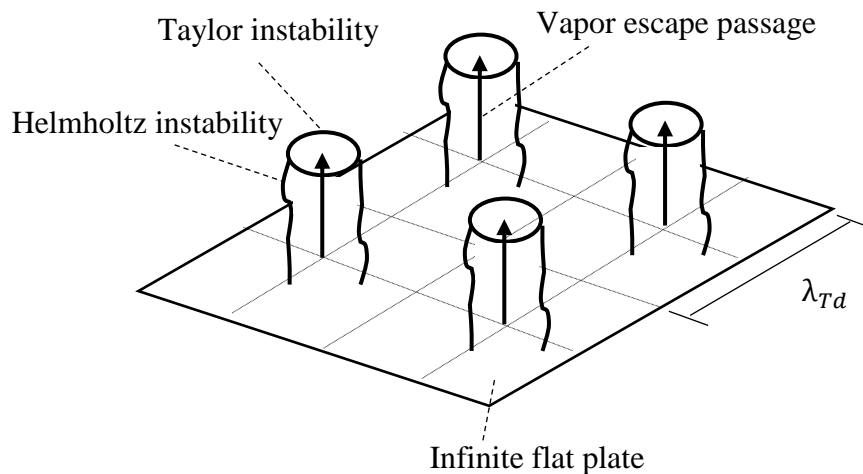
Fig. 2. Illustration of the hydrodynamic instability model [Zuber]
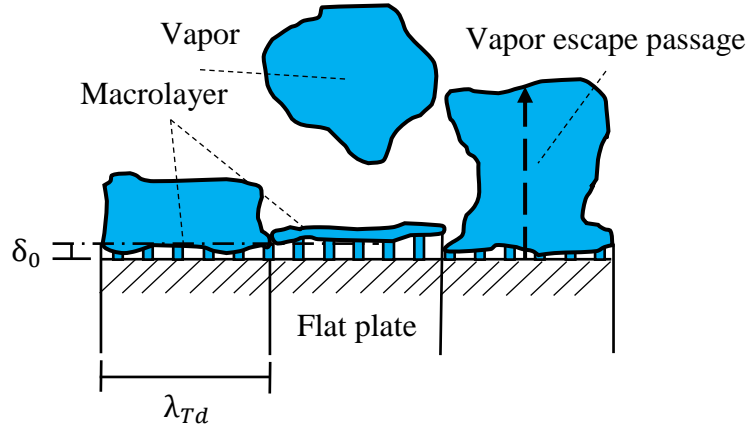
Fig. 3. Illustration of the macrolayer dryout model [Haramura & Katto]

Hydrodynamic instability models are characterized by the interaction between vapor and surrounded flow, in the contrast, microlayer dryout models focus on the interaction between the macrolayer and heated surface. (Kutateladze, 1948) and (Zuber, 1959) both published their CHF models based on HI. Extending the work of Kutateladze, Zuber's model concluded that Helmholtz instability and Taylor instability both play an important role on heat transfer mechanisms. Zuber's model is presented as

$$q''_{CHF,f} = kL\rho_v \left(\frac{\sigma g (\rho_v - \rho_l)}{\rho_v^2} \right)^{\frac{1}{4}} \left(\frac{\rho_l}{\rho_v + \rho_l} \right)^{\frac{1}{2}}, \tag{2.1}$$

where q''_{CHF} is the critical heat flux for infinite plane, $k = \pi/24 = 0.131$, σ is the surface tension, g is the constant for gravitational acceleration, L is a length-scale, ρ_v refers to the vapor density, and ρ_l is the liquid density. Helmholtz wave occurs on the interface between two mediums with different velocity. In the case of Zuber's model, the two mediums are upward vapor flow and surrounded liquid bulk (Fig. 4). If the velocity difference between the two mediums is large enough, c^2 becomes negative and Helmholtz instability results to

$$c^2 = \frac{\sigma m}{\rho_l + \rho_v} - \frac{\rho_l \rho_v}{(\rho_l + \rho_v)^2}, \tag{2.2}$$

where $m = 2\pi / \lambda_h$ and λ_h is the Helmholtz wave-length.
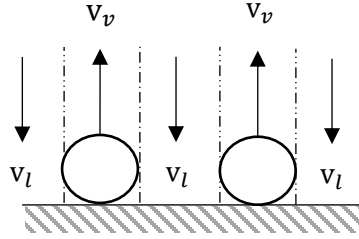
Fig. 4. Sketch of Helmholtz instability

Additionally, Taylor waves result from density differences in fluids interacting with one another. During bubble growth, liquid surrounds the vapor substrate generated from a heated surface (Fig. 5) thereby creating local opportunities for a fluid with significant density gradients to interact.
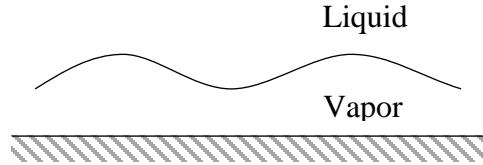
Fig. 5. Sketch of illustrating Taylor wave

Once the Taylor wave length is larger than critical Taylor wave length shown as (2.3), Taylor instability occurs.

$$\lambda_c = 2\pi \left(\frac{g_c \sigma}{g\left(\rho_l - \rho_g\right)} \right)^{\frac{1}{2}}. \tag{2.3}$$

Following Zuber's work, (Lienhard & Dhir, 1973) extend the concept of Taylor wave lengths by identifying specific lengths which cause the most likely set of conditions for Tayler instability to occur. In this case they identified the critical Taylor length-scale as

$$\lambda_c = 2\pi \left(\frac{3g_c \sigma}{g(\rho_l - \rho_g)} \right)^{\frac{1}{2}}, \tag{2.4}$$

which resulted in an updated version of (2.1) to be

$$q''_{CHF,f} = 0.149 L \rho_v \left(\frac{\sigma g \left(\rho_v - \rho_l\right)}{\rho_v^2} \right)^{\frac{1}{4}} \left(\frac{\rho_l}{\rho_v + \rho_l} \right)^{\frac{1}{2}}. \tag{2.5}$$

One of the most significant assumptions in Zuber's model is that the array of Leidenfrost columns (referred to as "vapor escape passage" shown in Fig. 2) are infinite and uniform in spacing. Lienhard and Dhir attempted to remove this assumption with their model by generating the relation of

$$q''_{CHF} = f\left(L'\right)q''_{CHF,f},$$ (2.6)

where q''_{CHF} is the critical heat flux, $q''_{CHF,f}$ is the critical heat flux for infinite flat plane and L' is a dimensionless unit for different geometries of heater, defined as

$$L' = L\left(\frac{\sigma}{g\left(\rho_l - \rho_v\right)}\right)^{-1}.$$ (2.7)

The result of this extension to the original model provided variability in predicting CHF when applying unique heater sources.

2.1.3 Macrolayer Dryout Models

Two of the most critical issues of the HI model are that it fails to predict the formation of the macrolayer and it does not account for the influence of surface properties. (Gaertner, 1965) was able to experimentally capture the complete process of bubbles forming during heating via the application of high-speed cameras. The result from (Gaertner, 1965) depicted two culminating observations including a macrolayer which formed on the heated surface and the formation of mushroom-like bubbles during heating process with high heat flux. Neither of these were explained within Zuber's model (1959).

With the observations from Gaertner (1965), (Haramura &Katto, 1983) developed the first macrolayer dryout model. Haramura and Katto asserted that the formation of the macrolayer is due to the limitation of Helmholtz wave near the surface. As a result, two assumptions were made. First, the thickness of the macrolayer (δ_0) should be less than a Helmholtz wave length. They assumed the critical macrolayer (δ_c) thickness is a quarter of one Helmholtz wave length found to be

$$\delta_c = \frac{\lambda_h}{4} = \frac{\pi}{2}\sigma\frac{\rho_l + \rho_v}{\rho_l\rho_v}\left(\frac{A_v}{A_w}\right)^2\left(\frac{\rho_v h_{fg}}{q}\right)^2,$$ (2.8)

where A_v is the effective vapor area, A_w is the effective wetted area, and h_{fg} is the latent heat of vaporization. Second, it is assumed that critical heat flux occurs when the time required for macrolayer to dryout is equal to the time for bubble to departure. Using these two assumptions and solving (2.8) with (2.4) and (2.5) they produced the final form of their macrolayer dryout model:

$$\frac{q}{\rho_v h_{fg}} \left(\frac{\sigma g (\rho_l - \rho_v)}{\rho_v^{\,2}} \right)^{-\frac{1}{4}} = \left(\frac{\pi^4}{2^{11} \cdot 3^2} \right)^{1/16} \left(\frac{A_V}{A_W} \right)^{5/8} \left(1 - \frac{A_v}{A_w} \right)^{5/16} \left(\left(\frac{\rho_l}{\rho_v} + 1 \right) \left(\frac{11}{16} \frac{\rho_l}{\rho_v} + 1 \right)^{-3/5} \right)^{5/16} . \quad (2.9)$$

2.1.4   Wettability

Nevertheless, Haramura and Katto's model (1983) failed to explain the influence of wettability. Wettability is defined by a fluid's contact angle as it interacts with the surface that it resides upon. A fluid having a contact angle less than 90° as shown in Fig. 6 is referred to as a highly wettable fluid and one with a contact angle great than 90° is considered poorly wettable. The ability for liquid substrate to contact a surface was hypothesized even in the earliest of studies to influence the CHF.
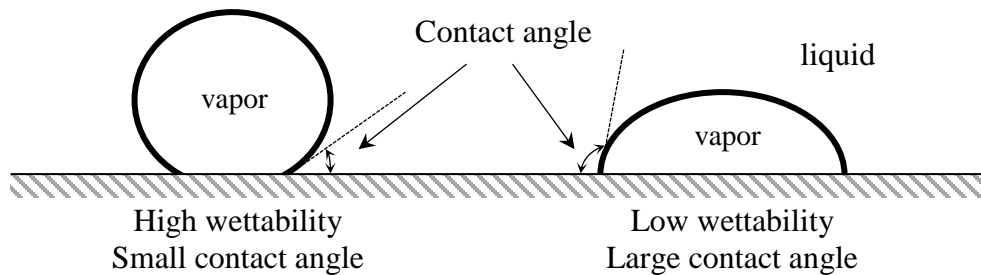
Fig. 6. Sketch of contact angle and wettability

(Liaw &Dhir, 1986) published their experimental study and were able to explicitly observe the influence of surface wettability on the occurrence of CHF using water and Freon-113. It was found that two boiling curves existed for heating and cooling, respectively and that the difference between two curves diminished as the surface wettability became better or as contact angle became smaller.

To speak to the wetting influence in CHF, (Pan &Lin, 1990) modified Haramura and Katto's model (1983). Pan and Lin hypothesized that the fraction of surface occupied by

vapor stem (the term A_v/A_w in (2.9)) was underestimated and only could be applied to fluids having a contact angle between 50° to 90°. Thus, the fraction of surface occupied by vapor stem was modified by Pan and Lin to

$$\frac{A_v}{A_w} = C\theta^{-n}\left(\left(\frac{11}{16}\frac{\rho_v}{\rho_l}+1\right)^{3/5}\left(\frac{\rho_v}{\rho_l}+1\right)^{-1}\right)^{1/2}. \qquad (2.10)$$

To ensure the usability of this model, (Pan &Lin, 1991) investigated the effect of several important parameters, including cavity size distribution, the thickness of surface coating, substrate thermal properties, system pressure and liquid subcooling. The result was that the model showed good agreement to experimental data.

2.2   Transient Boiling

Transient boiling refers to any boiling occurrence in which either hydrodynamic or thermodynamic conditions are not at equilibrium. This generalization has resulted in countless exploratory studies associated with the observation of CHF while changing all forms boundary conditions as a function of time. For focus, the breadth of discussion herein will consider power-transient CHF experiments and models specifically with only brief reference to other transient CHF studies performed that have significant impact on the subject.

2.2.1   Power Transient CHF Experiments

The earliest transient boiling experiment is chased back to (Rosenthal, 1957). A power type transient boiling experiment was performed through use of a 0.1 *in.* wide, 3 *in.* long and 0.001 *in.* thick ribbon heater submersed in water at atmospheric pressure. The peak heat flux produced by the ribbon heater was 5E6 *Btu/hr-ft²* within 30 to 500 *ms* period. During the experimental study an exponential increase in power was applied to the ribbon heater via the relation:

$$P = P_0 e^{t/\tau}, \qquad (2.11)$$

where P is power generation, P_0 is initial power, and τ is exponential heating period which is a constant varied during the study between 5 to 75 *ms*. Empirically utilizing several ribbon materials and testing more than 15 unique experimental conditions resulted in an

observed increase in CHF with a decrease in the exponential heating period. In addition, a specific phenomenon of "temperature overshoot (OV)" is revealed and attributed to the delayed ONB. Rosenthal denoted the following specific observations from this experimental campaign:

- OV increases by the decreasing of exponential period or increasing of water subcooling.
- There is no OV or delay time when water subcooling is near saturation.
- A significantly increasing of CHF only appears when an exponential period of less than 15 *ms* is applied.
- The OV may be due to a delayed response of natural convection. The water bulk near the surface during the OV possibly performed like a semi-solid with heat removal only by conduction.

(Tachibana, Akiyama, &Kawamura, 1968) followed suite with a similar power type transient boiling experiment. Strip (ribbon) heaters with different thickness, 0.01 *mm*, 0.05 *mm* and 0.1 *mm*, were used to observe the influence of heater geometry. Different from Rosenthal (1957), the rate of power increase was specified by a linear ramp-period with respect to time as following:

$$P = P_0 \left(\frac{t}{t_0} \right), \tag{2.12}$$

where t_0 is the linear heating period. The experiments were held near the saturated temperature for all tests considered by Tachibana et al. The outcome of this study corroborated some observations made by Rosenthal (1957), but not all:

- Transient CHF increases with an increased rate of power while lower rates of power approach that of quasi-steady state CHF.
- In the non-boiling region, conduction is the main heat transfer mechanism since the results agree with the derived boiling curve which considers convection as only heat removal method.
- All the bubbles on the surface remains in first generation even when the CHF is reached.

- The physical mechanism behind the OV may not be the response of delayed ONB since the first bubble is observed to be formed earlier before the inflection of boiling curve.

- No OV is observed.

To study the influence of pressure, subcooling and exponential period to transient boiling, (Johnson, 1970) studied transient boiling while controlling pressure (14.7, 500, 1000, 2000 *psi*), subcooling (10, 42, 112 *°F*) and exponential period (5, 15, 50 *ms*). The geometry of heater was of the ribbon-type, maintaining consistency with Rosenthal (1957) and Tachibana (1968). Bubble generation and growth was measured via *x*-ray radiography. This was the first comprehensive study to vary multiple fluid properties and boundary conditions using a parametric approach. The results of Johnson's experiments were compared to the previous studies and showed good agreement in conditions that aligned with the previous investigators. However, in some cases with lower pressure and higher subcooling, it was observed that early voids condensed in place which was believed as the main reason of OV. Furthermore, Johnson indicated that the observed OV phenomenon was confined to the nucleate boiling regime, and should therefore be carefully qualified since it was different from the hypothesis issued by (Hall &Harrison, 1966).

(ASakurai, Shiotsu, &Mizukami, 1970) also used a ribbon heater with an exponential power output at atmospheric pressure to study power transient CHF. Similar to the previous studies, an overshoot of temperature was revealed under 20 *ms* heating period. Furthermore, Sakurai et al. introduced two curves with significant difference for long heating period and short heating period, respectively (Fig. 7). In the long heating period case, the authors found that a larger heat transfer coefficient on the heated surface led to a small temperature difference on curve (*CD* and *DE* in Fig. 7). They also asserted that the value of transient CHF may be predicted by creating a correlation between heat input and the transient heating period with any wave form.
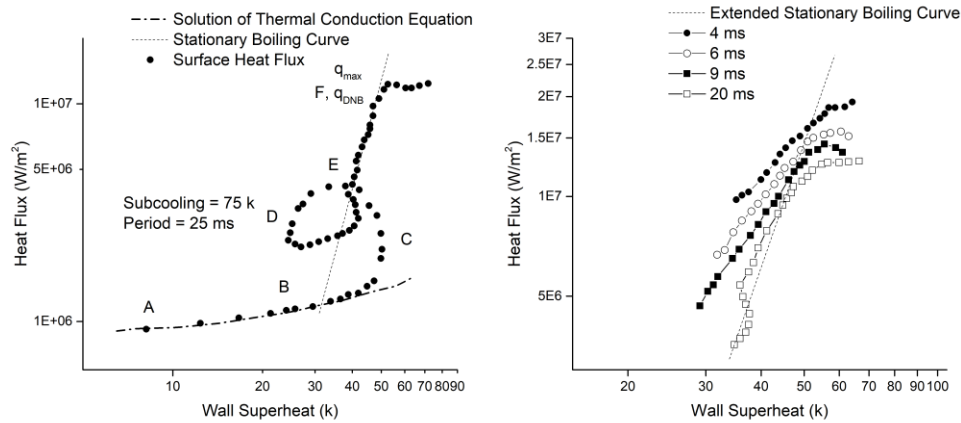
Fig. 7. Boiling curve with long period (left) and short period (right) [Sakurai et al.]

Followed by previous study, (ASakurai &Shiotsu, 1977) developed an experimental study based on a wire heater with 50.9 *mm* in length and 1.2 *mm* in diameter. Tests were performed under different pressures and exponential heating period. Testing at 0.588 *MPa* which is shown in Fig. 8, reveals two kinds of transient boiling curves categorized into "regular type" and "irregular type" by the authors. Curve *ABCD* and *EFGH* in Fig. 8 represent the "regular type" which have a transient CHF after the curves attach on the extended quasi-steady boiling curve. On the contrary, curve *IJK* represents the "irregular type" which provides a transient CHF before the attachment of extended quasi-steady state boiling curve. Sakurai and Shiotsu had three culminating observations from this study:

- The irregular transient boiling is triggered only when the exponential heating period is short enough.

- The CHF in the irregular case is first decreased then increased by the decreasing of exponential heating period. Although, the regular case only shows a trend of increased CHF with the decreasing of exponential heating period.

- It is assumed that the shifting between two types of transient boiling curves is due to the delay of activated nucleate cavities. The nucleate cavities which are originally flooded tend to be triggered sluggishly. The hypothesis is supported by the heat transfer coefficient derived from the experimental data.
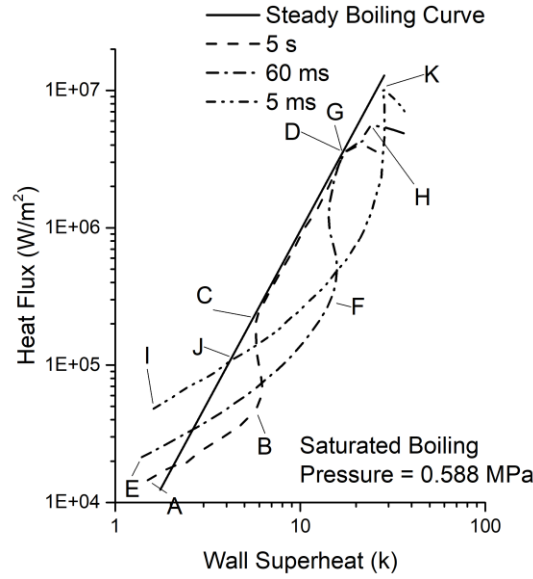
Fig. 8. Graphic depicting transient boiling curve of 0.588 MPa [Sakurai & Shiotsu]

Few studies have considered power type transient boiling with forced convection. (Kataoka &Serizawa, Akimi, Sakurai, 1983) studied transient flow boiling with different flow velocities, pressures and subcooling levels. In the study, a platinum wire with diameter of 0.8, 1.2 and 1.5 *mm* and length of 3.93, 7.12 and 10.04 *cm* were investigated. Both types of transient boiling curves defined by Sakurai et al. (1970) were observed under the scenario of forced convection. Similar results to the stagnation flow condition are observed that CHF increased with the decreasing of heating period and the increasing of pressure, velocity and subcooling. Serizawa et al. have developed a correlation which predicts the transient CHF with above-mentioned variables within a 20 percent error of those experimental cases compared against. Following is the correlation.

$$\frac{q''_{CHF,tr}}{GH_{fg}} = 0.3740 \left(\frac{\rho_v}{\rho_l} \right)^{0.66} \left(\frac{\sigma \rho_l}{G^2 l_0} \right)^{0.4}$$
$$\cdot \left(1 + \left(0.03648 \left(\frac{l_0}{d_{he}} \right)^{-0.2} \cdot \left(\frac{\rho v}{\rho l} \right)^{-0.79} + \varepsilon \right) \frac{\Delta H_i}{H_{fg}} \right) , \qquad (2.13)$$
$$+ 0.2038 \left(\frac{\rho_v}{\rho_l} \right)^{0.52} \cdot \left(\frac{\sigma \rho_l}{G^2 l_0} \right)^{0.19} \cdot \left(\frac{\tau G}{\rho_l l_0} \right)^{-0.63}$$

where $q''_{CHF,tr}$ is transient critical heat flux, G is mass flux, l_0 is laplace coefficient, d_{he} is heated equivalent diameter, and ε is inlet subcooling coefficient defined by author and H_i is enthalpy of inlet subcooling.

2.2.2   Power Transient CHF Models

With developed experiments and correlations, (Serizawa, 1983) formulated a model to predict transient CHF which is led by the rapid increase in power.

For $q'' = q''_0 e^{t/\tau}$

$$\tau \left[q''_{CHF,tr} - q''_{CHF,ss} \left\{ 1 + \ln \left(q''_{CHF,tr} / q''_{CHF,ss} \right) \right\} \right] = \rho_l h_{fg} \delta_m (1 - \overline{\alpha}), \tag{2.14}$$

where, $q''_{CHF,ss}$ is quasi-steady state CHF, δ_m is mean macrolayer thickness, and $\overline{\alpha}$ is mean void fraction. Based on the photographic observations from (Torika, Hori, Akiyama, Kobori, &Adachi, 1964) and the macrolayer dryout model, a new model was formulated to compare with the experimental results, including the experiments from (Kataoka &Serizawa, Akimi, Sakurai, 1983). The model attributed the macrolayer evaporating to the thermal thinning and shows an ability to predict transient CHF via stagnation and flow condition.

(Pasamehmetoglu, Nelson, &Gunnerson, 1990) questioned Serizawa et al.'s model (1983) via three potential defects.

- The physics behind the formation of the macrolayer assumed by Serizawa et al. is contradicting to Haramura and Katto's model (1983). While the latter explained the formation of the macrolayer is dependent on the surface condition, the former assumed the macrolayer is formed by the supplying of water bulk.

- The validation of the model is based on the experimental data which is also used for the model development. With the nature that the macrolayer thickness may serve as a crucial portion of the model, it is not suitable to derive the macrolayer thickness within the model from the experiments that also used for model as the validation approach.

- The hydrodynamic thinning is a crucial portion of macrolayer thinning. The thermal thinning should not be the only consideration. This is graphically presented in Fig. 9.

By the improvement of the above-mentioned defects, (Pasamehmetoglu et al., 1990) developed a more acceptable model including the quasi-steady state assumption within the context of a fast transient. The hydrodynamic and thermal effects contribute to the thinning of the macrolayer thickness, where the former represents to the first term of the right-hand side in (2.15) and the latter is shown in the second term.

$$\frac{d\delta_0}{dt} = \max\left(\left|\frac{\partial}{\partial q''}\frac{f_1(p)}{(q''(t))^2}\frac{dq''}{dt}\right|, \left|\frac{q''}{f_2(p, \Delta T_{sub})}\right|\right), \tag{2.15}$$

$$f_1(p) = \frac{\pi}{2}\sigma\left(\frac{\rho_l - \rho_v}{\rho_l \rho_v}\right)\left(\frac{A_v}{A_w}\right)^2 (\rho_v h_{fg})^2, \tag{2.16}$$

$$f_2(p, \Delta T_{sub}) = \rho_l h_{fg}\left(1 - \frac{A_v}{A_w}\right)\left(1 + K\frac{C_p \Delta T_{sub}}{h_{fg}}\right), \tag{2.17}$$

where p is pressure, K is empirical constant, ΔT_{sub} is temperature subcooling and C_p is specific heat capacity.
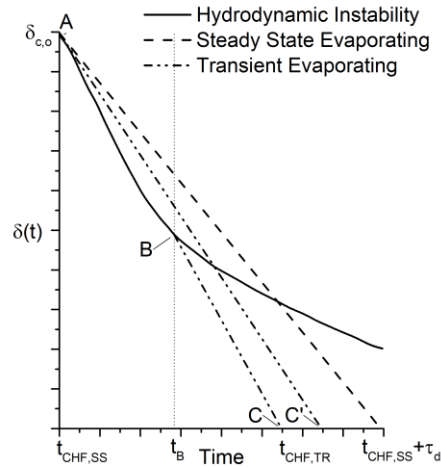
Fig. 9. Sketch detailing macrolayer thinning mechanism [Pasamehmetoglu]

2.2.3 *Heterogeneous Spontaneous Nucleation*

A recently identified phenomenon of direct transition from natural convection to film boiling without passing through nucleate boiling region has been observed and studied by several researchers. This phenomenon, named heterogeneous spontaneous nucleation (HSN), is theorized to occur as a result of the nearly instantaneous development of nucleate bubbles which form on the heated surface due to a fast power transient. HSN is found to be highly dependent upon the pressure and the heating period. Namely, HSN can be triggered by decreasing of the heating period and pressure. Generally, the higher the pressure, the shorter heating period is needed. Nevertheless, a discussion of HSN is warranted since it has been observed by Sakurai et al. and no other studies are presently attempting to try to duplicate the result from Sakurai et al.

(Shiotsu, Hata, &Sakurai, 1990) studied power transient boiling phenomenon using liquid nitrogen. A cylinder type heater with a linear increasing heat input was applied in the experiments with the following temporal relation,

$$P = kt, \tag{2.18}$$

where Q is the k is the linear heat increasing rate. The results show a direct transition to film boiling without nucleate boiling introduced as indicated within Fig. 10. Under HSN conditions, the resulting CHF is found to be only 14 percent of its corresponding quasi-steady state CHF. It should be noted that, in past studies, transient CHF was characterized by a higher value of its corresponding quasi-steady state CHF. With constant pressure, the authors indicate that there is a lower limit of temperature (T_{HSN}) for HSN to occur against the heat increasing rate. The following provides a summary of the most significant outcomes of their efforts:

- T_{HSN} is dependent on the heat increasing rate. A higher increasing rate leads to the rising of the T_{HSN}.
- T_{HSN} is dependent on the pressure. With constant heat increasing rate, a higher pressure leads to a higher T_{HSN}.
- T_{HSN} is independent on the heater surface condition.
- The influence of pressure on T_{HSN} is postulated to be the variation of liquid surface tension which is led by the pressure changing.
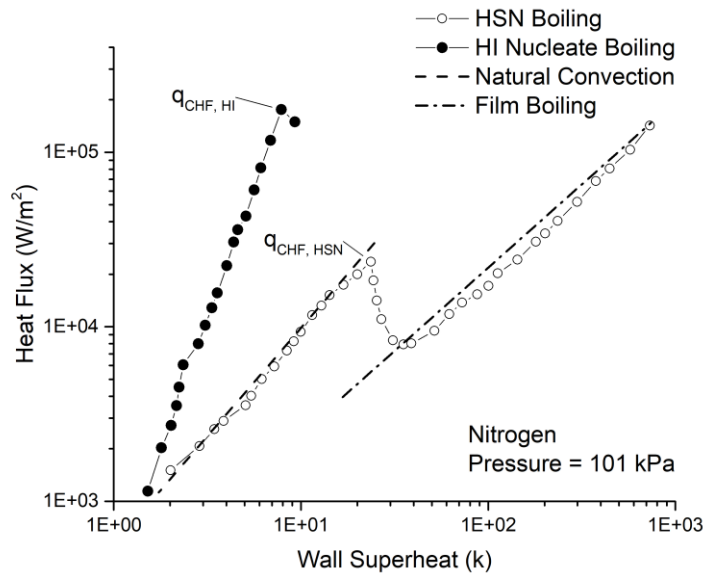
Fig. 10. Data showing direct transition of film boiling [Shiotsu et al.]

For the purpose of confirming that HSN may be characterized for other types of coolant, (ASakurai, Shiotsu, &Hata, 1993) further explored the transient boiling phenomenon under the stagnation flow condition by using water as coolant. The results indicate that the HSN phenomenon is able to be reproduced when water is used, however, only with a certain degree of pre-pressurization before the application. The authors attribute the discovery to the influence of surface tension. With the pre-pressurized step, it is believed by the authors that the coolant is forced to flood into the originally unflooded cavity and, thus, triggers HSN.

In the subsequent study, (AkiraSakurai, Shiotsu, Hata, &Fukuda, 1995) further summarized the influence of the pre-pressurization as seen in Fig. 11 and classified three different groups of transient boiling by the CHF and its corresponding heat flux of ONB, shown in Fig. 12. With the occurrence of HSN, a direct transition from natural convection to film boiling is confirmed. Namely, the CHF is observed to occur with a similar value to the ONB heat flux. The first transient boiling group classified within the study corresponds to tests having a relatively long heating period while the second group ($q''_{CHF} = q''_{ONB}$) has a relatively short heating period. The third group has an intermediate heating period between the first and the second group and considered a transition region.
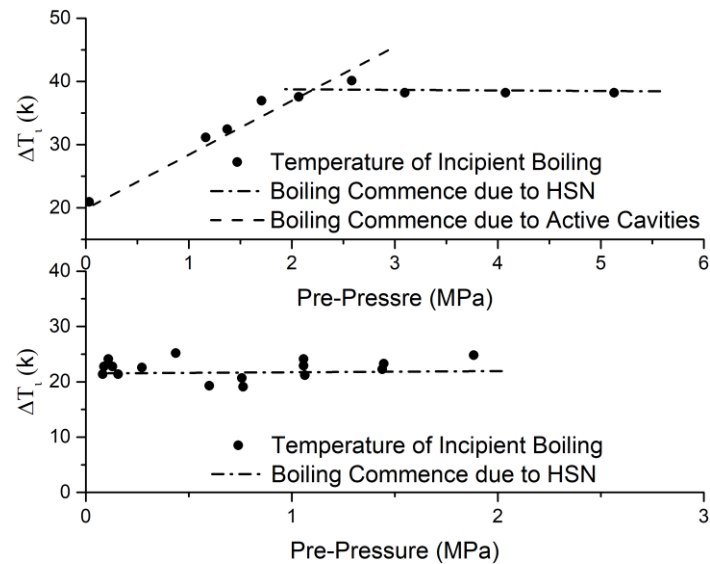
Fig. 11. Temperature of incipient of boiling for nitrogen and water [Sakurai et al.]
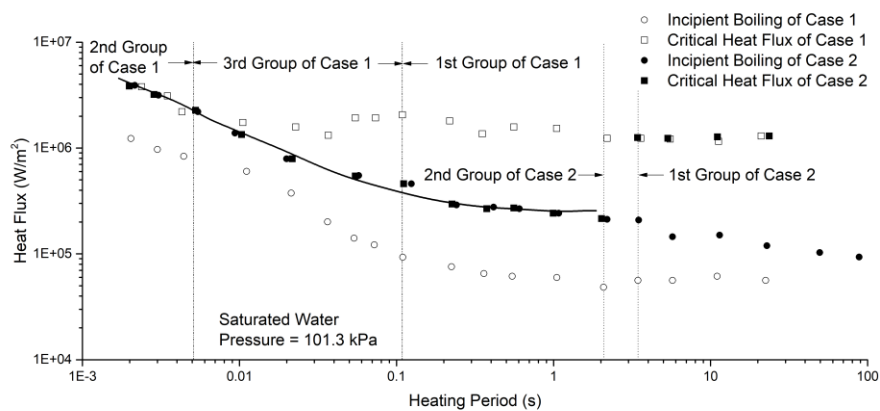
Fig. 12. Three groups of transient boiling against heating period [Sakurai et al.]

(ASakurai, 2000) did a review for transient boiling with respect to HSN, including the empirical applications and a new hypothesis of mechanism. That is, HI dominates the transient CHF for the first group boiling while HSN dominates the second group. It should be clarified that the HI mechanism-based approach is validated by the model from Pasamehmetoglu (1990) shown in Fig. 13. Pasamehmetoglu's model is based on the theory of macrolayer thinning instead of the HI. Thus, a narrative around the concept that 'a mechanism of non-HSN dominates the transient boiling from the first group' was expanded upon. To support the above-mentioned new hypothesis, a photographic observation with

respect to HSN corroborated this work and was conducted by (ASakurai, Shiotsu, Hata, &Fukuda, 2000). A clear difference between HSN and non-HSN mechanisms is distinguished.
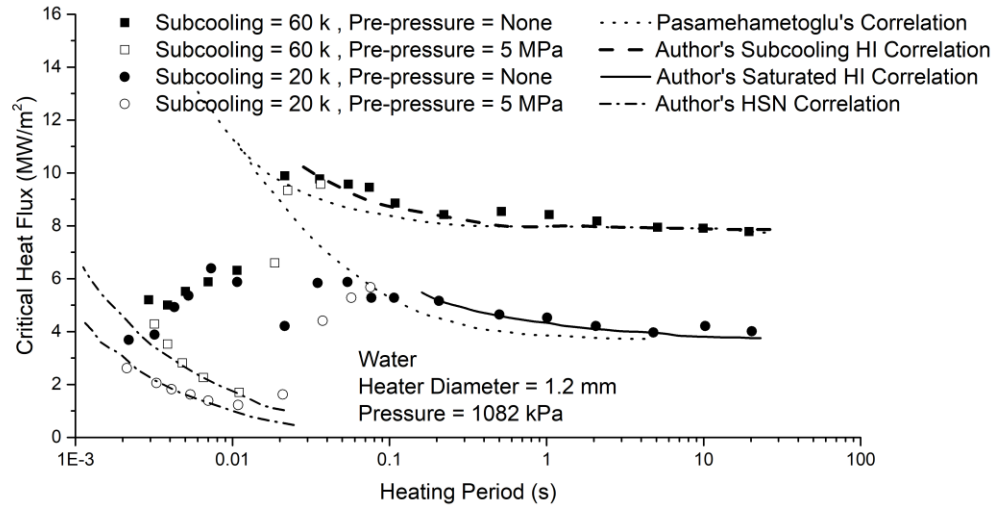
Fig. 13. Transient CHF compared with various models [Sakurai]

2.2.4   Other Types of Transient CHF: Flow and Pressure

In the meanwhile, several studies focus on other types of transient boiling, which are flow and pressure transient, have been published. Since this study is focusing on power type transient boiling, the detail of other types of transient boiling will not be provided. However, several studies relate to the pressure and flow transient are listed in Table. 1. Generally, pressure transient provides a higher CHF than its corresponding quasi-steady state case. On the contrary, for the flow transient, CHF is generally lower than its corresponding quasi-steady state case due to a sudden flow deceleration.

Table. 1. Studies of other type transient boiling

Study	Flow transient	Pressure transient
(Aoki, Inoue, &Kozawa, 1974)		X
(Ishigai &Nakanishi, 1974)	X	
(A.Sakurai, Shiotsu, &Hata, 1979)		X
(Leung, Gallivan, Henry, &Bankoff, 1981)	X	X
(Iwamura, 1987)	X	
(Celata, 1991)	X	X
(Fukuda, Shiotsu, Hata, &Sakurai, 1994)		X

2.3 Two-Phase Computational Fluid Dynamics in Star-CCM+

2.3.1 Mesh Generating

Mesh generating is one the most fundamental topics for a CFD study. Even though meshes have no decisive impact to simulating results, it does provide significant influence in some cases. (CD-adapco, 2009) lists all the mesh models that are available under the frame of Star-CCM+. Typically, three kinds of primary (core) and one kind of optional (boundary) volume mesh models can be found for the purpose of three-dimensional simulation. These available models are listed in Table. 2.

Table. 2. Volume mesh models in Star-CCM+

Primary mesh model	
Tetrahedral	Tetrahedral cell shaped based core mesh
Polyhedral	Arbitrary polyhedral cell shaped based core mesh
Trimmed	Trimmed hexahedral cell shaped based core mesh
Optional mesh model	
Prism Layer	Orthogonal prismatic cell next to wall or boundary

The tetrahedral cell develops an efficiency and simple solution for the problems with complex geometry. It is also characterized as the fastest and least memory consuming mesh with a given number of cells. However, since the tetrahedral mesh model produces cells with a triangular shape, the meshes on the surface must be well developed to ensure the simulating domain is sealed.

The polyhedral cell provides a balanced solution between accuracy and computational cost for complex geometry. The mesh model generates five times fewer cells than tetrahedral

mesh model under the same degree of refinement. Though the polyhedral cells are coarser, they do provide a more accurate result due to an increased number of cell faces. It should be noticed that the increasing faces for the cell leads to additional computation between cells and, thus, causes a significant increasing of computational cost compared to tetrahedral and trimmed meshes.

Trimmed cells work well with the robust and efficient solution for both simple and complex geometry. The trimmed mesh model is most commonly combined with predominate hexahedral cells with trimmed cells next to the surface. The regular arrangement of the cells leads to the most robust computation among all the types of cells. However, due to the limited number of surfaces generated in each cell, the accuracy is weakened by the decreasing computation.

Prism Layer cells can be applied with three main models mentioned above. The purpose is to improve the mesh performance on the boundary or surface by generating of the boundary layer. The existence of prism layer supplements the importance of the physics which occur within the fluid boundary layer within CFD simulations. For the cases with turbulent flow, the boundary layer is necessary for the calculation of wall y^+ method which is highly influential to the accuracy and stability of solution attained, especially for the Reynolds Averaged Navier Stokes (RANS) model.

(Hernandez-Perez, Abdulkadir, &Azzopardi, 2011) did a survey to explore the influence of different mesh types for two-phase problem. The comparison of different mesh types was developed by the mesh models adopted in the Star-CD software package and the two-phase problem solved by the Star-CCM+ software package. The two-phase problem was defined as a three-dimensional vertical pipe with the flow passing through from the bottom side. The pipe wall was treated as a thermal boundary which heated the water flow directly. The volume of fluid (VOF) model, which is one of the most common two-phase model provided by Star-CCM+, was adopted to compare the difference between mesh models shown in Fig. 14. The study summarized that the butterfly-grid shows the best result for validating its corresponding empirical application. Specific observations were be broken

down into two: First, the velocity profiles are well performed by the hexahedral cells in the center of the pipe for the mesh type of H-grids, butterfly-grid and unstructured pave grid. Second, during the refinement of the above-mentioned models, the performance of the flow and heat transport on the boundary are not improving in the same degree. For both unstructured pave grid and butterfly-grid, a fair improvement is seen. However, the butterfly-grid has the capability to provide good agreement with the validating data by only refining on the heated boundary. It can be concluded that the core meshes may have no significant impact to the accuracy, however, this is not the case for the boundary meshes.

(a)   (b)

(c)   (d)
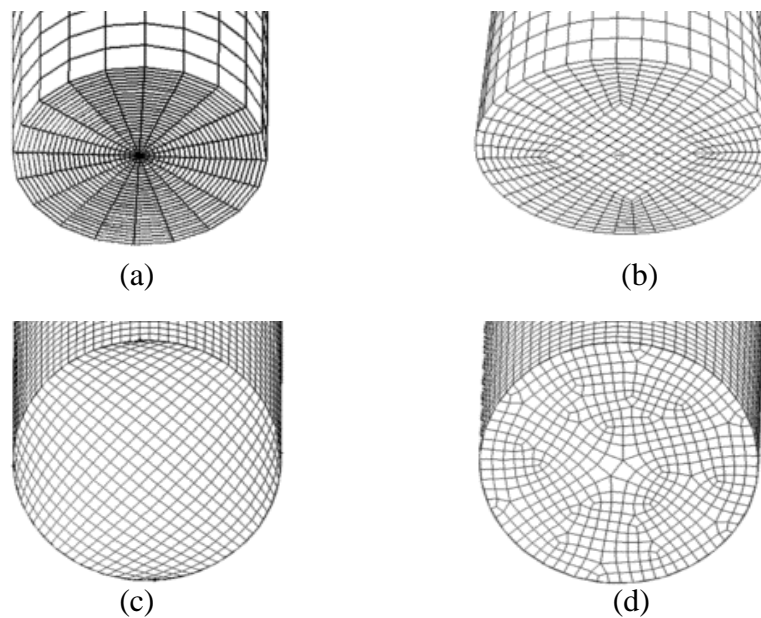
Fig. 14. Mesh types (a) O-grid, (b) butterfly, (c) H-Grid, (d) unstructured pave

2.3.2   Turbulent Models

The application of turbulent models plays an important role for presenting the viscosity and vorticity behavior in the CFD studies. The appropriate selection of the turbulent model may lead to a more accurate result with a more stable computational operation. Since turbulence influences the flow and velocity profile near the surface or boundary, the decision of the model may significantly influence the heat removal on the heated surface, especially for the boiling case with flow. (CD-adapco, 2009) lists all the twenty-three turbulent models that can be applied under the frame of Star-CCM+. These models can be

categorized as three different types which are Detached Eddy Simulation (DES), Large Eddy Simulation (LES) and RANS. Furthermore, RANS model provides four most widely used turbulent models. Table. 3 lists the most common selections of turbulent models within the Star-CCM+ software package.

Table. 3. Common turbulent models in Star-CCM+

	Model	High-y^+	Low-y^+	All-y^+
DES	SST k-ω Detached Eddy	X	X	X
LES	WALE Subgrid Scale		X	X
RANS	Realizable k-ε Two Layer			X
	SST (Menter) k-ω	X	X	X
	Reynold Stress			X
	Standard Spalart-Allmaras		X	

In (Chen, 2009), the scale effect to the blade ratio is investigated with respect to different turbulence models. The author compared three types of turbulence models and explained the difference via simulating external flow on a bumped surface. As graphically sketched in Fig. 15, the local vorticity that can be resolved by DES and LES are in a relatively small scale compared to RANS. To handle the characterization of micro scale vorticity, highly refined meshes are necessary that a traditional desktop computer may lack in abilities to execute the simulation. To support extremely high computational costs, a supercomputer or High Performance Cluster (HPC) is needed. On the contrary, instead of calculating the transport equations numerically, RANS model provides an estimate with better computational cost through use of time averaging flow characteristics via the Navier-Stokes equation.
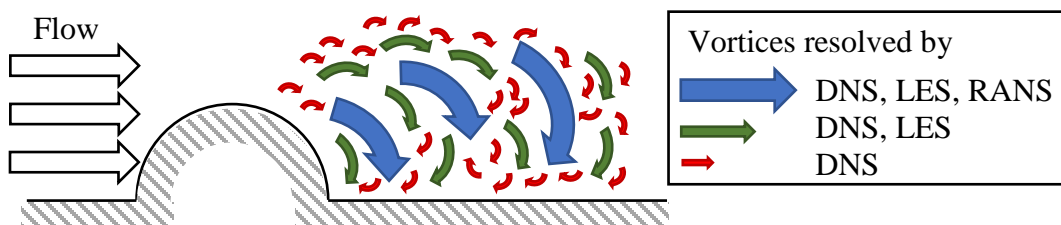
Fig. 15. Turbulent scales resolved by DNS, LES and RANS [Chen]

With the consideration of only RANS models, (Davis, Rinehimer, &Uddin, 2012) did an exploration of accuracy between SST (Menter) k-ω, Realizable k-ε and V2F k-ε. The validation is done via an empirical application of the external flow passing along a surface with a wall-mounted block. The results disagreed to the traditional thought that a k-ω model should provide better resolution. Yet, the results showed that the Realizable k-ε two-layer model did a better job among all others. It was concluded by the author that the improvement of the realizable k-ε from its traditional version leads to a better resolved characterization within the viscous sublayer. While the high-y^+ wall treatment is adopted by the traditional k-ε, the realizable k-ε is modified for the compatibility of the two-layer approach. The traditional low resolution in the viscous sublayer is, thus, improved by the all-y^+ wall treatment which is adopted by the two-layer approach.

For CFD studies which contain complex physics, the mesh size may become an important issue. Due to the highly refined meshes needed, an inappropriate selection of the wall treatment method will lead to additional stability issues and thus impact the accuracy. In the Star-CCM+ software package, all the turbulence models have their own compatible wall treatment as seen in Table. 3Table. 3 and can be categorized as three different methods which are high-y^+, low-y^+ and all-y^+ graphically shown in Fig. 16. For high-y^+ method, the viscous sublayer near the surface is not resolved. In contrast, low-y^+ method resolves the viscous sublayer and provides a more accurate predication for the physics near the surface. Served as a combination of high-y^+ and low-y^+ method, the all-y^+ method provides an advantage of automatically deciding the wall treatment method by the size of the surface meshes which should be a preference.
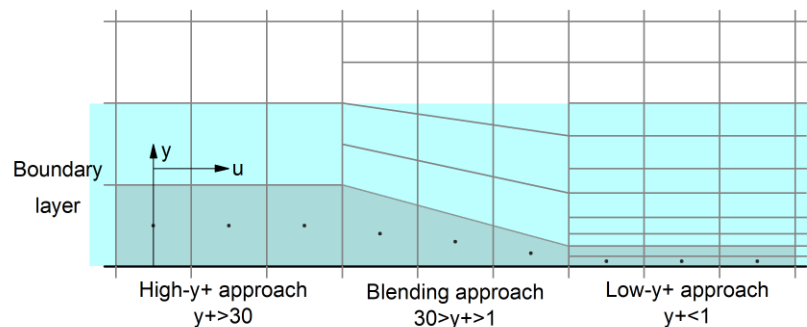
Fig. 16. Wall treatment of high-y^+, low-y^+ , and all-y^+ method [CD-Adapco]

2.3.3   Two-Phase Heat Transfer Models in Star-CCM+

The Star-CCM+ software package simulates boiling by the using different Eulerian multiphase models. Under the frame of Eulerian multiphase models, two-phase problems can be solved via either a segregated or coupled flow solver. However, the segregated flow solver is the only solver that can be applied if the boiling process is included in the multiphase problem. The main difference between two solvers is that the energy equation respect to continuity and momentum equation, is solving independently or not. Namely, the accuracy and the computational cost is highly dependent on the types of the solver. Typically, the segregated flow solver is found to be faster and more robust but with less accuracy. In the contrast, the coupled flow solver provides a more reliable, however, more expensive solution.

Three different Eulerian multiphase models are provided by Star-CCM+, which are referred to as the Eulerian multiphase mixture (MMP), multiphase segregated flow (EMP) and VOF models. It should be noticed that not all the Eulerian multiphase models are compatible with both types of solvers. The brief introduction of three kinds of model are included in (CD-adapco, 2009) a shown in Table. 4.

Table. 4. Eulerian multiphase models

Model	Description	Flow solver
MMP	Considering only one mixture quantities with changing properties according to phase volume fraction.	Segregated or coupled flow solver
EMP	• Coupled flow solver for equations within phase. • Segregated flow solver for equations between phases.	Segregated and coupled flow solver
VOF	• A simpler multiphase model. • Considered as a special case of MMP.	Segregated flow solver

In MMP and VOF, two-phase flow is considered as a mixture quantity. Namely, the flow is treated as a single mixture phase, however, the mixture phase can be characterized through changing of the material properties as a function of the void fraction. This attribute of these models leads to the lacking ability of resolving the interface between two phases. In some cases, the low computational cost makes MMP become an alternative model to the EMP. Depending on the different assumptions made for two-phase interaction, three

different sub-models may be selected under the frame of MMP, seen in Table. 5. Nevertheless, MMP is the two-phase model that only focuses on the averaged behavior between two phases. As a result, EMP and VOF should be considered for the two-phase problems that containing boiling.

Table. 5. Eulerian multiphase mixture

MMP	Homogeneous multiphase	• Homogeneous single mixture phase • Thermal equilibrium • No relative speed between two phases
	Algebraic slip	Defining relative velocity between two phases by empirical correlations.
	Drift flux	Defining relative velocity between two phases by kinematics effect.

As a "real" two-phase model, EMP treats two-phase flow as two independent phases with their own respective material properties. One most important characteristic of the EMP is that the primary and second phase in the flow are considered as continuous flow and particles, respectively. The interaction between phases is, then, solved in the manner of flow-influenced particle. The "segregated" term in "multiphase segregated flow" referred to the fact that the pressure and velocity are solved independently instead of coupled with continuity and energy equation. It is expected that the accuracy is highly improved compared to the MMP, however, the computational cost is significantly increased. Though the accuracy is an advantage, the EMP model is also notorious for its stability issues. The heavy computation between particles and flow leads to an unstable process of coupling the solutions from different phases. As a result, the use of the EMP model should be carefully treated.

The VOF can be considered a special case of MMP. Different from the MMP which is not suitable for boiling type simulation, the VOF is designed for application with respect to boiling simulations specifically under the frame of multiphase mixture quantity. The interphase interaction is defined by the void fraction which is solved via heat transfer correlations. Under the frame of VOF, two different models which predict boiling by different correlations are available in the Star-CCM+ software package. These models are the Rohsenow boiling model and the transition boiling model. For the Rohsenow boiling

model, boiling is simulated via the nucleate boiling correlation from (Rohsenow, 1951) and, the film boiling correlation which considers only vapor heat transfer. The nucleate boiling model developed by Rohsenow is

$$q''_{Roh} = \mu_l h_{fg} \left(\frac{g \left(\rho_l - \rho_v \right)}{\sigma} \right)^{0.5} \left(\frac{C_{pl} \left(T_l - T_{sat} \right)}{C_{qw} h_{fg} Pr_l^{np}} \right)^{3.03} , \tag{2.19}$$

where μ_l is the liquid viscosity, C_{pl}, C_{qw}, np are empirical coefficients, T_l is the liquid temperature, T_{sat} is the saturated temperature of the water and Pr is the Prandtl number. However, the correlation is only suitable for the conditions where the subcooling between heated surface and coolant is small. If the correlation is applied out of the applicable range, for example in a film boiling regime, an unrealistically high heat flux may be predicted. With this concern, the Rohsenow boiling model uses a film boiling correlation to solve problems that contain high wall superheat.

Different from the Rohsenow boiling model, the transition boiling model uses the user-defined built-in functions to simulate the boiling. The three relations in (2.20) represent the boiling curve in the nucleate boiling, transition boiling A and transition boiling B regime, respectively and graphically shown in Fig. 17.

$$q''(\Delta T_w) = q''_{max} S \phi \left(\frac{\Delta T_w}{\Delta T_1} \right)^{K_1} \qquad\qquad , 0 \le \Delta T_w \le \Delta T_1,$$

$$q''(\Delta T_w) = q''_{max} S \left[1 - 4(1-\phi) \left(\frac{\Delta T_w - \Delta T_{max}}{\Delta T_2 - \Delta T_1} \right)^2 \right] \qquad , \Delta T_1 \le \Delta T_w \le \Delta T_2, \tag{2.20}$$

$$q''(\Delta T_w) = q''_{max} S \phi \left(\frac{\Delta T_w}{\Delta T_2} \right)^{-K_2} \qquad\qquad , \Delta T_2 \le \Delta T_w,$$

where ΔT_1, ΔT_2 are the respective wall superheats that defining the boiling regions. In the region of nucleate boiling and transition boiling B, K_1, K_2 are the factors that defining the slope for the boiling curve. In transition boiling A region, q''_{max} is the maximum heat flux that is used for boiling and φ is the factor that modifies the quadratic curve. The variable S in all three equations is the factor that scales the boiling curve according to the applications. All the above-mentioned variables are dependent on the empirical application which is different case by case. The default setting for these variables are from (Ellion, 1953).
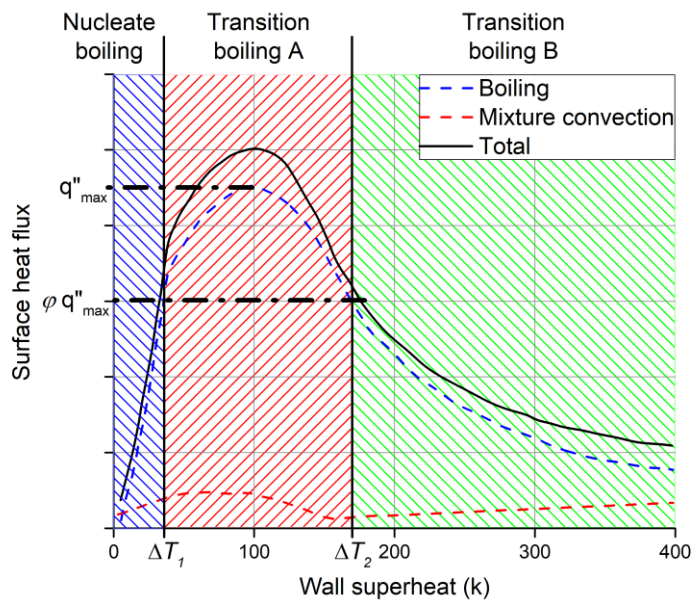
Fig. 17. Sketch detaling theorized transition boiling model [CD-Adapco]

In (Sontireddy &Hari, 2017), all four models (MMP, EMP and two types of VOF) mentioned above were compared against one another in a common problem compared against experimental data. In the application, a pipe with 12.03 *mm* diameter and 1 *m* length was explored with the conditions of inlet temperature 519 °*K* and pressure of 6.89 *MPa*. The upward internal flow was heated by a constant wall heat flux of 800 *kW/m²* from the pipe surface directly. As expected, the MMP showed a big difference between the simulation and the application. Even though the algebraic slip and drift flux model are used for the consideration of heat non-equilibrium, the result still indicated a poor ability of the volume fraction prediction. All other models provided a fair ability to predict both volume fraction and temperature against the application.

2.3.4   *Simulation of CHF Using Star-CCM+*

Recently, a robust number of studies have been performed which focus on efforts to validate CFD software packaged associated with specific phenomena. Among the studies, very few of them focus on the prediction of CHF. There are several reasons for which studies have avoided this topic. First, it is challenging to perform a CFD study which includes complicated physics under the transient two-phase flow. Numerical instability led by the complicated physics deteriorate when the time influence is included, especially for

the fast transient. Second, it is difficult to validate such a phenomenon due to the lack of mechanistic understanding of such a transient. Nevertheless, there are several studies which have explored boiling but have most commonly been limited to quasi-steady state. In general, currently, CFD software packages have a good ability to predict the macroscopic phenomenon for the boiling.

In most of the EMP studies, the CHF or boiling phenomena are studied under steady state models. (Krepper, 2007) did a validation study for the wall boiling model. The wall boiling model, which combines the evaporation, convection and quenching model, is the model contributes to the boiling under the frame of EMP. The validation of the models indicates a fair ability of wall temperature prediction by EMP, however, only under the frame of macroscopic. For the detailed phenomenon, for example, bubble coalescence and break up, further improvement is necessary. In (Povolny &Cuhra, 2014) and (Li et al., 2018), the influence of bubble dynamics is studied by the using of S-gamma model. Both studies indicate that the simulation provides good agreement against the empirical applications, however, with an acceptable higher value of CHF. Since the void fraction plays an important role for the occurrence of CHF when the wall boiling model is used, the vapor generation within the wall boiling model should be focuses. With this concern, both (Shirvan &Azizian, 2015) and (Colombo &Fairweather, 2016) performed validating studies to test the accuracy of simulations by the modification of wall boiling model. The former study included the influence of the macrolayer for the evaporation model and the latter study modified the evaporation model by nucleate site number density. Both studies indicated the accuracy should be improved via more extensive validation. Different from the focusing microscopic phenomena aspect, (Kim, Okhuysen, Demarly, &Baglietto, 2016) developed a boiling curve from the aspect of the heat flux and the wall superheat. The heat flux is considered a time independent variable and increased step by step. An iteration number of five-hundred was set up in each step for the stability purposes. Even though the boiling curve was successfully developed respect to the quasi-steady state CHF, the time influence remained a consideration for the boiling process. It should be noted that time dependent boiling is not studied by any of the studies that are mentioned above. For transient boiling, more studies are necessary for the time dependent behavior.

Instead of exploring CHF phenomenon in the simple geometries, most of the VOF studies have focused on the nucleate boiling phenomenon within specific test facilities. In (Youchison, Ulrickson, &Bullock, 2011) and (Domalapally, Rizzo, Savoldi Richard, Subba, &Zanino, 2012), boiling in the first wall of the International Thermonuclear Experimental Reactor (ITER) was studied by the using of several CFD software packages. The former study included the temporal influence of the Rohsenow boiling model, and the latter one focused on the comparison between the Rohsenow boiling models which are provided by Star-CCM+ and Fluent software packages. The authors in both two studies concluded that Star-CCM+ software package provides an accurate result with the VOF model. Furthermore, it is observed that a more accurate result is acquired by Star-CCM+ compared to the Fluent. In (Nagwase &Pachghare, 2013), boiling in the Closed Loop Pulsating Heat Pipe (CLPHP) was studied via the uses of the Rohsenow boiling model. The unsteady boiling model was successful to reproduce the same boiling pattern within the facility. (Lobón, Valenzuela, &Baglietto, 2014) performed a boiling investigation within the parabolic-trough solar steam generating system and good agreement was provided with the error less than 6 percent.(Domalapally &Subba, 2015) compared the Rohsenow and transition boiling model with the unsteady state assumption. Even though the criteria for the incipience of the film boiling was modified for Rohsenow boiling model to fit the empirical application, the results still indicated that the transition boiling model provided a more promising result outside the nucleate boiling region. The conclusions drawn were that the VOF models present the most accurate results with the error less than 10 percent in most of the case.

3   METHOD AND METHODOLOGY

This chapter discusses how to process a simulation using Star-CCM+ and how this study developed with Star-CCM+ provided model package. The content includes an overview of the improved CFD study process with new approach against transient boiling phenomenon, the simulating geometry and corresponding boundary conditions, the method for grid refinement study, the general physics and heat transfer models setting, and the necessary stability maintenance methods. The process of setting up a simulation with Star-CCM+ can be separated into three major steps as graphically shown in Fig. 18.
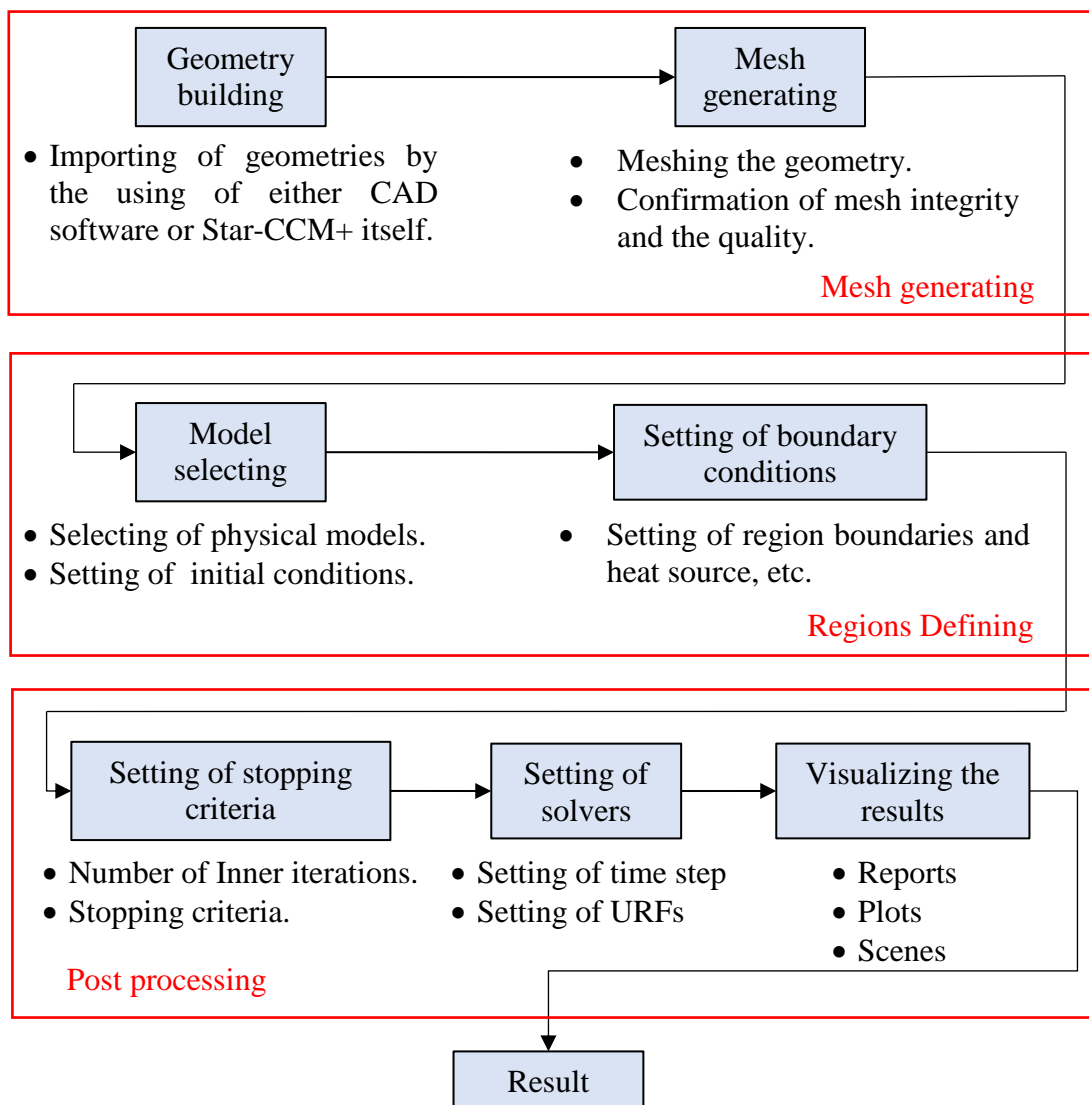
Fig. 18. Overview of process used with Star-CCM+

First, geometry and mesh building. It is well-known that CFD is highly mesh size dependent. In a general manner, a finer mesh set indicates a more accurate result. However, due to the limited computational resource, it is unrealistic to build a mesh set with extremely small size. As a result, a grid independent study is necessary to test how significant are the simulation results influenced by the mesh size. In this study, a simplified geometry from TRTL facility is adopted for the purpose of saving computational resource. This is due to the fact that the test section from the TRTL facility is simply constructed by the vertical pipe with cladding heater. If the true geometry of a test facility is complicated, for example, a heat exchanger, the way how to simplify the geometry may have a significant impact to the simulation result.

Second, defining the region by physics models and boundary conditions. Different from the potential influence from the geometries and meshes, the selection of physics models has a directly influence to the simulation result. To make sure the physics models setting is correct in this study, some reference, including past CFD studies and Star-CCM+ user guide, are considered. In addition, some detailed modifications, which are made under the instruction of the support group from CD-Adapco, are setting up for the stability maintenance. Since the EMP simulations are extremely fragile and notorious for their weak ability for maintaining stability, it is necessary to detail and discuss all the selections made for the model setting.

Last, the post-processing. Due to the complicated physics embed in two-phase heat transfer, it is difficult to obtain stable and converged results from the simulation with two-phase heat transfer, especially when EMP model is considered. That is, solvers and stopping criteria do play a crucial role in the stability maintenance. The problem stands for the balance between the efficiency and the converged ability. The decision of converged ability improvement may lead to a time-consuming converged process. However, in some situations, a simulation with complicated physics have no choice but necessary to improve the stability to prevent from a diverged consequence.

3.1   New Simulating Method

There are several studies performed the boiling process using CFD in the past. However, most of the studies are failed to include the influence of the heat deposit and corresponding temporal behavior. Thus, this study has developed a new approach based on the following method:

- Conjugate Heat Transfer (CHT)
- Implicit unsteady state

In most of the past study, a direct heat source is applied on the pipe wall. In the other words, the behavior of the heater (energy deposit) is not performed in those simulations. To illustrate a more realistic boundary condition, this study use the method of CHT. Different form traditional method, CHT method allowed the heat generates from the heater region and transfer from the heater region to the fluid region. The heat source can be set as volumetric heat source or total heat source to demonstrate the deposit of energy in the heater itself or the energy transfer between two regions by the heat flux. The detail of CHT method is provided in chapter 3.3.3.

To simulate the mechanism behind power transient boiling the influence of the time should be included in the simulation which means the simulation should processing under the frame of unsteady state. Star-CCM+ software package provides several different unsteady state time models. The detail of these unsteady state time models is provided in chapter 3.5.1. It is found out that, for the heat transfer type simulations, especially when the boiling process is included, the simulations become extremely fragile. The instability is come from the nature of phase treatment adopted by EMP models. Such instability issue deteriorated since the extremely complicated physics led by EMP model are combining with the using of implicit unsteady state model. The diverged simulation forced the consideration of simplified model setting and geometry. All the efforts that made for the stability maintenance are included in chapter 3.7.

3.2   Improved Process of Transient Simulation

Fig. 19 shows an improved CFD process for transient simulation that adopted in this study. In the pre-processing step, a simplified test section from TRTL facility is considered for the power transient boiling simulation. For the mesh generating, the polyhedral mesh set is able to provide a conformal interface which is confirmed to be necessary in this study. Although the using of trimmed mesh and corresponding mapped contact interface are also tested and summarized in chapter 3.3.3 and 3.4.1, it is proved that such simplification on the geometry and boundaries is not able to provide reasonable results and corresponding physics. Different from traditional transient simulations, a precursor simulation, which is processing with steady state model, is added before the transient simulation start. The purpose of the precursor simulation is to provide a necessary stability maintenance by giving transient simulations a fully developed flow and temperature profile as initial condition. To provide a similar initial condition to the experimental applications which is happen in TRTL facility, a 2.4 kW total heat source is added in the heater region to provide a near saturated wall temperature before the transient simulation begin. In transient simulation step, two types of studies which are grid independent studies and benchmark simulations are processing with implicit unsteady state model. While The former one is used to determine an appropriate mesh size for this study, the latter one is processing with heating period of 50, 75, and 100 ms to distinguish the significance of different boiling patterns.
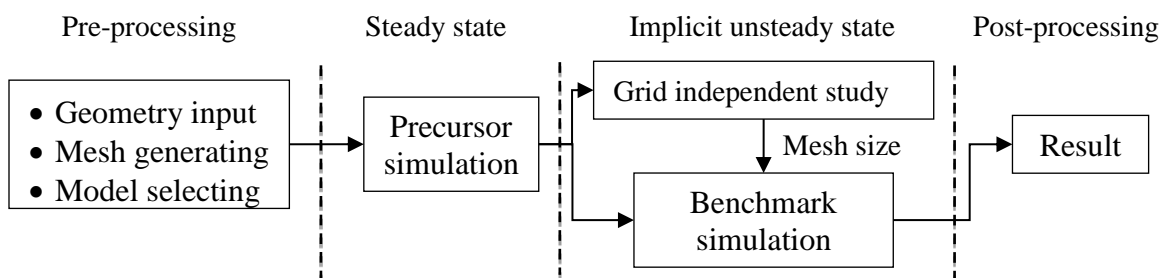
Fig. 19. Flow chart of improved transient CFD process

3.3 Geometry and Boundary Conditions

To simulate heat transfer within the TRTL facility test section in a robust pattern, a simplified geometry is built by Star-CCM+ and applied in this study. There are two different sets of heater rod for TRTL facility. While low-power heater rod set (geometry A) operates with Zr-4 cladding and integral flow channel (with containment pipe), a high-power heater rod set (geometry B) operates with same Zr-4 cladding but only partial flow channel (a ceramic shell layer is installed between the containment pipe and the cladding). For the exponential heat increasing rate, geometry A is considered for both TRTL facility and this study. Both heater rods have a 50 *in.* of total length and a 24 *in.* of heat generating length. The heat generating length is between 12 *in.* to 36 *in.* from the bottom of heater rod. The geometries are summarized in Table. 6, Fig. 20, and Fig. 21.

Table. 6. Geometries of TRTL test section

	Cladding		Pipe	Ceramic shell
	Inner diameter	Outer diameter	Inner diameter	Inner diameter
Low-power heater rod set	0.305 *in.*	0.375 *in.*	2.125 *in.*	N/A
High-power heater rod set	0.305 *in.*	0.375 *in.*	2.125 *in.*	0.75 *in.*

Inner Pipe: 2.125 *in.*
Ceramic shell: 0.75 *in.*
Outer cladding: 0.375 *in.*
Inner cladding: 0.305 *in.*

Flow region
Solid region

Low-power heater rod   High-power heater rod
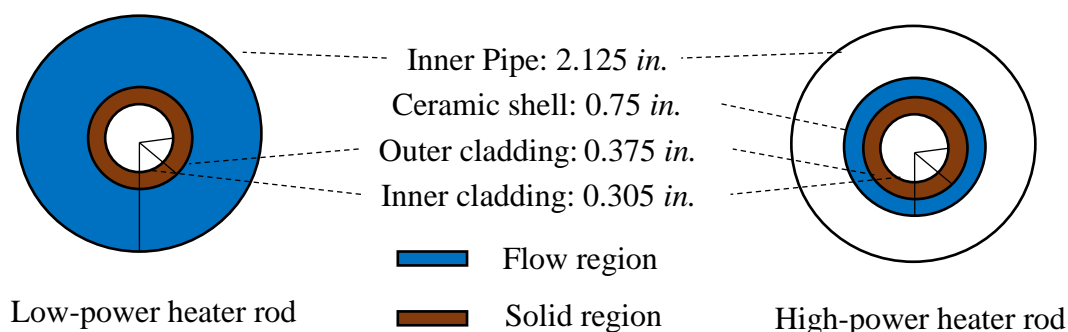
Fig. 20. Cross view of test section with different heater rod sets

g

0 *in.*   12 *in.*   Heat generating section   36 *in.*   50 *in.*
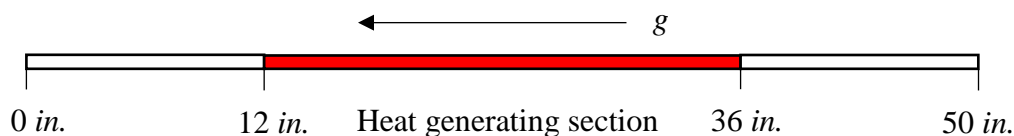
Fig. 21. Side view of heat generating section

3.3.1 Cladding Heater Boundary Conditions

To present the influence of turbulence and viscosity, the surface condition of the heater surface is set as non-slip surface. The surface roughness of the non-slip surface is keeping as the default setting. The boundary heat transfer condition is setting as adiabatic boundary for both inner and outer cladding surface. In addition, a total heat source is set for the solid region to present the heat transfer behavior between solid and fluid region. Table. 7 and Table. 8 has listed all the thermal specifications for wall type boundary and energy source specification for region that available in Star-CCM+. To simulate a heat generating section between 12 *in.* and 36 *in.*, a field function is set for the total heat source as

$$(\$\${position}[1] >= 0.3048 \& \&\$\${position}[1] <= 0.9144) \quad \text{total heat source} : 0 \, . \qquad (3.1)$$

In the realistic manner, the energy distribution of a heater rod should perform with a cosine function. However, with the relatively slow velocity of the coolant compared to extremely short heating period (high heat generating ratio), the heat input profile is considered as equally on everywhere of the cladding surface in this study. The exponential power output is set using a field function as

$$(p_0 * \exp(1/\tau * \${time})) \, . \qquad (3.2)$$

Before the beginning of each transient simulation, the temperature of the water bulk is heated until the subcooling is less than 5 $°K$ by the precursor simulation. This process is not only used to catch the same status of the experimental application within TRTL facility but also used obtain a well converged initial condition before the transient begin. The power to approach such initial condition are 10 kW and 2.4 kW for geometry A and B, respectively. In (3.2), p_0 is the power output from the initial condition and τ is the exponential heating period. In this study, the benchmark simulation is processing with heating period of 50 ms, 75 ms and 100 ms.

Table. 7. Energy specification for region source in Star-CCM+

Energy source specification	Description
Volumetric heat source	Specified a user-defined heat source with W/m^3.
Total heat source	Specified a user-defined heat source with W.
Specific heat source	Specified a user-defined heat source with W/kg.
Heat exchanger	Specified a heat exchanger term.

Table. 8. Thermal specification for wall type boundary in Star-CCM+

Thermal specification	Description
Adiabatic	No heat transfer across the boundary is permitted.
Temperature	User-specified temperature.
Convection	Consider only convective heat flux between external side of boundary and environment.
Environment	Consider both convective and radiative heat flux between external side of boundary and environment.
Heat flux	User-specified heat flux.

3.3.2   Pipe Boundary Conditions

The pipe boundary in this study can be separated to four parts: pipe inlet, pipe outlet, pipe wall and, interface between the heater and pipe region. Table. 9 shows all different boundary types that available for fluid region in Star-CCM+. For pipe inlet, since the viscosity is calculated based on the velocity profile, a velocity inlet is adopted to help improving early diverged issue. Due to EMP model phase treatment, a specification of 0 vapor volume fraction may cause unnecessary instability. Thus, a small vapor volume fraction which is 1E-4 is set up for pipe inlet boundary. To include the influence of changing density and other properties in fluid region, the equation of states of both liquid and steam are modeled by IAPWS-IF97 steam table. In order to provide a more accurate prediction for compressible flow, a pressure type outlet is set for pipe outlet boundary. The extrapolated vapor volume fraction set for pipe outlet boundary is able to prevent the back flow from the pressure type outlet. Same as the setting for cladding surface, pipe wall and heater-coolant interface are set as non-split boundary to reflect the influence of viscosity. Table. 10 summaries all the boundary type setting for fluid region in this study.

Table. 9. Available boundary types for fluid region in Star-CCM+

Boundary		Description
Inlet	Velocity	User-specified velocity for inlet.
	Mass flow	User-specified mass flow for inlet.
	Stagnation	The flow is complete at rest upstream. Typically, work with compressible flow.
Outlet	Pressure	User-specified pressure for outlet
	Flow split	User-specified split ratio for outlet between 0 and 1.
Symmetry plane		An imaginary plane of symmetry.
Wall		An impermeable surface.

Table. 10. Boundary type settings for the fluid region

Boundary	Type	Velocity	Pressure	Temperature	Volume fraction	Back flow specification
Pipe inlet	Velocity	4 *m/s*	N/A	330 *°C*	[0.9999,1E-4]	N/A
Pipe outlet	Pressure	N/A	2000 *psi*	335.48 *°C*	Extrapolated	Extrapolated
Pipe wall	Wall	N/A	N/A	Adiabatic	N/A	N/A
Heater-coolant interface	Wall	N/A	N/A	CHT	N/A	N/A

3.3.3   Conjugate Heat Transfer and Interface Types

An overlap of boundary is not allowed during mesh generating. If the simulated geometry is built by two independent geometries which are directly corresponding to fluid region and solid region, an overlapped boundary is very likely formed. To solve the issue, a subtraction Boolean, graphically shown in Fig. 22, is applied for generating geometry. Boolean is a geometry generating method which is commonly used for solving mesh problems or creating regions. By the Boolean operation, two boundaries belong to two independent contacted geometries can be generated with a small distance without overlapping.

Overlap boundary

Non-overlap boundary
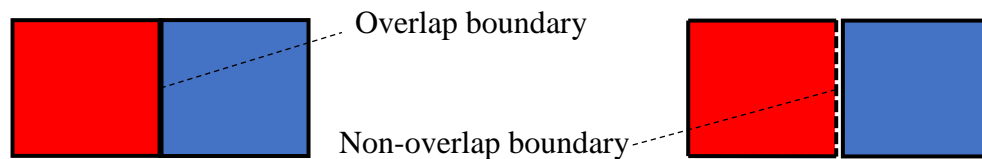
Fig. 22. Graphic depicting Boolean subtract function in Star-CCM+

Recall that the boundary for both cladding and fluid region are set up with adiabatic boundary and the thermal specification for cladding region is set up with total heat source. To track the heat transfer between two regions, The CHT method, as shown in Fig. 23, is used in this study. Different from specifying the heat flux and temperature profile on the boundary, CHT method allows the information of heat profile communicating between two contacted regions by creating an interface between regions.
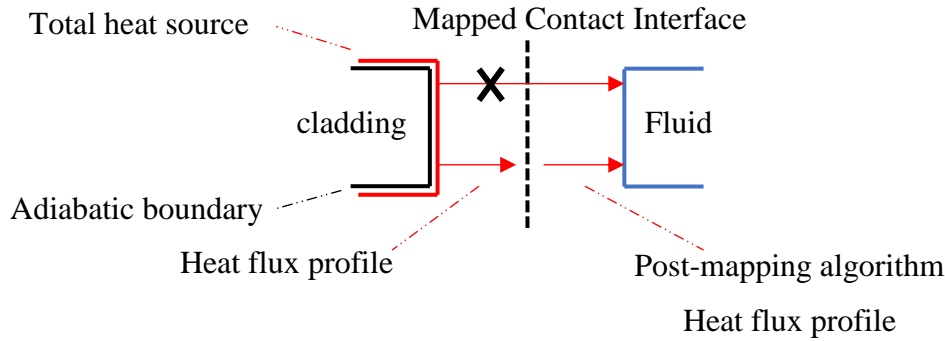
Fig. 23. Sketch of CHT method and mapped interface

The EMP simulations that includes heat transfer or boiling is extremely complicated and fragile. Typically, a conformal interface is necessary for CHT method, however, the generating of conformal interface is not supported by trimmed mesh set in Star-CCM+. The reason why conformal mesh is so crucial is that, for some of the critical locations or areas with high heat flux, a non-conformal interface may lead to inaccurate calculation for the conductive or convective heat transfer on the interface. As discussed in chapter 2.3.1, it is important to generate prism layer cells on the surface to resolve the viscosity and the turbulent. If one side of the interface is solid region, a mapped contact interface as shown in Fig. 23, can provide a solution for dealing with non-conformal issues on the mesh set for CHT simulation. With mapped contact interface, a mapping algorithm can be used for transferring information between two sides of the interface. The mapping algorithm splits surface to two categories, the associated face-set is transferred to the interface boundary while the unassociated face-set is remaining on the original boundary. During the study, it is found out that, though mapped contact interface provides an alternative solution for dealing with non-conformal interface, it fails to provide a reasonable physics and corresponding CHF. Thus, trimmed mesh set and corresponding mapped contact interface may not be suitable for the simulation with fast changing boundary conditions or high heat input.

If polyhedral mesh is decided for the core mesh, then, a conformal interface can be set up by generating the mesh for both regions simultaneously. In this case, the faces of each cell are matched which means the heat flux profile can be directly communicated between

regions. Fig. 24 shows a comparison of conformal interface built by polyhedral mesh set and a non-conformal interface built by trimmed mesh set. It should be noticed that, it is found out in this study, the conformal interface is necessary for the prediction of transient CHF. Thus, all the results from this study are provided under the frame of polyhedral mesh and conformal interface.
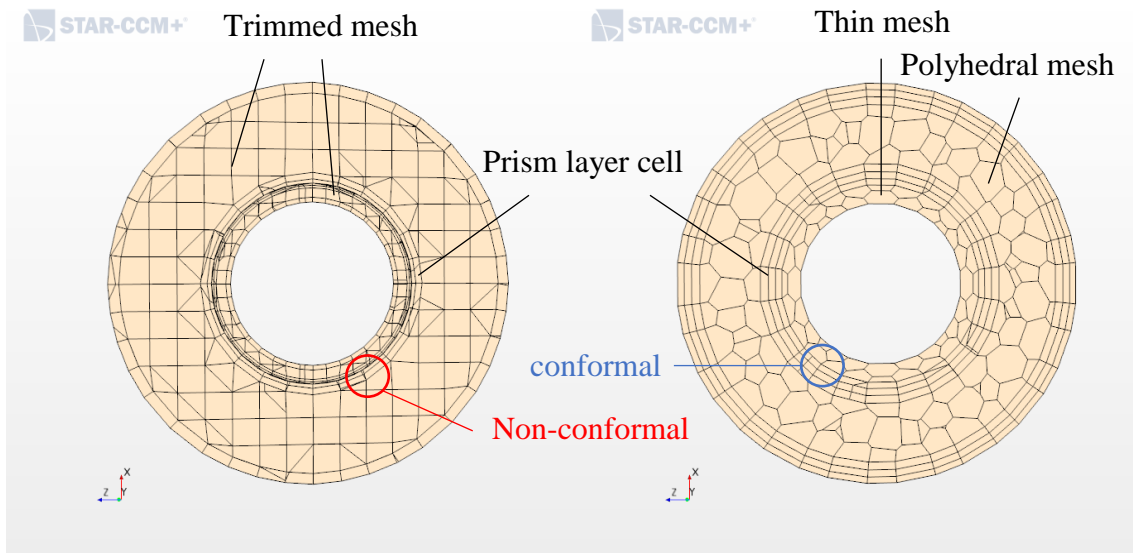
Fig. 24. Comparison of conformal interface: (left) non-conformal, (right) conformal

3.4 Grid Refinement Method

The purpose of the grid independent study is to ensure the result from the simulation is not highly influenced by the mesh size, especially, in the critical area. This section is discussing the method used for developing grid independent study including, mesh generating mode, how meshes are refined, and the mesh diagnosis reports.

3.4.1 Mesh Types and Generating Modes

Trimmed meshes provide a robust and efficient performance for simulation. The cell with hexahedral shape has a near perfect cell quality, face validity and volume change ratio among all the cells with other shape. Trimmed mesh set remains hexahedral cells in most of the simulating region except the region near the boundary. Combined with the using of

prism layer cell on the boundary, an accurate calculation is assured for most kind of simulation. It should be noticed that, due to the generating algorithm, a conformal interface is not allowed for trimmed mesh set. The generating mode of trimmed mesh is given as following and graphically shown in Fig. 25.

- Defining the boundary region (for prism layer cell) and core region (for hexahedral cell).
- Generating hexahedral cells for all the regions.
- Removeing the hexahedral cells on the boundary by trimming the excess part in the boundary region.
- Generating prism layer in the boundary region.
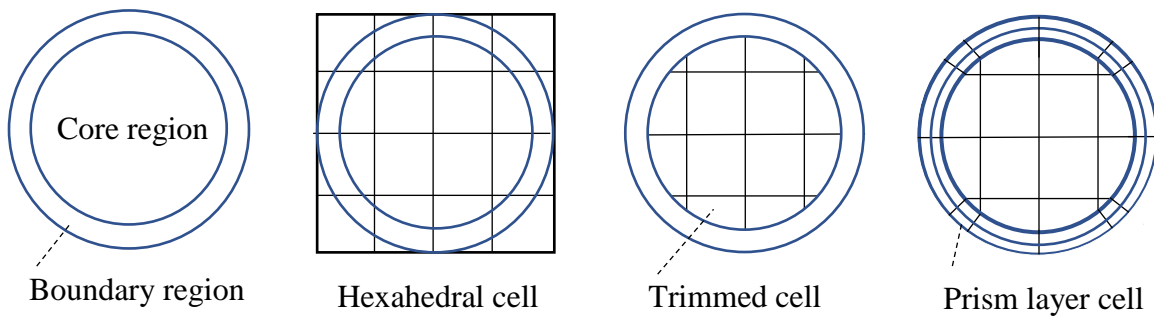
Fig. 25. Graphic of trimmed mesh model generating mode

Polyhedral meshes provides a balanced solution for complicated geometry. A typical polyhedral mesh is combined with 14 faces which means more information is transferred between cell to cell. It is foreseeable that the stability of the simulation is weakened by the increasing calculation. Though the robustness of the polyhedral meshes is relatively poor than the trimmed meshes, the accuracy of the solution is highly enhanced due to the increasing number of faces between cells. The most significant contribution from the polyhedral meshes is that the conformal interface is allowed with the polyhedral mesh generating algorithm. Different from trimmed mesh set, the prism layer cells are generated prior to the core mesh when the polyhedral mesh set is considered. Thus, a conformal interface can be formed with the consistency of prism layer cell and heater surface cell. In

this study, it is proved that the conformal interface is required under the frame of CHT method. A non-conformal interface may lead to unrealistic prediction of heat flux.

Thin meshes is a special category of mesh set which can only be activated when polyhedral mesh is set as the core mesh model. Thin mesh model create prismatic shaped meshes in the region which is considered with extremely thin geometry, for example, baffle and cladding. The cell quality and face quality can be significantly increased by the thin meshes which leads to a strong improvement of the robustness. In this study, the solid region (cladding heater) is meshed by the thin mesh model and the cell size of thin meshes is maintained during the refinement.

3.4.2 Mesh Refined Method

According to several CFD studies in the past, for example (Kim et al., 2016), there are two features of the mesh behavior should be noticed under the frame of two-phase simulation.

- First, the refinement in the water bulk region do not have a significant influence on the heat transfer behavior near the heating surface.
- Second, an over refinement on the surface mesh may lead notable instability for the two-phase simulation.

Both features are confirmed by the support from CD-Adapco and considered as principles for the mesh refinement method in this study. To acquire a reasonable number of cells across the pipe, the base size of the polyhedral meshes is set as 0.05 *in.* in the fluid region and is not refined during the grid independent study. Similar method is also applied in the solid region, the size of the thin mesh is set as 0.035 *in.* to result a two layers thin mesh set in the solid region.

As reported by the support from the CD-Adapco, an "over-refined" of the surface mesh size is approximately 0.2 *mm*, however, such "over refinement" is changing case by case. Thus, it is necessary to determine the minimum cell size which can be used for the study. To test the mesh behavior during the refinement, the refinement is applied with following steps:

- Constant core mesh base size of 0.1 *in.*

- Decreasing the wall thickness (thickness of first prism layer on the heated surface) until reaching the lower limit which may cause significant instability.

- Maintaining the mesh growth rate (the size ratio between core mesh and prism layer) at about 40 percent.

- Maintaining the stretch factor (the size ratio between each prism layer) between 1.1 to 1.3.

- Calculating the needed number of layers for prism layer cell.

Due to the consideration of the mesh growth rate and the prism layer stretch factor, the total thickness of the prism layer is about 0.04 *in.*, however, depends on cases. The resulting number of layers for prism layer cells is between one to three. The criteria for mesh growth rate and stretch factor are recommended by (CD-adapco, 2018) and are well adopted to provide a most stable simulation process. Fig. 26 shows a comparison of the cases with 0.3 *mm* and 0.5 *mm* wall thickness. Table. 11 summaries the information of different mesh sets that used in the grid independent study.
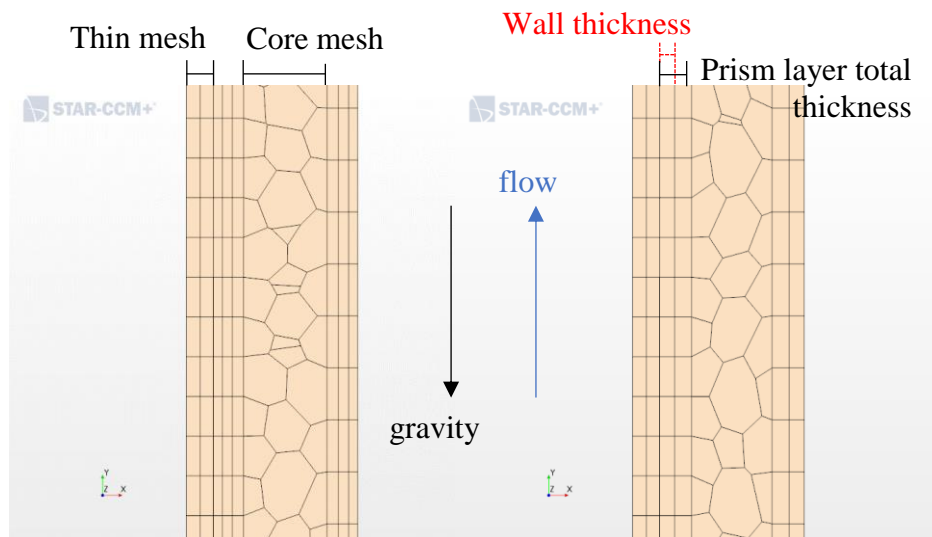
Fig. 26. Comparison of wall thickness 0.3 mm (left) and 0.5 mm (right)

Table. 11. Overview of mesh sets for grid refinement study

Core mesh base size (*in.*)	Wall thickness (*mm*)	Number of prism layer	Prism layer total thickness (*in.*)	Stretch factor
0.1.	0.3	3	0.04	1.12378
	0.4	2	0.033	1.0995
	0.5	2	0.042	1.1336
	0.75	1	0.02952	N/A
	1.0	1	0.03937	N/A

3.4.3   Mesh Diagnosis

Due to the stability issues that occurred in this study, it is important to check the mesh quality after the mesh set is generated. Though the geometry performed in this study is simplified, yet, the unstable of the two-phase simulations may amplify a tiny defect on the mesh to a significant issue of divergence, especially on the interface between solid region and fluid region. Star-CCM+ provides a diagnosis tool which is allowing user to check the mesh quality by several general approaches. Some typical mesh qualities used to determine the integral of the mesh set are listed below:

- Face validity: The correctness of face normal relative to their cell centroid. A good face validity indicates the face normal point outward the cells. A cell with face validity less than 1.0 is considered as bad cell.

- Cell quality: Typically decided by the distance between cell centroid and each face. A good cell quality indicates the distance from centroid to each face are almost nearly the same. A cell with cell quality less than 1.0E-5 is considered as bad cell.

- Volume change: The ratio of volume for a cell to its largest neighbor. A cell with volume change less than 0.01 is considered as bad cell.

- Skewness angle: The angle of the straight line of two cell centroids and its corresponding face normal. A cell with skewness angle greater than 85° is considered as bad cell.

Table. 12 summarizes all the parameters and corresponding standards that mentioned above. As a short conclusion, the mesh diagnosis shows a good agreement to the standards for all the mesh properties. It is worthy to mention that the mesh diagnosis report only

provides the value of face validity and volume change. To acquire the value of cell quality and skewness angle, an additional threshold scene is necessary to be used. Fig. 27 shows an example of diagnosis report for the mesh set with wall thickness of 0.3 *mm*.

Table. 12. Mesh diagnosis for the mesh set

Wall thickness	Minimum face validity	Minimum cell quality	Minimum volume change	Maximum skewness angle
0.3 *mm*	1.0	0.04315	1.8925E-2	54.48°
0.4 *mm*	1.0	0.08610	1.4846E-2	49.50°
0.5 *mm*	1.0	0.08529	2.6706E-2	47.00°
0.75 *mm*	1.0	0.13423	2.1508E-2	44.22°
1.0 *mm*	1.0	0.13287	2.4522E-2	47.99°
Standard	>1.0	>1E-5	>0.01	<85.00°

```
----------------------------------------------------
--- Computing statistics in Region: fluid
----------------------------------------------------
-> ENTITY COUNT:
   # Cells: 230210
   # Faces: 1052928
   # Verts: 720154
-> EXTENTS:
   x: [-9.4768e-03, 9.4768e-03 ] m
   y: [0.0000e+00 , 1.2700e+00 ] m
   z: [-9.4816e-03, 9.4816e-03 ] m
-> MESH VALIDITY:
   Mesh is topologically valid and has no negative volume cells.
-> FACE VALIDITY STATISTICS:
Minimum Face Validity: 1.000000e+00
Maximum Face Validity: 1.000000e+00
         Face Validity <  0.50              0     0.000%
0.50 <= Face Validity <  0.60              0     0.000%
0.60 <= Face Validity <  0.70              0     0.000%
0.70 <= Face Validity <  0.80              0     0.000%
0.80 <= Face Validity <  0.90              0     0.000%
0.90 <= Face Validity <  0.95              0     0.000%
0.95 <= Face Validity <  1.00              0     0.000%
1.00 <= Face Validity                 230210   100.000%
-> VOLUME CHANGE STATISTICS:
Minimum Volume Change: 1.892501e-02
Maximum Volume Change: 1.000000e+00
         Volume Change <  0.000000e+00            0     0.000%
0.000000e+00 <= Volume Change <  1.000000e-06           0     0.000%
1.000000e-06 <= Volume Change <  1.000000e-05           0     0.000%
1.000000e-05 <= Volume Change <  1.000000e-04           0     0.000%
1.000000e-04 <= Volume Change <  1.000000e-03           0     0.000%
1.000000e-03 <= Volume Change <  1.000000e-02           0     0.000%
1.000000e-02 <= Volume Change <  1.000000e-01         331     0.144%
1.000000e-01 <= Volume Change <= 1.000000e+00      229879    99.856%
```

Fig. 27. An example of Star-CCM+ for compact mesh diagnosis for 0.3 mm mesh set

3.5   Setting of General Models and Eulerian Phases Material

For multiphase heat transfer simulations, Star-CCM+ provides a considerable number of models. Typically, the setting can be categorized as three steps: setting of general models, setting of Eulerian phases material, and setting of multiphase interaction models. Depends on the using of different multiphase model, the order of settings may be presently slightly different. The model setting process for VOF and EMP are shown in Table. 13.

Table. 13. Model setting process for VOF and Multiphase segregated flow simulation

Simulation	General models	Eulerian multiphase material	Phase interaction
VOF	• Time • Space • Material • Viscous regime • Turbulent	Material properties of: • Liquid phase • vapor phase • Mixture phase	• Rohsenow boiling • Primary/secondary phase specification • Phase interaction material properties
EMP	• Time • Space • Material • Viscous regime	Material properties of: • Liquid phase • Vapor Phase Turbulent model of: • Liquid phase • Vapor phase	• Wall boiling • Continuous/dispersed phase specification • Phase interaction material property • Interphase mass transfer

3.5.1   General Models

This section provides the entire process of setting general models. In Star-CCM+, there is no specific category of models named general models, however, this part summarizes those models which are not included in the Eulerian multiphase material and phase interaction. Chapter 3.8 details all the models and their corresponding setting utilized to support this study.

Flow solver decides how continuous, momentum and energy equation be solved. In Star-CCM+, flow solver is not directly selected by the user. However, when Eulerian multiphase models are set up, segregated flow solver is appeared as a default setting. It should be noticed that Star-CCM+ provides only segregated method for boiling simulations.

Segregated flow solver solves continuous and momentum equation without energy equation at same time while coupled flow solver solves all three equations synchronously. Such characteristic leads to different performance of accuracy, stability and efficiency for two solvers. Table. 14 has summarized the characteristics for both solvers. Under the frame of segregated flow solver, the continuous, momentum and energy conservation equation for independent phase *i* and *j* can be written as (3.3), (3.4) and (3.5), respectively.

$$\frac{\partial}{\partial t}\int_v \alpha_i\rho_i dV + \oint_A \alpha_i\rho_i v_i \cdot dA = \int_v \sum_{j\neq i}(m_{ij} - m_{ji})dV + \int_v S_i^m dV \tag{3.3}$$

$$\frac{\partial}{\partial t}(\int_v \alpha_i\rho_i v_i)dV + \oint_A \alpha_i\rho_i v_i \otimes v_i \cdot dA$$
$$= -\int_v \alpha_i\nabla p dV + \int_v \alpha_i\rho_i g dV + \oint_A \left[\alpha_i(T_i^m + T_i^t)\right]\cdot dA + \int_v M_i dV \tag{3.4}$$
$$+\int_v (F_{int})_i dV + \int_v S_i^M dV + \int_v \sum_{i=1}^n (m_{ij}v_j - m_{ji}v_i)dV$$

$$\frac{\partial}{\partial t}\int_V \alpha_i\rho_i E_i dV + \oint_A \alpha_i\rho_i H_i v_i dA + \oint_A \alpha_i p dA$$
$$= \oint_A \alpha_i k_{eff,i}\nabla T_i dA + \oint_A T_i \cdot v_i dA + \oint_A f_i v_i dV + \int_V \sum_{j\neq i} Q_{ij} dV \tag{3.5}$$
$$+\int_V \sum_{(ij)} Q_i^{(ij)} dV + \int_V S_i^E dV + \int_V \sum_{j\neq i}(m_{ij} - m_{ji})h_i(T_{ij})dV$$

Table. 14. Characteristics of segregated and coupled flow solver

	Segregated flow solver	Coupled flow solver
Equations	• Continuous and momentum equations are solved at same time. • Then, solve energy equation.	Continuous, momentum and energy equations are solved at same time.
Advantage	• Less computational cost. • Less CPU hours.	• Stable for compressible flow. • More accurate.
Disadvantage	Non-linear computational cost.	Time costing to converge.
Compatible	Eulerian and Lagrangian method.	Only for Lagrangian method.

For the time model, there are five models, as shown in Table. 15, that available for the different consideration. For transient simulation, four unsteady state models can be selected. However, only implicit unsteady state is satisfied the requirement of multiphase heat transfer and is compatible with segregate flow solver which is the flow solver used

for multiphase boiling simulation. Fig. 28 shows how segregated flow solver works under the frame of implicit unsteady state model.

Table. 15. Temporal models in Star-CCM+

Time model		Description	Compatible
Transient	Explicit unsteady state	Time step is defined by the convergence of coupled flow solver.	Coupled flow solver
	Implicit unsteady state	User-specified constant time step.	Segregated flow and coupled flow solver
	PISO unsteady state	User-specified constant time step which involves predictor and corrector inner iteration.	Not supporting Eulerian multiphase flow
	Harmonic balance	Designed for unsteady problems with periodic physics phenomenon.	
Steady state	Steady state	Applied for steady state cases.	
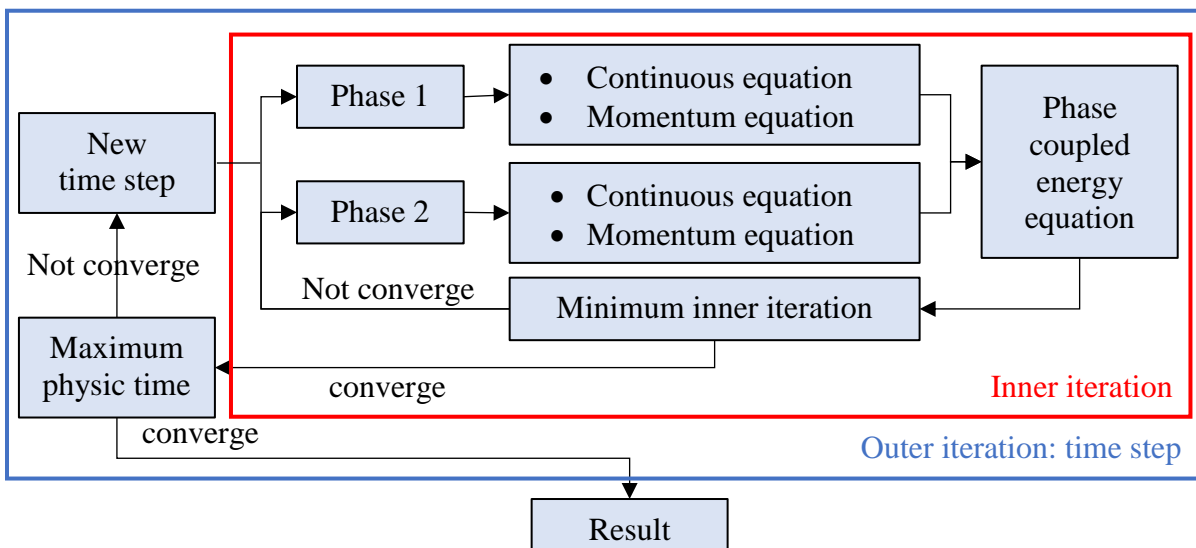
Fig. 28. Flow chart of process for segregated flow solver with implicit time step

Four different models are available for modeling space. The choice here stands for three-dimension model which is used for 3-D simulation. The other three different models are: axisymmetric, shell three-dimension and two-dimension model. Axisymmetric and two-dimension are used for 2-D simulation while previous applied for 2-D symmetry geometry

and later applied for all 2-D geometry. Shell three-dimension is compatible with the geometries have extremely small thickness which can be considered as only one cell.

Star-CCM+ provides several selections of model for different material type. The most common choices are the single-phase material including solid, liquid and gas. The multi-component material model is provided for the consideration of same independent phases, for example, multi-component solid. However, for the multiphase boiling simulations, the Eulerian multiphase material model is the only choice. Once the model is activated, a model node named "Eulerian multiphase" will be added into the physical model tree and the detailed models for defining phases and phase interaction are ready for the selection.

The viscous regime decides the flow behavior close to the wall boundary. The options provided in Star-CCM+ are inviscid, laminar and turbulent. To simulate the influence of viscosity on the heater surface, turbulent viscous regime is selected in this study. It should be noticed that if EMP model is used, the further setting for turbulent models should be completed in the Eulerian phase material node. In the contrast, for the VOF model, the option will show up automatically. Since VOF model treats multiphase as single mixture phase, only one turbulent model is needed to be specified. For EMP model, two independent turbulent models is necessary for different phase material.

3.5.2   Eulerian Multiphase Material

In this study, the studied transient CHF is focusing for the pressure of 2000 *psi*. In a PWR reactor, the operating pressure is 2250 *psi* which is also the original design in this study. However, during the study, it is found out that such setting leads to potential instability from the build-in steam table. To keep simulations as simple as possible for the stability concern, the objective pressure is switch to a lower level.

The built-in steam table, IAPWS-IF97, is attributed to the equation of state model for this study. IAPWS-IF97 provides a broad range of water properties shown in Fig. 29 and Table. 16. The provided properties are included in Table. 17. If the liquid model for material is activated under the model node of Eulerian multiphase, IAPWS-IF97 can be directly

selected in equation of state. However, in gas model, a real gas model should be activated in equation of state before IAPWS-IF97 be selected.
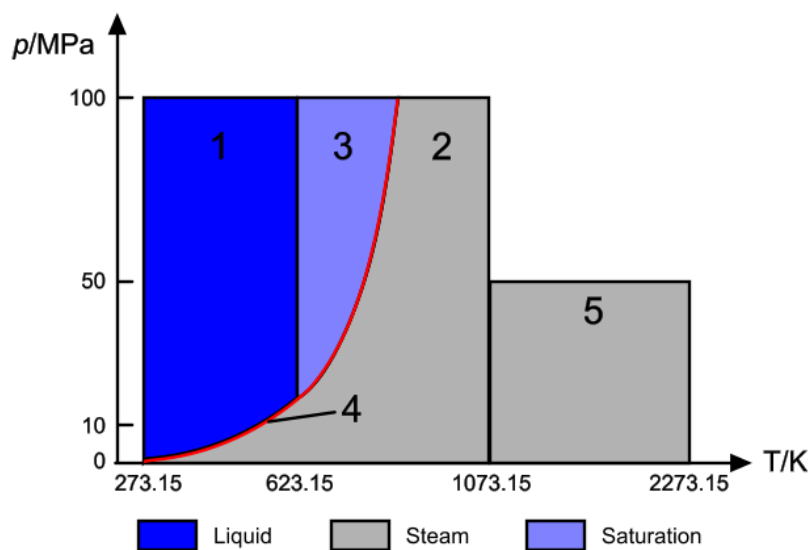
Fig. 29. Graphic of applied range for IAPWS-IF97

Table. 16. Range values within applied range for IAPWS-IF97

Region/boundary	Range		IAPWS-IF97
	Temperature (*K*)	Pressure (*MPa/Psi*)	
1	$273.15 \leq T \leq 623.15$	$p \leq 100$ (14503.77)	Water
2	$273.15 \leq T \leq 1073.15$	$p \leq 100$ (14503.77)	Steam
3	Not supported by Star-CCM+		
4	Boundary of liquid and saturation on one side, and steam on the other		
5	$1073.15 \leq T \leq 2273.15$	$p \leq 50$ (7251.885)	Steam

Table. 17. Properties supported by IAPWS-IF97

IAPWS-IF97
Dynamic viscosity
Thermal conductivity
Critical temperature
Molecular weight
Saturation temperature
Saturation pressure
Speed of sound
Entropy
Heat capacity

It should be noticed that IAPWS-IF97 is not supporting the region 3 in Star-CCM+. That is, if the simulating pressure is 2250 *psi* (15.5 *MPa*), the steam temperature higher than 623.15 °*K* is most likely to happen. It is confirmed that the potential instability introduced by this issue is lead to a diverged scenario. As a result, 2000 *psi* is set for the initial condition and pressure type outlet boundary for this study. Table. 18 provides the saturating properties for water at 2000 *psi*. The correct setting of these parameters for initial condition may prevent the simulations from early divergence.

Table. 18. Phase material property at 2000 psi

Fluid property	Water	Steam
Pressure (*psi*)	2000	
Saturated Temperature (°*C*)	335.48	
Density (*kg/m³*)	624.8678	85.1233
Dynamic viscosity (*Pa·S*)	7.23E-5	2.21E-5
Heat capacity (*kJ/kg·S*)	7.6841	10.949
Thermal conductivity (*W/m·K*)	0.4513	0.1028
Specific enthalpy/ Heat of formation (*kJ/kg·K*)	2643.49	1562.62
Surface tension (*mN/m*)	6.47	

The heat of formation is a special material property that adopted by Star-CCM+ and using for determining how much heat is evolved in one kilogram of the material when it forms from its elements. In multiphase simulation, this property also specifies the reference enthalpy at reference temperature. In (3.6), *E* is the total energy which is decided by enthalpy, pressure and density. H_i is the total enthalpy inside phase *i* which can be written as (3.7). The term h_i the can be further expressed by (3.8) and ,finally, decided by the heat of formation which is written as h^{ref}. By defining the heat of formation, the unnecessary calculation of the energy that used for phase change can be neglected, thus, improve the stability.

$$E_i = H_i - \frac{p}{\rho_i} \tag{3.6}$$

$$H_i = h_i + \frac{|v_i|^2}{2} \tag{3.7}$$

$$h_i(T_i) = h_i^{ref} + \int_{T_i^{ref}}^{T_i} C_{p,i}(T')dT' \tag{3.8}$$

Surface tension is a crucial property which should be accounted in boiling process. The surface tension can only be set up under the node of multiphase material model when phase interaction models is entirely defined. During the process of setting up VOF models by using IAPWS-IF97 as equation of state, the simulation is not able to initialize in the first iteration. After detailed inspection, it is found out that VOF simulation is not compatible when using IAPWS-IF97 as surface tension reference. As a result, the surface tension is set as 6.47 *mN/m* for the VOF simulations. To detail the reason, a further discussion with CD-Adapco is needed.

The material properties for cladding heater is set up using material properties of Zr-4. The setting of solid region is relatively simple compared to fluid region since only solid phase and constant density are considered. Segregated solid energy model is selected in optional model for the purpose of calculating the heater transfer between solid and fluid region. Due to the fact that the influence of thermal expansion in the solid region is not the purpose, the simulations are simplified with the concern of stability concern. The summary of the models and corresponding setting in solid region is shown in Table. 19.

Table. 19. Models and properties setting for solid region

Modeling	Models
Material	Solid
Equation of state	Constant density
Optional	Segregated solid energy
Properties	Zr-4
Density (kg/m^3)	6560
Heat capacity ($kJ/kg·k$)	0.285
Thermal conductivity ($W/m·K$)	21.5

3.5.3   Modeling Turbulent Flow

Recall the discussion in chapter 2.3.2, realizable k-ε two-layer (RKE-2L) is selected as the turbulent model in this study. In VOF simulations, only one turbulent model is necessary to be set up for both primary and secondary phase, however, in EMP simulations, two turbulent models (can be either the same or not) are needed for continuous and dispersed phases, respectively. The reason is that, in EMP model, the dispersed phase (steam) is

treated as an independent phase instead of part of the mixture phase. To perform a robust result, in this study, different turbulent models for different phases are not considered. Table. 20 provides the turbulent model that setting for VOF and EMP model. It should be noticed that some of the setting has been modified under the instruction of support from CD-Adapco. The detail of the modification is discussed in chapter 3.7.6 from the stability manner.

Table. 20. Turbulent models considered

	Viscous regime	Phase	Turbulent	k-ε turbulent	Turbulent intensity	Turbulent viscosity ratio
VOF		Mixed			0.05	400
EMP	Turbulent	Continuous	RANS	RKE-2L	0.05	400
		Dispersed			0.05	200

The k-ε turbulent model (KE) is one of the most common models in RANS model family and is well known for its robustness and accuracy. Recall that Star-CCM+ provides two categories of turbulent model: Reynolds-Averaged Navier-Stokes turbulent model (RANS) and Scale-resolving simulations (DES and LES). RANS is always the first consideration due to the balance of performance and computational cost. In most of the cases, RANS is enough to resolve more than 90 percent of the turbulence with far away less computational cost than DES and LES. For all the solution, variables in RANS model can be expressed as

$$\phi = \bar{\phi} + \phi' , \tag{3.9}$$

where $\bar{\phi}$ and ϕ' are the averaged and fluctuating term. In the averaged momentum transport equation, an additional term of Reynolds Stress tensor is added by

$$T_t = -\rho \begin{bmatrix} u'u' & u'v' & u'w' \\ u'v' & v'v' & v'w' \\ u'w' & v'w' & w'w' \end{bmatrix} . \tag{3.10}$$

Depends on how Reynolds stress tensor is solved, RANS can be subdivided into two categories: eddy viscosity models and Reynold stress transport models. In eddy viscosity models,

$$T_t = 2\mu_t S - \frac{2}{3} (\mu_t \cdot \bar{v}) I , \tag{3.11}$$

is used to solve Reynolds stress tensor, where I is the identify tensor, μ_t is the turbulent eddy viscosity and S is the mean strain tensor shown as

$$S = \frac{1}{2}\left(\nabla\bar{v} + \nabla\bar{v}^T\right).$$ (3.12)

For all the KE models, the transported variables, turbulent kinetic energy (k) and turbulent dissipation rate (ε), are solved for the resolving of the turbulence. Star-CCM+ provides two different method to specify these transported variables. For the default setting adopted in these study, the term k and ε are specified using the turbulent intensity and turbulent viscosity ratio shown as (3.13) and (3.14), respectively.

$$k = \frac{3}{2}(Iv)^2,$$ (3.13)

$$\varepsilon = \frac{\rho C_\mu k^2}{(\frac{\mu_t}{\mu})\mu},$$ (3.14)

where I and μ_t/μ are turbulent intensity and turbulent viscosity ration, respectively. The term C_μ is a coefficient, given by (3.19), depends on the variants of KE model.

Under the frame of eddy viscosity models, the RKE-2L model is a variant model of SKE model which is combining RKE model with two-layer method. The term turbulent eddy viscosity (μ_t) in RKE-2L can be further expressed as

$$\mu_t = \rho C_\mu f_\mu \frac{k^2}{\varepsilon},$$ (3.15)

where f_μ is a damping function written as

$$f_\mu = \frac{1}{C_\mu\left\{4 + 6^{0.5}\cos\left[\frac{1}{3}\cos^{-1}\left(6^{0.5}\frac{S*^3}{(S*:S*)^{1.5}}\right)\right]\frac{k}{\varepsilon}(S:S + W:W)^{0.5}\right\}}.$$ (3.16)

The term S^* and W (module of mean velocity tensor) can be further expressed by (3.17) and (3.18), respectively.

$$S* = S - \frac{1}{3}\text{tr}(S)I.$$ (3.17)

$$W = \frac{1}{2}(\nabla \overline{v} - \nabla \overline{v}^T) . \tag{3.18}$$

The most significant difference between RKE and SKE is that the coefficient, C_μ, is no longer a constant coefficient. In RKE model, C_μ is calculated form the mean strain rate tensor (S) and the module of mean velocity (W) as

$$C_\mu = \frac{C_{a,0}}{C_{a,1} + C_{a,2}\overline{S} + C_{a,3}\overline{W}} , \tag{3.19}$$

where,

$$\overline{S} = \frac{k}{\varepsilon}(2S:S)^{0.5} , \tag{3.20}$$

and

$$\overline{W} = \frac{k}{\varepsilon}(2W:W)^{0.5} . \tag{3.21}$$

As a two-equation turbulent model, RKE-2L uses two transport equations to solve the behavior of turbulent kinetic energy (k) and turbulent dissipation rate (ε). The transport equations for k and ε can be written as (3.22) and (3.27) respectively.

$$\frac{\partial}{\partial t}(\rho k) + \nabla \cdot (\rho k \overline{v}) = \nabla \cdot \left[\left(\mu + \frac{\mu_t}{\sigma_k} \right) \nabla k \right] + P_k - \rho \varepsilon , \tag{3.22}$$

where σ_k is the turbulent kinetic energy coefficient and P_k is the production term of turbulent kinetic energy. The production term for turbulent kinetic energy can be further expressed as

$$P_k = G_k + G_b + \gamma_M , \tag{3.23}$$

where G_k, G_b and γ_M are turbulent production, buoyancy production and compressibility modification which are showed as (3.24), (3.25) and (3.26), respectively.

$$G_k = \mu_t S^2 - \frac{2}{3}\rho k \nabla \cdot \overline{v} - \frac{2}{3}\mu_t (\nabla \cdot \overline{v})^2 . \tag{3.24}$$

$$G_b = -\frac{1}{\rho}\frac{\partial \rho}{\partial \overline{T}}\frac{\mu_t}{\text{Pr}_t}(\nabla \overline{T} \cdot g) , \tag{3.25}$$

where Pr_t is the turbulent Prandtl number and $\overline{T}$ is the mean temperature.

$$\gamma_M = \frac{C_M k\varepsilon}{c^2}, \tag{3.26}$$

where C_M is the coefficient and c is the speed of sound.

$$\frac{\partial}{\partial t}(\rho\varepsilon) + \nabla \cdot (\rho\varepsilon\bar{v}) = \nabla \cdot \left[\left(\mu + \frac{\mu_t}{\sigma_\varepsilon}\right)\nabla\varepsilon\right] + \frac{\varepsilon}{k}\left(C_{\varepsilon,1}P_\varepsilon - C_{\varepsilon,2}f_2\rho\varepsilon\right), \tag{3.27}$$

where σ_ε, $C_{\varepsilon,1}$ and $C_{\varepsilon,2}$ are the coefficients for turbulent dissipation rate transport equation and P_ε is the production term of turbulent dissipation rate which can be expressed as

$$P_\varepsilon = Sk + C_{\varepsilon,3}G_b, \tag{3.28}$$

where $C_{\varepsilon,3}$ is the coefficient. Again, f_2 is a damping function, written as

$$f_2 = \frac{k}{k + (v\varepsilon)^{0.5}}. \tag{3.29}$$

The two-layer method is an alternative approach for traditional KE model to resolve the turbulent behavior at near wall prism layer cell (viscous sublayer). In the near wall region, ε and μ_t are specified as a function of wall distance. Then, a blended function of

$$B = \exp(-\frac{\text{Re}_y}{11}) = \exp(-\frac{1}{11}\frac{k^{0.5}y}{v}), \tag{3.30}$$

is used in the buffer layer region by blend the turbulent from the viscous sublayer region and the log-law region smoothly. Combining with all y^+ wall treatment, the reference velocity (u^*), turbulent production (G_k) and turbulent dissipation rate (ε) are modified inside the near wall cell by (3.31), (3.32) and (3.33), respectively.

$$u^* = \left(\frac{Bvu}{y} + (1-B)C_\mu^{0.5}k\right)^{0.5}. \tag{3.31}$$

$$G_k = B\mu_t S^2 + (1-B)\frac{1}{\mu}(\rho u^*\frac{u}{u^+})^2\frac{\partial u^+}{\partial y^+}. \tag{3.32}$$

$$\varepsilon = g\frac{2vk}{y^2} + \frac{k^{1.5}}{l_\varepsilon}. \tag{3.33}$$

In Star-CCM+, two-layer method provides three model variants to describe the turbulent behavior near the wall. The default setting, the Wolfstein approach, is a shear driven model which solves length scale function and turbulent viscosity ratio as

$$l_\varepsilon = 0.42 C_\mu^{-0.75} d \left[1 - \exp\left(-\frac{\text{Re}_w}{0.84 C_\mu^{-0.75}} \right) \right], \tag{3.34}$$

and

$$\frac{\mu_t}{\mu} = 0.42 \, \text{Re}_w \, C_\mu^{0.25} \left[1 - \exp(-\frac{\text{Re}_w}{70}) \right], \tag{3.35}$$

respectively. The Re_w in both is equations are the wall-distance Reynold number.

All the coefficients that used by RKE-2L model combining with all-y^+ wall treatment are listed in Table. 21.

Table. 21. Coefficient for RKE-2L combining with all-y^+ wall treatment

Coefficient	Value	Source
$C_{a,0}$	0.667	(3.19)
$C_{a,1}$	1.25	(3.19)
$C_{a,2}$	1	(3.19)
$C_{a,3}$	0.9	(3.19)
σ_k	1	(3.22)
σ_ε	1.2	(3.27)
$C_{\varepsilon,1}$	$\max(0.43, \frac{\eta}{\eta+5})$, where $\eta = \frac{Sk}{\varepsilon}$	(3.27)
$C_{\varepsilon,2}$	1.9	(3.27)
$C_{\varepsilon,3}$	$\begin{cases} 1 \text{ for } G_b \geq 0 \\ 0 \text{ for } G_b < 0 \end{cases}$	(3.28)
C_M	2	(3.26)

3.6 Setting of Heat Transfer and Multiphase Interaction Models

3.6.1 Thermal Diffusion in EMP

Wall boiling model is the boiling heat transfer model that used by EMP model to simulate surface boiling. To trigger the wall boiling model, an optional model, phase coupled fluid energy, is necessary to be selected. The phase coupled fluid energy model allows the energy equations from both continuous and dispersed phase solving at the same time. In addition, EMP model requires additional model to specify the interacting area between continuous and dispersed phase. In this study, the Kurul-Podowski model is used to specify the interfacial area between two phases and the Ranz-Marshall model is used for the

calculation of Nusselt number. The algorithm that solving thermal diffusion is graphically showing in Fig. 30.
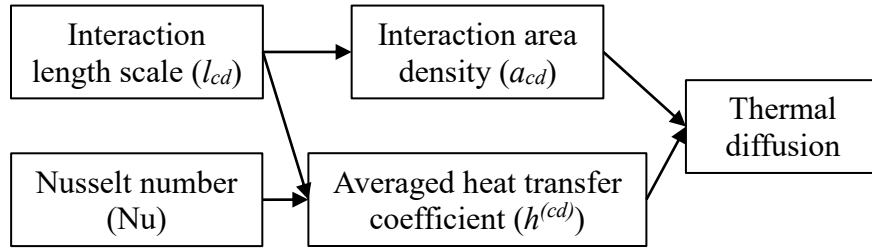
Fig. 30.Graphical algorithm of thermal diffusion

The thermal diffusion between continuous phase (*c*) and dispersed phase (*d*) is expressed as

$$Q_{cd} = -Q_{dc} = h^{(cd)} a_{cd} (T_d - T_c),$$
(3.36)

where a_{cd} is the interaction area density which is simulated by symmetric particle method and $h^{(cd)}$ is the average heat transfer coefficient. The averaged heat transfer coefficient can be further expressed as

$$h^{(cd)} = \frac{k_c \text{Nu}}{l_{cd}},$$
(3.37)

where l_{cd} is interaction length scale and k_c is the thermal conductivity of the continuous phase. The Nusselt number can be further express as

$$\text{Nu} = 2 + 0.6 \text{Re}_d^{0.5} \text{Pr}_c^{0.3},$$
(3.38)

by the using of the Ranz-Marshall correlation from (Ranz & Prog, 1952). Re_d and Pr_c in (3.38) are the dispersed phase Reynold number and continuous phase Prandtl number, respectively.

The interaction area density model is used to specify the interfacial area between phases for mass, momentum and heat transfer equations. In this study, the symmetric particle area density is used due to a wide range of applicable volume fraction, shown as

$$a_{cd} = \frac{6\alpha_c \alpha_d}{l_{cd}},$$
(3.39)

where α is the volume fraction from different phases and l_{cd} is the interaction length scale from the Kurul-Podowski method.

The interaction length scale decides the size distribution of dispersed phase. It is preferred to use the S-Gamma model, which includes the influence of particle coalescence and breakup, to predict the particle size. However, it is found out in this study that the using of the S-Gamma model significantly increases instability for the simulations and lead to a diverged scenario. As a result, the Kurul-Podowski method (Kurul &Podowski, 1990) is used as an alternative model of S-Gamma model. The Kurul-Podowski interaction length scale is written as

$$l_{cd} = \frac{D_{\min}^{d}(\Delta T_{D,\max} - \Delta T) + D_{\max}^{d}(\Delta T - \Delta T_{D,\min})}{\Delta T_{D,\max} - \Delta T_{D,\min}} \, , \tag{3.40}$$

where D_{min}^{d} is the minimum bubble diameter, D_{max}^{d} is the maximum bubble diameter, and ΔT_{D} is the corresponding liquid subcooling. The parameters that used by Kurul-Podowski method are summarized in Table. 22.

Table. 22. Parameters for interaction length scale

Parameter	Default value
$D_{\min}^{d}$	1.5E-4 m
$D_{\max}^{d}$	2E-3 m
$\Delta T_{D,min}$	13.5 $°K$
$\Delta T_{D,max}$	-5.0 $°K$

3.6.2 *Phase Momentum Transfer in EMP*

Star-CCM+ uses two-fluid model to simulate momentum transfer between continuous and dispersed phase. Under the frame of two-fluid model, phase momentum transfer can contribute to six terms which are: drag force, lift force, turbulent dispersion force, virtual mass force, wall lift force (wall lubrication force) and basset force. These six forces are list and explained below:

- Drag force: the force works on the dispersed phase that comes from the relative velocity to the continuous phase.

- Lift force: the force that perpendiculars to relative velocity due to rotation of flow in continuous phase.

- Turbulent dispersion force: the force due to the concentration difference of turbulent in the continuous phase

- Virtual mass force: the additional resistance that a particle accelerates through the continuous phase with apparent mass.

- Wall lift force: the force due to the velocity distribution changes near the wall surface which prevent the particle from touching the wall surface.

- Basset force: the effect of acceleration on dispersed phase due to the viscous drag during the period of boundary layer development.

In Star-CCM+, the interphase momentum transfer is simulated by the first four forces that mentioned above. The interphase momentum transfer can be detailed as

$$\mathrm{M}_i = \sum_{c \neq d} (F_{cd}^D + F_{cd}^L + F_{cd}^{TD} + F_{cd}^{VM}),\qquad(3.41)$$

where F_{cd}^D, F_{cd}^L, F_{cd}^{TD} and F_{cd}^{VM} represent drag force, lift force, turbulent dispersion force and virtual mass force, respectively. To keep simulation simple and robust, all the stings for four forces are maintaining default. It should be noticed that when EMP model is selected, drag force model is triggered automatically while lift force, the virtual mass force and the turbulent dispersion force are needed to be set up for the optional models.

F_{cd}^D stands for the drag force and can be expressed as

$$F_{cd}^D = A_{cd}^D (\mathrm{v}_d - \mathrm{v}_c).\qquad(3.42)$$

A_{cd}^D is the linearized drag coefficient which can be used directly or calibrated by the standard drag coefficient as

$$A_{cd}^D = C_{cd}^D \frac{1}{2} \rho_c |\mathrm{v}_d - \mathrm{v}_c| (\frac{a_{cd}}{4}),\qquad(3.43)$$

where C_{cd}^D is the standard drag coefficient. To response the influence from the concentration of particle to the drag force, a drag correction factor is added to correct standard drag coefficient, as

$$C_{cd}^D = f_{cd}^D C_{cd,\infty}^D,\qquad(3.44)$$

where $C_{cd,\infty}^{D}$ is single-particle drag coefficient and f_{cd}^{D} is drag correction factor. The default setting considered is volume fraction exponent drag correction. Star-CCM+ provides five linearized drag coefficient models and six single-particle drag coefficient models. The default setting for single-particle drag coefficient is using the result from (Tomiyama, Tamai, Zun, &Hosokawa, 2002), as

$$C_{cd,\infty}^{D} = \max\left[\min\left(\frac{24}{\mathrm{Re}}(1+0.15\,\mathrm{Re}^{0.687}), \frac{72}{\mathrm{Re}} \right), \frac{8Eo}{3(Eo+4)} \right],$$ (3.45)

where Reynold and Eotvos number can be further express by

$$\mathrm{Re} = \frac{\rho_c |\mathrm{v}_{cd}| l_{cd}}{\mu_c},$$ (3.46)

and

$$E_0 = \frac{|\rho_c - \rho_d| g l_{cd}^2}{\sigma},$$ (3.47)

respectively. The drag force that simulated by Tomiyama's method is suitable for the phases interaction with considering water bubbles as dispersed phase under a wide range condition.

F_{cd}^{L} stands for the lift force and can be expressed by

$$F_{cd}^{L} = C_{cd}^{L} \alpha_d \rho_c \left[\mathrm{v}_{cd} \times (\nabla \times \mathrm{v}_c) \right]$$ (3.48)

where C_{cd}^{L} is the lift coefficient. The default setting here is from (Lance &Bataille, 1991) which is 0.25.

F_{cd}^{TD} stands for the turbulent dispersion force which can be expressed as

$$F_{cd}^{TD} = A_{cd}^{D} D_{cd}^{TD} \cdot \left[\frac{\nabla \alpha_d}{\alpha_d} - \frac{\nabla \alpha_c}{\alpha_c} \right],$$ (3.49)

where A_{cd}^{D} is linearized drag coefficient and D_{cd}^{TD} is tensor diffusivity coefficient. The tensor diffusivity coefficient can be further detailed by

$$D_{cd}^{TD} = C_{cd}^{TD} \frac{v_c^t}{\mathrm{Pr}_\alpha^t},$$ (3.50)

where v_c^t is turbulent kinematic viscosity in continuous phase, Pr_α^t is turbulent Prandtl number according to volume fraction and, C_{cd}^{TD} is the turbulent dispersion coefficient from the default setting which is 1.0.

F_{cd}^{VM} stands for the virtual mass force which can be expressed as

$$F_{cd}^{VM} = C_{cd}^{VM} \rho_c \alpha_d \left[\frac{\partial \mathbf{v}_d}{\partial t} - \frac{\partial \mathbf{v}_c}{\partial t} \right], \tag{3.51}$$

where C_{cd}^{VM} is the virtual mass coefficient, shown as

$$C_{cd}^{VM} = \left[(C_{sphere}^{VM})^{-2} + (C_{max}^{VM})^{-2} \right]^{-0.5}. \tag{3.52}$$

C_{max}^{VM} is the limited virtual mass coefficient which is used for responding the influence from high volume fraction, written as

$$C_{max}^{VM} = \frac{1 - \alpha_d}{\alpha_d}. \tag{3.53}$$

C_{sphere}^{VM} is the spherical particle virtual mass coefficient from (Lamb, 1945) which has a default value of 0.5.

3.6.3   Wall Boiling Model in EMP

The wall boiling model under subcooled boiling condition can be expressed by

$$\dot{q}_w'' = \dot{q}_{conv}'' + \dot{q}_{evap}'' + \dot{q}_{quench}''. \tag{3.54}$$

The three terms on the right-hand side represent the contribution from convection, evaporation and quenching, respectively. These three terms are visually depicted in Fig. 31. However, under the condition with relatively high vapor volume fraction, the influence from the surface that covered by vapor should be included. The contribution from the vapor is added and (3.54) becomes

$$\dot{q}_w'' = (\dot{q}_{conv,wet}'' + \dot{q}_{evap}'' + \dot{q}_{quench}'')(1 - k_{dry}) + k_{dry} \cdot \dot{q}_{conv,dry}'', \tag{3.55}$$

where $\dot{q}_{conv,wet}''$ and $\dot{q}_{conv,dry}''$ are the convection heat flux from wetted and dryout surface, respectively, and k_{dry} is the wall dryout area fraction from the wall dryout area fraction model. The convective heat flux at wet surface can be further expressed as

$$\dot{q}_{conv,wet}'' = (1 - k_{quench}) \cdot \dot{q}_{conv}'', \tag{3.56}$$

where k_{quench} is from Kurul-Podowski bubble influence wall area fraction.
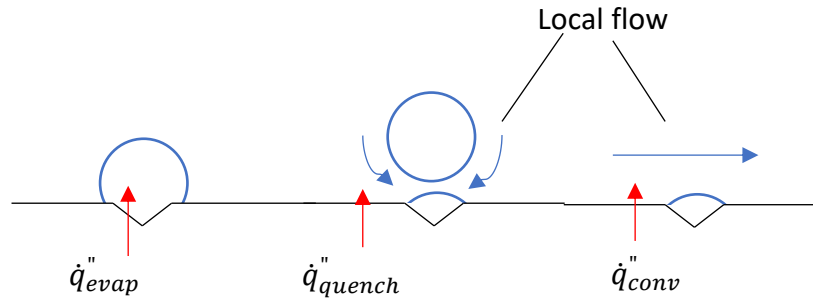
Fig. 31. Graphic of wall boiling model

(3.54) can also be presented as

$$\dot{q}''_w = \dot{q}''_{w,c} + \dot{q}''_{w,cd} + \dot{q}''_{w,d} , \tag{3.57}$$

which specifies the heat flux contribution from continuous and dispersed phase. The three terms on the right-hand side are the wall heat flux from continuous phase, continuous-dispersed phase interface and dispersed phase, respectively. Each above-mentioned term can be written as following:

$$\dot{q}''_{w,c} = (1-k_{dry})\left[\left(1-k_{quench}\right)\dot{q}''_{conv} + \dot{q}''_{quench}\right], \tag{3.58}$$

$$\dot{q}''_{w,cd} = (1-k_{dry})\cdot\dot{q}''_{evap} , \tag{3.59}$$

$$\dot{q}''_{w,d} = k_{dry}\cdot\dot{q}''_{evap} . \tag{3.60}$$

As shown in (3.54) and Fig. 31, the wall heat flux can be determined by evaporation, convection and quenching. To determine the value of these three terms, six sub-models are used under the frame of wall boiling by Star-CCM+ to specify the wall heat flux. Table. 23 summarizes the sub-models that used in this study.

Table. 23. Sub-models and corresponding selection for wall boiling model

	Sub-model	Model
Convective	Wall dryout area fraction	Basic wall dryout area fraction
Evaporation	Nucleation site number density	Lemmert-Chawla
	Bubble departure diameter	Tolubinsky-Kostanchuk
	Bubble departure frequency	Cole
Quenching	Quenching heat transfer coefficient	Del Valle-Kenning
	Bubble influence wall area fraction	Kurul-Podowski

Star-CCM+ uses

$$\dot{q}''_{conv,wet} = \frac{\rho_c C_{p,c} u^*_c}{T_c^+}(T_w - T_c) ,$$ (3.61)

and

$$\dot{q}''_{conv,dry} = \frac{\rho_d C_{p,d} u^*_d}{T_d^+}(T_w - T_d) ,$$ (3.62)

to calculate the convective heat flux for wetted and dryout surface, respectively. u* is the reference velocity near the heating surface from (3.31) and T^+ is the non-dimensional temperature depends on the distance from the heating surface. Both parameters are non-dimensional and decided by non-dimensional wall distance (y^+). The Basic wall dryout area fraction model,

$$k_{dry} = \begin{cases} 0 & \alpha_\delta \le \alpha_{dry} \\ f(\beta) & \alpha_\delta > \alpha_{dry} \end{cases} ,$$ (3.63)

provides a wall dryout fraction which is used to decide the convective heat flux is including dispersed phase contribution or not. If the vapor volume fraction averaged over the bubbly layer thickness (α_δ) is less than the wall dryout break point (α_{dry}), the influence from the dispersed phase is not considered. On the other hand, k_{dry} is decided by

$$f(\beta) = \beta^2(3-2\beta), \ \beta = \frac{\alpha_\delta - \alpha_{dry}}{1 - \alpha_{dry}} ,$$ (3.64)

if the contribution from the dispersed phase is included. The default setting for α_{dry} that adopted by Star-CCM+ is derived by (Weisman &Pei, 1983) with the value of 0.82.

The evaporative heat flux can be written as

$$\dot{q}''_{evap} = n'' f_d (\frac{\pi d_w^3}{6}) \rho_d h_{fg} ,$$ (3.65)

where n'' is nucleation site number density, d_w is bubble departure diameter and f_d is bubble departure frequency. The evaporation wall heat flux is graphically depicting in Fig. 32. Two sets of models for evaporation heat flux are provided by Star-CCM+ as shown in Table. 24. Though Hibiki-Ishii's method (Hibiki &Ishii, 2003) gives a more precise prediction under a wide range of pressure for nucleation site number density, it is found

out that the complication of the correlation leads to an unrecoverable instability for the simulation. Thus, in this study, the default setting of Lemmert-Chawla's method (Lemmert &Chawla, 1977) is used for nucleation site number density prediction.

$d_w = bubble\ diameter$

$f_d = time$

$n^{"} = 2\ sites\ /\ area$
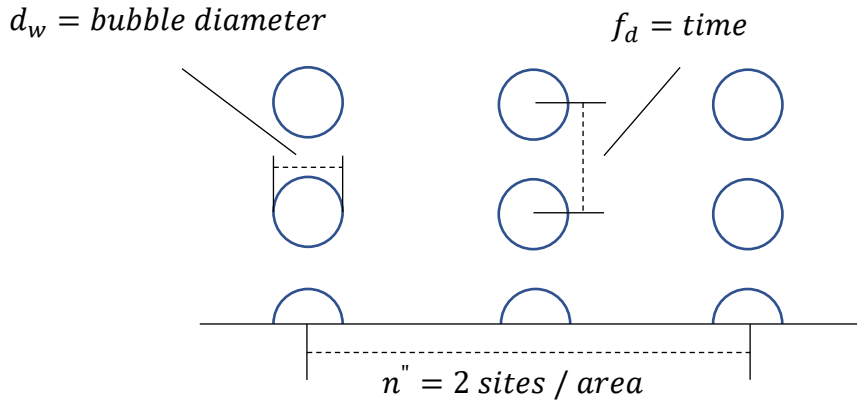
Fig. 32. Sketch of model used for evaporation heat flux

Table. 24. Options of evaporation heat flux model in Star-CCM+

	Nucleation site number density	Bubble departure diameter	Bubble departure frequency
Set 1	Hibiki-Ishii	Kocamustafaogullari	Cole
Set 2	Lemmert-Chawla	Tolubinsky-Kostanchuk	

Lemmert-Chawla's nucleation site number density can be written as

$$n'' = (185\Delta T_{\text{sup}})^{1.805},\tag{3.66}$$

where ΔT_{sup} is the wall superheat which can be further decided by

$$\Delta T_{\text{sup}} = \min(\max(T_w - T_{sat}, 0), \Delta T_{\text{max}}),\tag{3.67}$$

where ΔT_{max} is the maximum wall superheat applied for Lemmert-Chawla's method. It should be noticed that Tolubinsky-Kostanchuk's bubble departure diameter correlation (Tolubinsky &Kostanchuk, 1970) is designed and developed for the Lemmert-Chawla nucleation site number density model only. Thus, they are both adopted in this study. Tolubinsky-Kostanchuk's bubble departure diameter can be expressed as

$$d_w = d_0 \exp(-\frac{T_{sat} - T_c}{\Delta T_0}),\tag{3.68}$$

where d_0 is reference bubble departure diameter which has a value of 0.6 *mm* and ΔT_0 is the corresponding subcooling. For the bubble departure frequency model, Star-CCM+ takes Cole's method as a standard. The detailed of the model can be found in (Cole &R., 1960) and shown as

$$f = \left[\frac{4}{3} \frac{g(\rho_c - \rho_d)}{d_w \rho_c} \right]^{0.5} .$$

(3.69)

When the bubbles detach from the heated surface, the continuous phase replaces the dispersed phase on the heated surface. The induced quenching is calculated by the quenching wall heat flux which is written as

$$\dot{q}''_{quench} = h_{quench}(T_w - T_c),$$

(3.70)

where h_{quench} is quenching heat transfer coefficient that decided by Del Valle-Kenning method (DelValle &Kenning, 1985) as

$$h_{quench} = 2 k_{quench} f (\frac{\rho_c C_{p,c} k_c t_w}{\pi})^{0.5} .$$

(3.71)

k_c is thermal conductivity inside continuous phase and t_w is the waiting time which equals 80 percent of bubble departure cycle. The bubble influence wall area fraction, k_{quench}, can be further expressed as

$$k_{quench} = 2 \frac{\pi d_w^2}{4} n'',$$

(3.72)

by the using of Kurul-Podowski's method (Kurul &Podowski, 1990).

3.6.4   *Rohsenow Boiling Model in VOF*

Two boiling models are available under the frame of VOF two-phase model. Transition boiling model simulates boiling process by user defining boiling curve, thus, is not considered in this study. On the other hand, Rohsenow boiling model reproduces boiling pattern by using of Rohsnow's nucleate boiling correlation (Rohsenow, 1951) and film boiling model. Under the frame of VOF model, appropriate heat transfer model should be selected for boiling models. Star-CCM+ provides three different heat transfer models which should be applied with different simulating purpose as shown in Table. 25.

Table. 25. Heat transfer models available under the scope of VOF model

Model	Description	Usage
Segregated fluid enthalpy	• Solve total energy equation with chemical thermal enthalpy. • Temperature is decided by enthalpy.	Simulations that involving combustion.
Segregated fluid temperature	• Solve total energy equation with temperature. • Enthalpy is decided by temperature.	Simulations not involving combustion.
Segregated fluid isothermal	Relatively constant temperature.	For the purpose of saving computational cost.

The Rohsenow boiling model can be split into two parts which are the nucleate boiling model and the film boiling model. The nucleate boiling model simulates surface heat flux by

$$q''_{Roh} = \mu_l h_{fg} \left(\frac{g\left(\rho_l - \rho_v\right)}{\sigma} \right)^{0.5} \left(\frac{C_{pl}\left(T_l - T_{sat}\right)}{C_{qw} h_{fg} Pr_l^{np}} \right)^{3.03} , \tag{3.73}$$

where μ_l is the liquid viscosity, C_{pl}, C_{qw}, np are empirical coefficients, T_l is the liquid temperature, T_{sat} is the saturated temperature of the water and Pr is the Prandtl number. The vapor generating mass rate on the heater surface can be calculated by the surface heat flux as

$$\dot{m}_{ew} = \frac{C_{ew} q''_{Roh}}{h_{fg}}, \tag{3.74}$$

where q''_{Roh} is boiling surface heat flux for Rohsenow boiling model and C_{ew} is the ratio of surface heat flux using for vapor generating. One of the significant defects of Rohsenow's correlation is that if the correlation is applied outside its applicable range, for example, film boiling, an unrealistic high heat flux may introduce on the surface. To prevent the scenario, a correction is added as a multiplication to the heat flux as

$$\max\left[0, \min\left(\left(\frac{T_w - T}{T_w - T_{sat}} \right), 1 \right) \right]. \tag{3.75}$$

Under the condition of high vapor volume fraction, the secondary phase can't be resolved in a single grid. That is, the vapor occupies more than one cell. In this case, Rohsenow's

nucleate boiling correlation is no longer suitable to determine the surface heat flux. The film boiling model provides an alternative solution that considers only heat transfer with secondary phase. The transition equation as

$$f(\alpha_{sec}) = 1 - \min(1, \alpha_{sec} / \alpha_{film})^8 ,$$ (3.76)

determines the ratio of surface heat flux that used for nucleate boiling, and the rest part of surface heat flux is considered only for the vapor heat transfer. Within the equation, α_{film} decides at which vapor volume fraction that the heat transfer model is switched from nucleate boiling model to film boiling model. When the film boiling model is triggered, the heat transfer on the surface considers only heat flux between heater surface and secondary phase. Except the boiling takes place on the heated surface, the boiling happens in the water bulk or thermal diffusion (condensation and evaporation) is included by

$$\dot{m}_{ec} = \frac{HTC \times Area(T - T_{sat})}{h_{fg}} ,$$ (3.77).

where $\dot{m}_{ec}$ is the mass transfer between primary and secondary phase and $HTC \times Area$ is an empirical constant that decided by heat transfer coefficient and interaction area.

Totally, there are six parameters, summarized in Table. 26, that can be modified when Rohsenow boiling models is activated.

Table. 26. Six parameters in Rohsenow boiling model

Parameter	Description	Default
C_{qw}	Empirical coefficient varied with liquid-solid surface.	0.008
C_{ew}	The ration of heat flux using for generating bubbles.	0.1
$HTC \times Area$	Heat transfer coefficient between two phases multiplied by interaction area.	5E6
α_{film}	The vapor volume fraction that indicates the switching of nucleate boiling to film boiling.	0.75
np	The exponent of Prandtl number.	1.73
Sc_t	The turbulent Schmidt number that is associated with the turbulent diffusion of vapor bubbles.	0.9

The default setting for these parameters is developing with the experimental application which considers heating up upward flow with heat source applied on the circular pipe wall. Although the boundary conditions are slightly different from the application of TRTL

facility and geometry that applied by this study, it is found out to be the most similar application that can be found in the reference. In addition, (Jabardo, Silva, Ribatski, &Barros, 2004) has summarized all the parameters that can be modified in (3.73) based on the experimental application.

3.7   Convergence and Stability

To prevent the diverged scenario, several methods are taken into account in this study for the purpose of stability maintenance. This section summaries all the treatment from general manner (software level) to a detail manner (model properties and solver level). All the following setting are discussed and developed under the construction from the support of CD-Adapco.

3.7.1   Double Precision Version

Star-CCM+ provides two software versions, mixed precision version and double precision version, according to the floating point of computation. While a single precision float uses 4 bytes of memory to preserve 7 digits of precision, a double precision float uses 8 bytes of memory to preserve 15 digits of precision. A mixed version adopts double precision float with the parameter of coordinates, pressure and displacement. However, in double precision version, a double precision float is adopted for all the calculation within the simulation. Due to the increasing of the accuracy, double precision float prevents the error accumulated from the round-off. The robustness of the simulation thus highly improved. It should be noticed that, as a drawback of the improvement of accuracy, the memory requirement and the total solver elapsed time are increased by about 20 percent compared to the mixed precision version. Due the complicated and trivial physical phenomena within the multiphase flow, a double precision version should always be considered when multiphase simulations are studied.

3.7.2   Prism Layer Thickness and Wall Treatment

The k-ε turbulent model is one of the two-equation RANS model using wall y^+ method to resolve turbulent flow. Wall y^+ is a non-dimensional parameter that calculated from the thickness of the first cell on the surface. RKE-2L, the turbulent model adopted in this study,

uses all-y^+ method to resolve the turbulence on the boundary. Under the frame of all-y^+ method, the wall y^+ value between thirty and five hundred would provide the most stable simulating process. This means an over refinement of the prism layer cell on the surface may lead stability issues to the simulation. To prevent the divergence of solution, the wall y^+ values in this study are ensured between the range for all the cases that included in grid independent study. Fig. 33 shows the wall y^+ value for the simulation with the most refined mesh (wall thickness of 0.3 *mm*) and Table. 27 summarizes the averaged value of wall y^+ value for all the precursor simulations with different grid size.
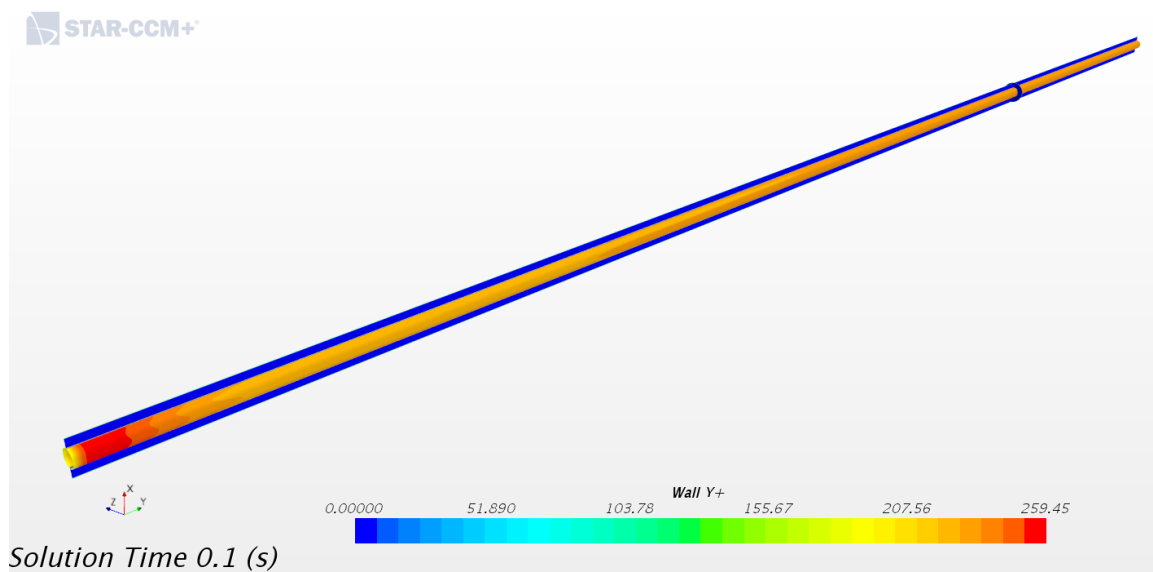
Fig. 33. Wall y^+ value with wall thickness of 0.3 *mm*

Table. 27. Wall y^+ values for all prism layer thicknesses

Prism layer thickness	Surface averaged Wall y^+
0.03 *mm*	2.2883E2
0.04 *mm*	3.0318E2
0.05 *mm*	3.8081E2
0.75 *mm*	5.5113E2
1.0 *mm*	8.9756E2

3.7.3   Time Step

The size of temporal grid does a significant influence on the accuracy and converged ability. With the changing boundary condition (heat input as a function of time) along the

simulating physical timeline, it is desirable to have a time step as small as possible. In this case, the changing of the heat input within each time step can be reduced and cause a more stable simulation. However, with the drawback of extremely expensive computational cost, it is impossible to have an infinitely small temporal grid. Thus, the time step is decided by the temporal resolution. Even the significant increasing of computation may be the concern for stability, the convergence still benefit since the physical phenomenon within each time step has been resolved and detailed. A non-dimensional parameter of convective courant number (CFL) can be used as a rule of thumb to decide the size of temporal grid size which can be expressed as

$$\text{CCN} = \frac{v_s \times \Delta t}{\Delta x} = \frac{4\left[\frac{m}{s}\right] \times 0.0001[s]}{0.05 \times 0.01 \times 2.54[m]} = 0.315, \tag{3.78}$$

where v_s is the velocity along the stream line, Δt is temporal grid size and Δx is spatial grid size. To resolve the flow phenomenon, it is necessary to introduce a CFL less than 1. The physical means behind is that the flow is not passing through more than one cell in each time step. If CFL is bigger than 1, the information between cells may lost and, thus, have a negative impact to the stability of the simulation. (3.78) provides a good value of CFL by using 1E-4 second as a time step. It should be noticed that (3.78) is only applied for two-dimensional geometry, however, due the simplicity of the geometry in this study, the true value of CFL in three-dimensional geometry is not far away from the result. The detailed value can be reviewed directly from Star-CCM+ built-in field function as summary in Table. 28. Fig. 34provides an example of CFL with wall thickness of 0.3 *mm*.

Table. 28. CFL values for all prism layer thicknesses

Wall thickness	Volume averaged CFL
0.03 *mm*	3.7080E-1
0.04 *mm*	3.7244E-1
0.05 *mm*	3.6895E-1
0.75 *mm*	3.8614E-1
1.0 *mm*	3.7597E-1
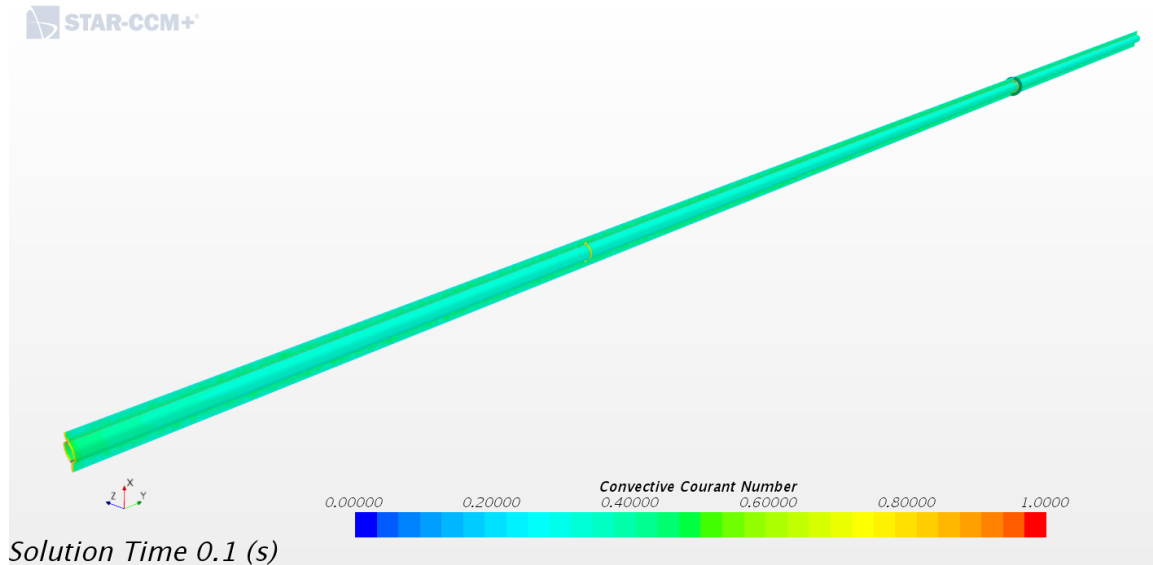
Fig. 34. CFL value with prism layer thickness of 0.3 mm

3.7.4   Boundary Conditions

Before each experimental application, the inlet temperature of the test section within TRTL facility is heated up to the level near the saturated temperature. In other words, the temperature subcooling is maintaining about 5 $°K$ by the preheater before each test. To respond to the influence of liquid subcooling as applied in the application, the inlet temperature for all the simulations are set up by 330 $°C$ (the saturated temperature at 2000 *psi* is 335.48 $°C$). However, due to the fact that EMP model treats dispersed phase as an independent phase, the vapor volume fraction is not allowed to be zero. A setting of zero may lead to an extremely low converged value with less than the order of negative twenty and cause a challenge of stability maintenance. Thus, a low value, 1.0E-4, is set up as an alternative inlet vapor volume fraction.

To deal with the compressible flow (changing density), the pressure type outlet is set up for outlet boundary of simulating domain. However, back flow is a drawback of pressure type outlet which is also known as one of the most common reason that may cause the divergence. To solve back flow, the vapor volume fraction on the outlet boundary is extrapolated from the fluid region. Since vapor volume fraction is extrapolated from test section, the possibility of back flow can highly reduce and thus improve the stability.

3.7.5   Wall Boiling Model Selection

Recall that the wall boiling model can be broken down to six sub-models. Star-CCM+ provides two model sets for nucleation site number density and bubble departure diameter model. Though Hibiki-Ishii's nucleation density number density model has a wider range of applicability and more accurate under certain condition, it is found out to be more unstable, especially when the boiling introduced with high heat flux. This is possibly because Hibiki-Ishii's nucleate site number density correlation is a function of wall contact angle, cavity length, cavity radius, pressure and wall superheat while Lemmert-Chawla's method considers pressure and wall superheat only. It is proved that, in this study, Hibiki-Ishii's model cause a hard time for simulations to get converged results. Such divergence cannot be fixed even with all the efforts mentioned in this section. As a result, Lemmert-Chawla's model and its corresponding bubble departure diameter model, Tolubinsky-Kostanchuk's method, are set up for the wall boiling model under the consideration of stability.

3.7.6   Turbulent Model Properties

Since this study focus on transient heat transfer, the validation of different turbulent models is not considered. Nevertheless, due to the fact that k-ε turbulent models are industry standards and provides an accuracy prediction for turbulent behavior under the frame of internal flow, several k-ε turbulent models has been tested to help the convergence. It is found out that RKE-2L model, as a recommendation from Star-CCM+ user guide, provides the most stable solution for wall y^+ value between 30 and 500. It should be noticed that the setting for the RKE-2L model is modified with the instruction from CD-Adapco support. The purpose of the modification is to help turbulent flow profile developed earlier before entering the test section. Recall that vapor volume fraction is modified to help the convergence of EMP model. It is found out that, however, the modification does a negative impact for the convergence of nucleation site number density model. In Fig. 35, it is apparent that the highest value of turbulent viscosity is located on the front surface of heated section when modification is not applied. This may indicate that the velocity profile is not developed until the flow reaches the heated section. With this issue, most of the simulations diverged earlier after the incipience of boiling. To prevent such scenario,

turbulent intensity and turbulent viscosity ratio are modified from the defaulting setting and results to the value shown in Fig. 36. The modifications and corresponding default values are summarized in Table. 29.
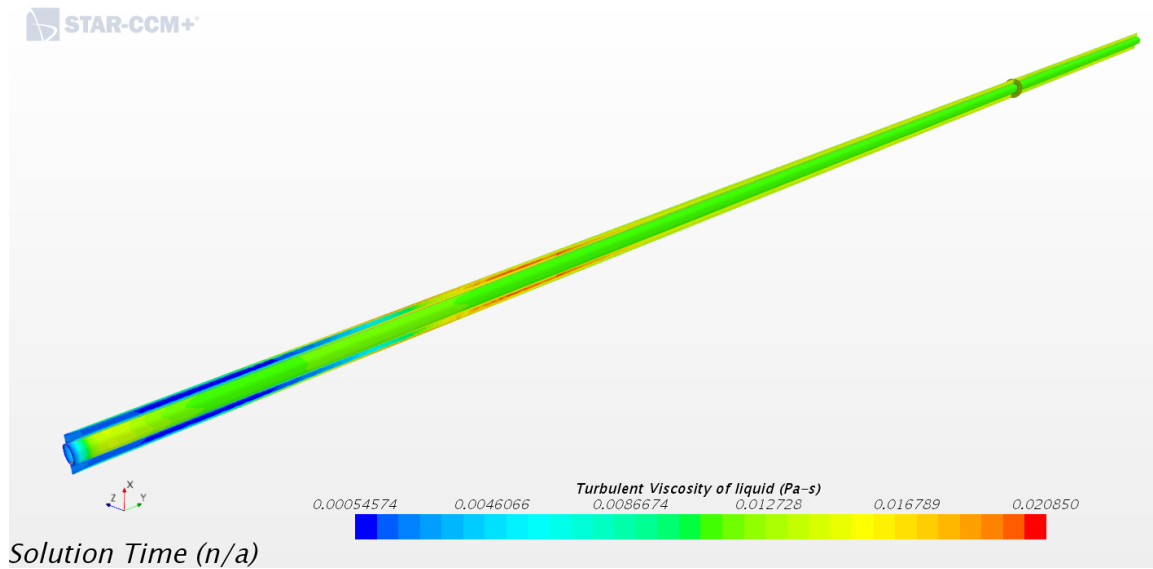
Fig. 35. Turbulent viscosity of liquid for non-modified boundary condition
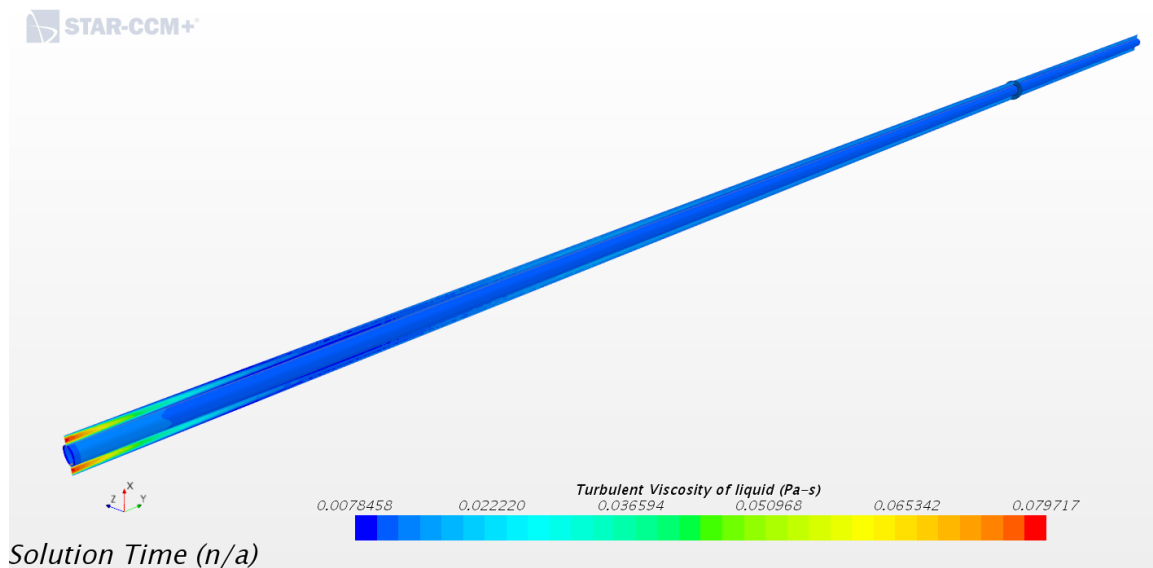
Fig. 36. Turbulent viscosity of liquid for modified boundary condition

Table. 29. Modified turbulent properties

Phase	Property	Modification	Default value
Continuous phase	Turbulent intensity	0.05	0.01
	Turbulent viscosity ratio	400	10
Dispersed phase	Turbulent intensity	0.05	0.01
	Turbulent viscosity ratio	200	10

3.7.7   Under Relaxation Factor and Inner Iteration

Under Relaxation Factor (URF) is a powerful tool which balance the solver algorithm between converged speed and stability. The solution form of the iterating algorithm can be expressed as

$$a_{cc}\phi_{cc}^{k+1} + \sum_{nc} a_{nc}\phi_{nc}^{k+1} = a_{cc}\phi_{cc}^{k} + \sum_{nc} a_{nc}\phi_{nc}^{k} + r, \tag{3.79}$$

where *cc* is the current cell, *nc* is the neighboring cell of *cc*, *r* is the residual (solution difference) between current iteration ($k+1$) and previous iteration (k), ϕ is the solution from transport equations, and a_{cc} and a_{nc} are the coefficients from the discretized term. In Star-CCM+, (3.79) is applied with an additional term, URF (ω), and can be expressed as

$$a_{cc}\phi_{cc}^{k+1} + \omega\sum_{nc} a_{nc}\phi_{nc}^{k+1} = a_{cc}\phi_{cc}^{k} + \omega\sum_{nc} a_{nc}\phi_{nc}^{k} + \omega r \tag{3.80}$$

where ω is URF with value between zero and one. The purpose of URF is to decide the ratio of residual that used for blend with the solution form previous iteration to form the solution for current iteration. Theoretically, it is expected that the lower the URF, the more inner iterations are needed to reach a converged status of residual equals to 0. Namely, the stability is highly increased by reducing the changing between each iteration with the drawback of significant increasing of necessary number of inner iterations. The default settings for URF perform a good balance between converged speed and stability. Typically, the number of inner iterations required for default setting URF is about 15 to 30. However, it is extremely aggressive processing a simulation, which includes dramatical changes of boundary condition in each time step, with a default value of URF. With a concern of stability, the URF for different solvers and models are modified as Table. 30, and an extremely high number of inner iterations of 500 is adopted for the simulations to reach converged status in each time step.

Table. 30. Solvers and corresponding URF

Solver	Default URF	Modified URF
Phase coupled velocity	0.7	0.1
Pressure	0.3	0.1
Volume fraction	0.5	0.1
Fluid segregated energy	0.9	0.1
Solid segregated energy	0.99	0.1
k-ε turbulence	0.8	0.1
k-ε turbulent viscosity	1.0	0.1
Boiling mass transfer rate	0.5	0.1
Wall boiling	0.5	0.1
Wall dryout area fraction bubbly layer	0.5	0.1

3.8   Overview of The Setting

All the models that used in this study are summarized in this chapter, including the models for solid and fluid region. Additionally, the models for EMP and VOF simulations in fluid region are presented herein. Table. 31, Table. 32 and Table. 36 are the general models while Table. 34, Table. 35, and Table. 37 detail the respective sub-models. It should be noticed that, all the simulations in this study are processing with Star-CCM+ version 13 which is the version provided on the HPC (high performance cluster). Due to the computational resource limitation, all the models setting listed in this chapter are set up on the local computer using Star-CCM+ version 12. The catalog for the models may slightly different between Star-CCM+ version 12 and 13.

3.8.1   Modeling Solid Region

Table. 31. Models for solid region

Models	
Space	Three dimensional
Gradient metrics	Gradient
Time	Implicit unsteady
Material	Solid
Equation of state	Constant density
Optional models	
	Segregated solid energy

3.8.2 Modeling Fluid Region with EMP

Table. 32. General models for EMP

Models		Sub-models
Space	Three dimensional	
Gradient metrics	Gradient	
Time	Implicit unsteady	
Material	Eulerian multiphase	Table. 35
Eulerian multiphase model	Multiphase segregated flow	
Viscous regime	Turbulent	
Optional model		Sub-models
	Phase coupled fluid energy	
	Multiphase interaction	Table. 33
	Gravity	

Table. 33. Multiphase interaction models for EMP

Models		Sub-models
Phase interaction topology	Continuous-dispersed phase interaction	
	Drag force	
	Interaction area density	
	Interaction area length	
Optional models		Sub-models
	Lift force	
	Multiphase material	
	Virtual mass force	
	Virtual mass coefficient	
	Turbulent dispersion force	
	Interphase mass transfer	
Interphase mass transfer rate	Boiling mass transfer	
	Wall boiling	Table. 34

Table. 34. Wall boiling models for EMP

Models	
Wall dryout area fraction	Basic wall dryout area fraction
Nucleation site number density	Lemmert-Chawla
Bubble departure diameter	Tolubinsky-Kostanchuk
Bubble departure frequency	Cole
Quenching heat transfer coefficient	Del Valle-Kenning
Bubble influence wall area fraction	Kurul-Podwoski

Table. 35. Eulerian multiphase material models for EMP

Models	
Material	Liquid/Gas
Equation of state	IAPWS-IF97
Energy	Segregated fluid temperature
Turbulence	RANS
RANS	k-ε turbulence
k-ε turbulence models	Realizable k-ε two-layer
Wall treatment	Two-layer all y^+ wall treatment
Optional models	
	Exact wall distance

3.8.3   *Modeling Fluid Region with VOF*

Table. 36. General models for VOF

Models		Sub-models
Space	Three dimensional	
Gradient metrics	Gradient	
Time	Implicit unsteady	
Material	Eulerian multiphase	Table. 37
Eulerian multiphase model	VOF	
Flow	Segregated flow	
Viscous regime	Turbulent	
Turbulence	RANS	
RANS	k-ε turbulence	
k-ε turbulence models	Realizable k-ε two-layer	
Wall treatment	Two-layer all-y^+ wall treatment	
Optional model		Sub-models
	Gravity	
	Multiphase interaction	
	Segregated fluid temperature	

Table. 37. Eulerian Multiphase material models for VOF

Models	
Material	Liquid/Gas
Equation of state	IAPWS-IF97
Optional model	
	Exact wall distance

4   RESULTS AND DISCUSSION

4.1   Initial Condition

With the stability concern, all the transient simulations in this study are developed after the precursor simulations. Served as initial conditions, the steady state model is adopted as the time model for all the precursor simulations. That is, the time influence is not considered in these precursor simulations and have no impact to following transient heat transfer behavior. The purpose of the precursor simulation is to provide not only a reasonable heat distribution among all the heated surface but also provides a fully developed flow profile before the transient power output is applied. In order to acquire sufficient convergence, all the precursor simulations are postponed manually after a lower plateau is confirmed in the residual. Table. 38 provides necessary number of iterations for all the precursor simulations and an overview of grid independent study simulations against different wall thickness for both EMP and VOF model.

Table. 38. Precursor simulation and grid independent study for EMP and VOF

	Wall thickness	Precursor simulation (Total heat source/ Number of inner iteration)	Grid independent study (Total heat source/ Physical time)
EMP	0.3 mm	2.4 kW / 34000	Diverged
	0.4 mm	2.4 kW / 20000	10 kW / 0.1 s
	0.5 mm	2.4 kW / 20000	10 kW / 0.1 s
	0.75 mm	2.4 kW / 22000	10 kW / 0.1 s
	1.0 mm	2.4 kW / 22000	10 kW / 0.1 s
VOF	0.3 mm	2.4 kW / 10000	10 kW / 0.1 s
	0.4 mm	2.4 kW / 10000	10 kW / 0.1 s
	0.5 mm	2.4 kW / 10000	10 kW / 0.1 s
	1.0 mm	2.4 kW / 10000	10 kW / 0.1 s

4.1.1   Inner Iterations

The maximum number of iterations is a most common stopping criteria that used for steady state simulation, however, the problem stands for how to determine an appropriate number for the iterations. In this study, the residual from each precursor simulation is adopted as an important standard for determining the maximum number of iterations. As (3.79), for

steady state simulation, the residual indicates the difference between each iteration. Theoretically, the residual is equal to zero if a true solution is acquired, however, this is not realistic since it is impossible and resource-wasting to achieve a solution with no changing of the residual. As a result, all the precursor simulations are only processing until the residuals reach a lower plateau. Fig. 37 shows the residuals from an EMP precursor simulation with wall thickness of 0.4 *mm*.
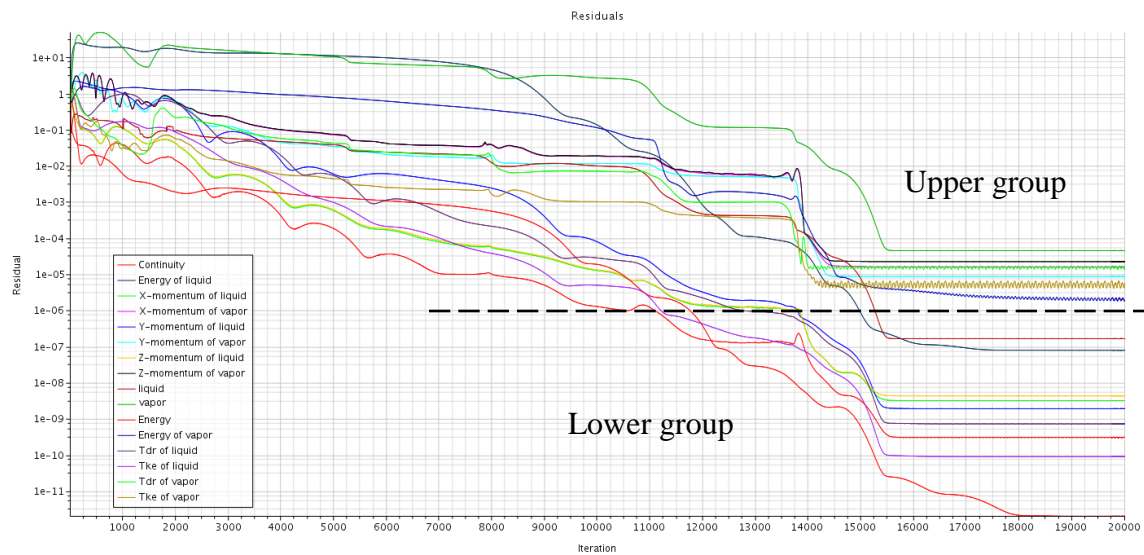
Fig. 37. Normalized residuals of precursor simulation: wall thickness of 0.4 *mm*

It is clearly shown in shown in Fig. 37 that the all the residuals are decreasing gradually before the iteration of 14000. However, after 14000 iteration, the residuals drop suddenly and reach a lower plateau at about 16000 iteration. At this point, the precursor simulation can be considered as converging. To guarantee the stability for the following transient case, the precursor simulation is further processing until all the residuals converge to a stable value. In this case, all the residuals maintain constant value after the iteration of 18000, thus, the precursor simulation is decided to stop at iteration of 20000.

Even though all the residuals reach a lower plateau, the problem here stands for what is the actual value. A rule of thumb that deciding the convergence for CFD study is the value of 1E-6. It should be noticed that the residuals provide in Fig. 37 is a normalized residual which means the value is normalized by the value form the first several iterations. The

normalized residuals provide a stricter standard for determining the convergence compared to non-normalized residual. In this study, even the simulation is developed with a double precision version, the highest normalized residual (mass balance of vapor) in Fig. 37 remains in a relative higher level which is 1E-5. On the other hand, Fig. 38 shows the non-normalized value of residuals. It is clearly that all the value in Fig. 38 are giving an extremely low value with the highest value (energy of liquid) about 1E-9.
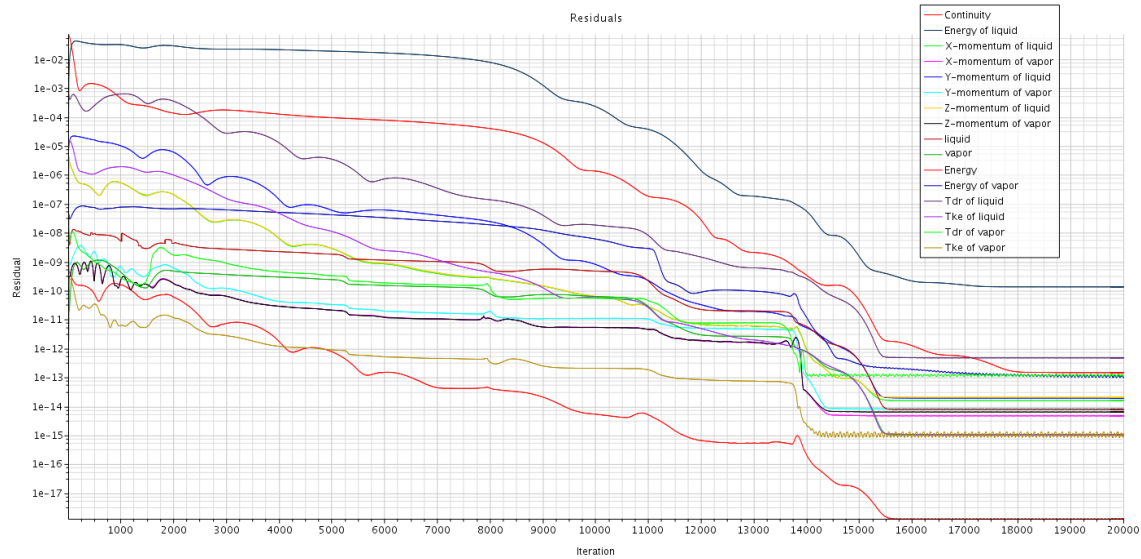
Fig. 38. Non-normalized residuals of precursor simulation: wall thickness of 0.4 *mm*

Furthermore, as shown in Fig. 37, the residuals can be obviously split into two groups by the above-mentioned standard of 1E-6. The upper group has a relatively higher value for residuals which means these solvers face a more challenging scenario to reach a converged status. Typically, these solvers are associated with dispersed phase which includes mass, momentum and energy solver. Meanwhile, the lower group includes those solvers associated with the continuous phase. As a brief conclusion, it is expected that, for the following transient simulations, the computation in dispersed phase may cause stability issue. During the grid independent studies, it is proved that the computation in dispersed phase does have a significant influence on the stability even though the total heat source (10 *kW*) is far away lower than CHF. Recall the discussion for the stability maintenance, most of the transient simulations diverged at the early stage of incipient boiling if the inlet boundary condition and turbulent model for dispersed phase are not setting appropriately.

4.1.2   Impact of Grid Size

Studies in the past indicated that the mesh size on the heated surface plays a crucial role in the stability. Table. 38 has listed the necessary number of iterations for simulations to reach the converged status. In VOF model, it is found out that the additional iterations are not needed though the mesh size is refined. In other words, there isn't a most appropriate mesh size for the VOF model in this study. In the contrast, the necessary number of iterations is changing depends on the mesh size for EMP type simulations. Fig. 39 and Fig. 40 provide the residuals for precursor simulation with wall thickness of 0.75 *mm* and 0.3 *mm*, respectively.
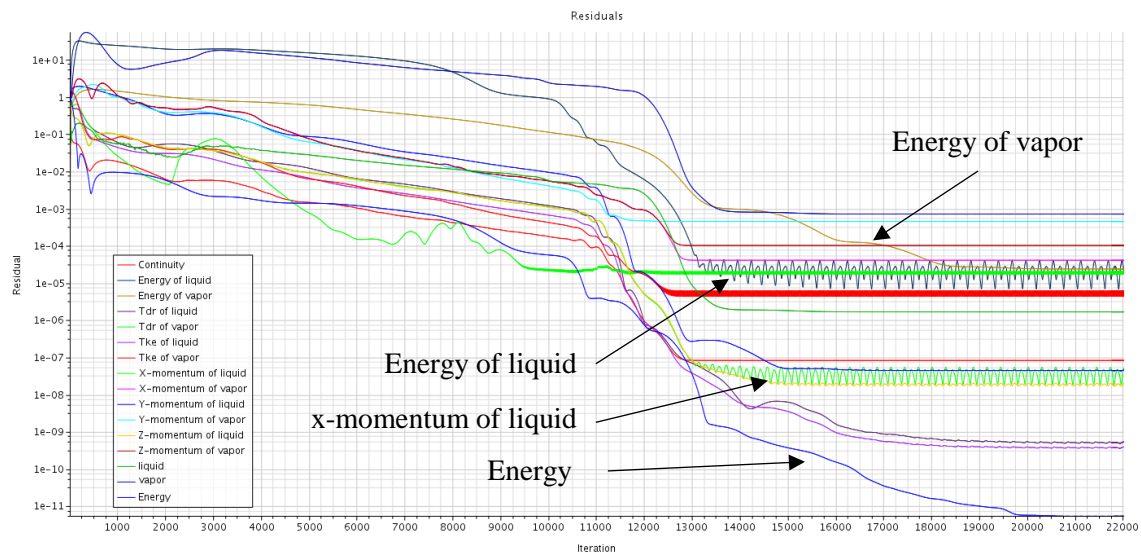
Fig. 39. Residuals of precursor simulation: prism layer thickness of 0.75 *mm*

In the case with 0.75 *mm* wall thickness, it is found out that an additional 2000 iterations are needed for the precursor simulation to reach the converged status. As shown in Fig. 39, even though most of the residuals start decreasing around 12000 iteration, it takes way longer than the case with wall thickness of 0.4 *mm* to reach the lower plateau. With same characteristic, the solvers for dispersed phase is difficult to converge, especially for the energy solver. The energy solver for the dispersed phase reaches the lower plateau at about the iteration of 19000 which leads to the total energy solver converged more than 20000 iterations. It should be noticed that the residuals for continuous phase, including the radial

momentum (x and y-axis) and energy solver, oscillate hardly even when the lower plateaus are reached. Moreover, several solvers converge to a high value of more than 1E-3 which possibly indicates that the mesh size is not small enough to resolve the turbulent behavior near the viscous surface. As discussion for the stability, the wall y^+ value should in the range of 30 and 500 in order to provide best resolution for turbulent behavior under the frame of RKE-2L turbulent model. It is obvious that the averaged wall y^+ value in the case with 0.75 *mm* wall thickness is slightly higher than 500 and, thus, leads to a challenge for convergence due to the inappropriate application of wall y^+ method.
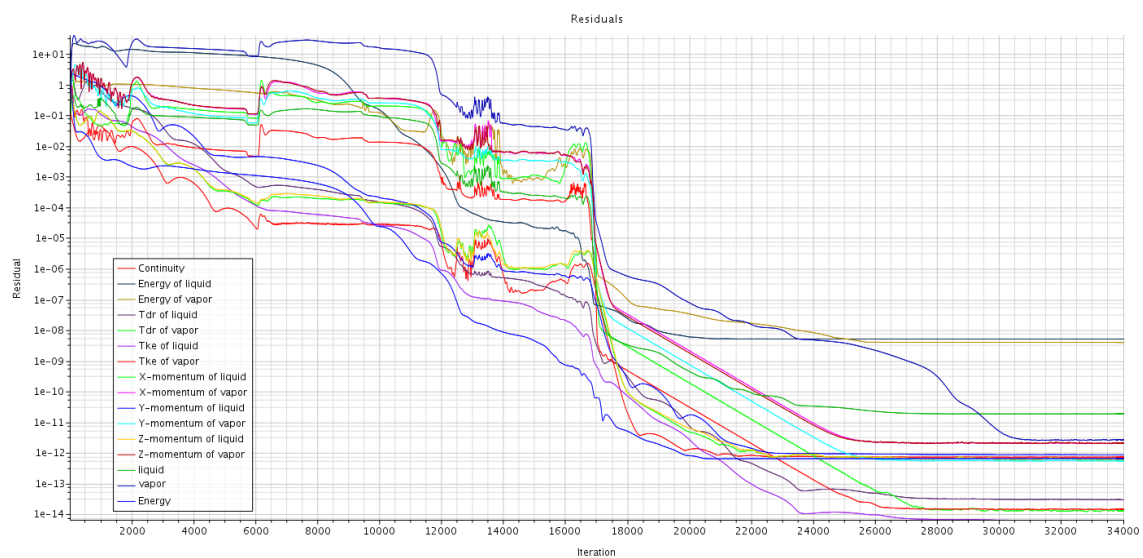
Fig. 40. Residuals of precursor simulation: prism layer thickness of 0.3 *mm*

In the case with 0.3 *mm* wall thickness, the converged ability becomes even worse than those case with low resolution of turbulent behavior. As shown in Fig. 40, to reach the lower plateaus for all the solvers, a total iteration of more than 30000 is necessary. Even though the residuals start decreasing around 17000 iteration, the necessary iterations is 3000 more than the 0.4 *mm* wall thickness case. The possible reasons may be following:

- The mesh size is close to the reference bubble departure diameter which is from the evaporation wall boiling model.
- The mesh number is significantly increased because of the mesh refined method.

Recall the discussion for the mesh refinement, an over refinement may lead to the significant stability issues. Such fact is led by the surface mesh size is smaller than bubble departure diameter. If the surface mesh size is smaller than the bubble departure diameter, the vapor "particle" is very likely to be occupied more than two cells and leads to an extremely difficult scenario for the interphase momentum transfer models to process. The default setting for the Tolubinsky-Kostanchuk bubble departure diameter model adopts 6E-4 *m* as the reference bubble departure diameter which means the surface mesh thickness is smaller or equals to the radius of the vapor "particle". Thus, the scenario mentioned above is very likely to be occurred. Furthermore, one significant step for the mesh refinement in this study is to keep a reasonable stretch factor between prism layer cells and core cells. Thus, an additional layer of prism cells is added in the case with 0.3 *mm* wall thickness compared to the case with 0.4 *mm* and 0.5 *mm* wall thickness. Such additional layer of cell leads to a significant increasing of the cell number along the geometry and may cause an additional loading for the computation and stability. With these factors, it is expected that the number of iterations needed for convergence in the 0.3 *mm* case is highly increased.

4.1.3   Data Series

The precursor simulations result to temperature subcooling of about 1 °*K* on the heated surface by setting up a 2.4 *kW* total heat source for the heat input. The purpose is not only to maintain the stability for following transient simulations but also performs the same initial conditions as the experimental application occurred in TRTL facility. During the precursor simulations, it is found out that the mesh size has almost no impact to the result if the precursor simulations reach a converged status. Fig. 41 shows the boundary heat flux of the heater for different Eulerian multiphase models and each mesh size. The differences between EMP model and VOF model are less than 1E-3 percent for all the mesh sizes. Even though the result provides a discretization error for different mesh size, the difference is less than 10 W/m^2 between the coarsest and the finest mesh set, with the magnitude of 10E+5 for the resulting value.
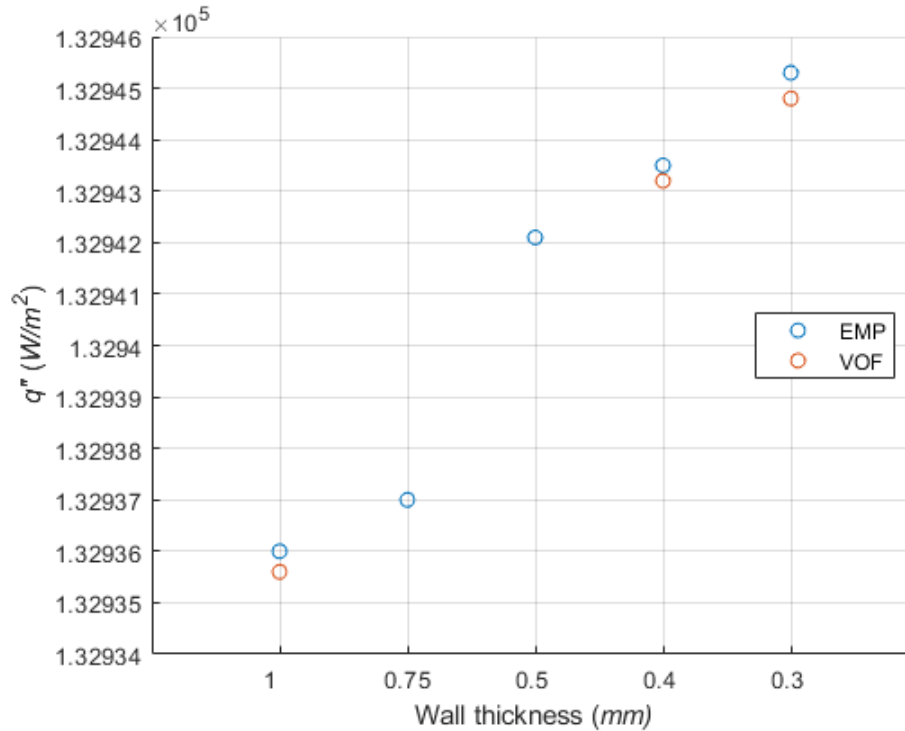
Fig. 41. Precursor simulation: boundary heat flux of heater

Fig. 42 shows the surface averaged temperature of the heater for different Eulerian multiphase models and each mesh size. As same trend from boundary heat flux, the error between the EMP model and the VOF model are less than 1E-3 percent for all cases. The maximum temperature difference for the EMP and VOF model are 0.4877 °K and 0.2414 °K, respectively. In the cases with wall thickness of 1.0 mm and 0.3 mm, the results almost agree with each other and the differences are less than 0.01 °K. It should be noticed that in the case with 0.75 mm wall thickness, the EMP model provides a value of 607.9139 °K which is out of the trend of other results. This may indicate the results from the EMP model is oscillatory converged instead of monotonic converged. Fig. 43 provides the results for the wall super heat on the heated surface. In this study, the wall superheat is calculated using

$$\Delta T_{sup} = T_{wall,avg} - T_{sat} \tag{4.1}$$

The T_{sat} in the equation represents the saturated temperature under the pressure of 2000 psi which is 608.63 °K.
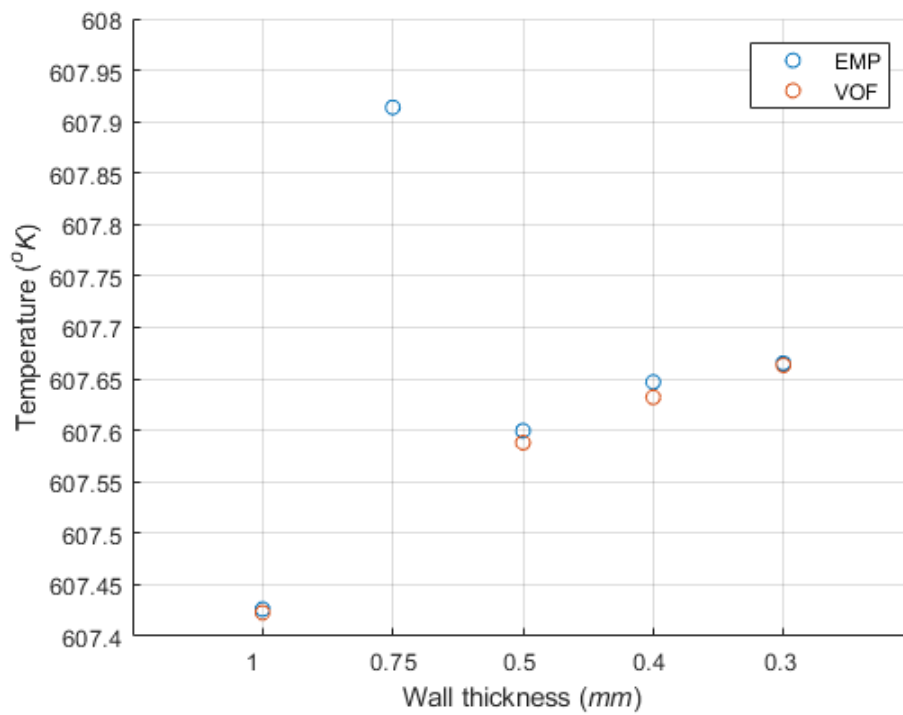
Fig. 42. Precursor simulation: surface averaged temperature of the heater
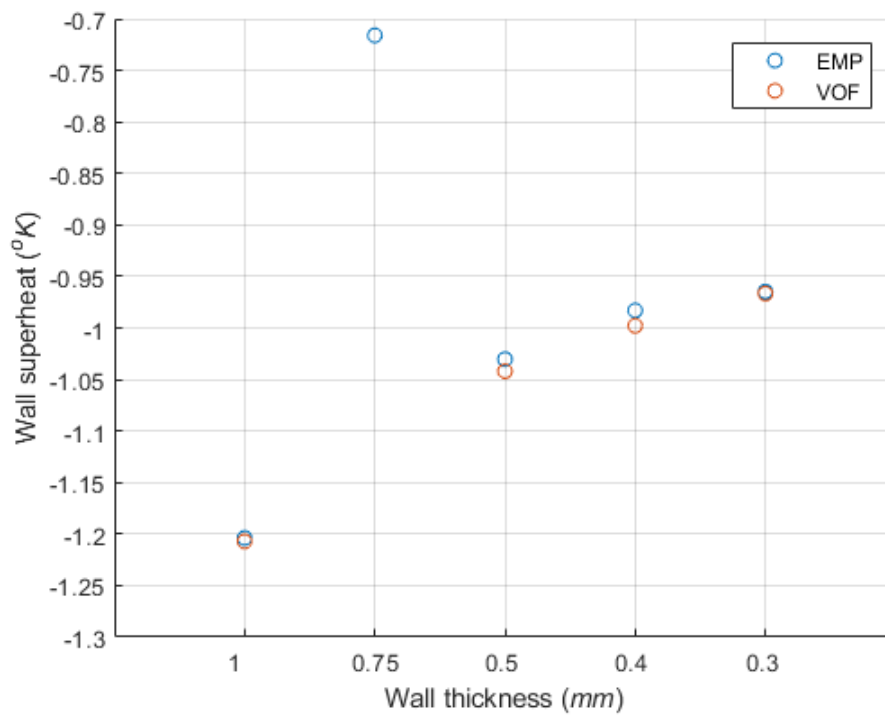
Fig. 43. Precursor simulation: wall superheat of the heater

Fig. 44 and Fig. 45 shows the volume averaged temperature of the test section for the water bulk and the heater, respectively. The predictions for the water bulk give a good agreement between the EMP and VOF model. The errors between two models are less than 2E-4 percent for all the mesh size though this is not the case for the values from heater. For the heater, the maximum error is about 2.44E-3 percent in the case with 0.4 *mm* wall thickness which is a magnitude larger than the value from the water bulk. One would be noticed that the volume averaged heater temperature shares a similar trend with surface averaged heater temperature. This may again indicate that the precursor simulations are converged to a good status.
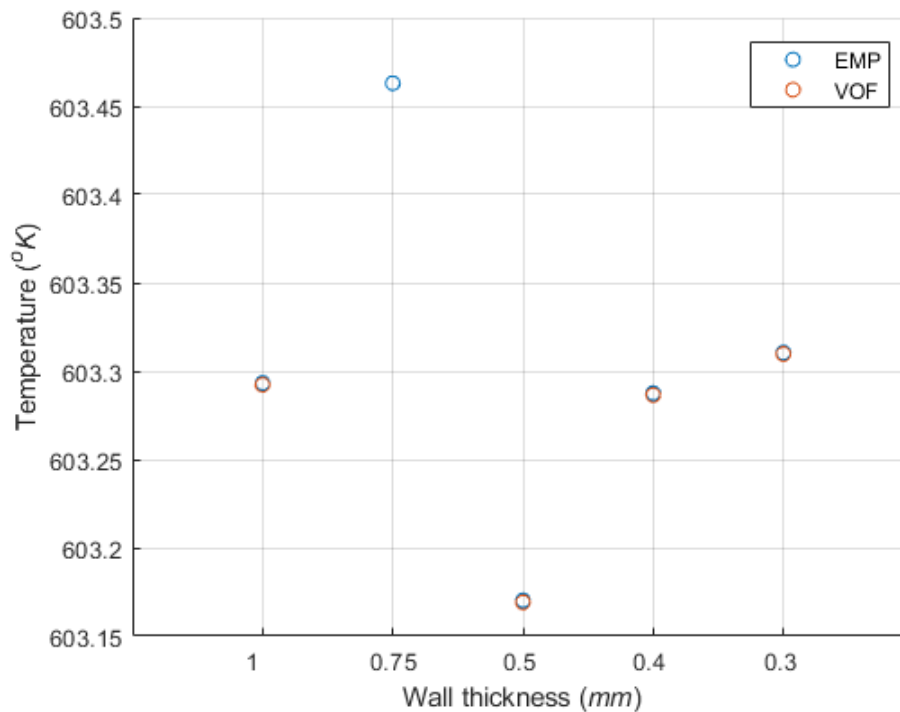
Fig. 44. Precursor simulation: volume averaged temperature of liquid
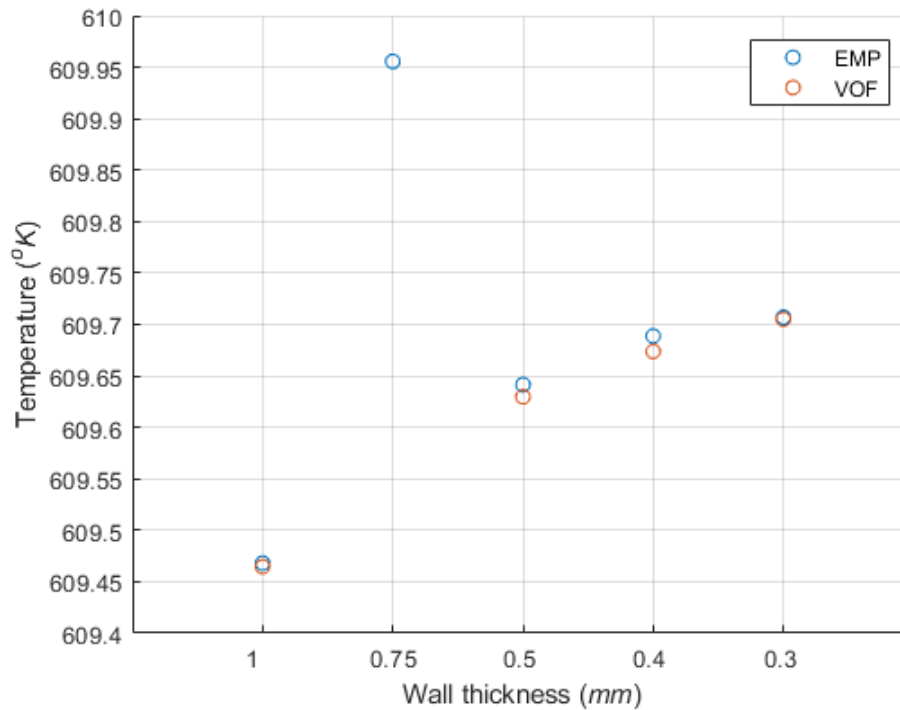
Fig. 45. Precursor simulation: volume averaged temperature of heater

Except the global thermal hydraulic behavior of the test section, the behavior at the end of the heater also provides a good understanding for the convergence. Fig. 46 and Fig. 47 are the averaged and maximum water temperature on the heated surface, respectively. In Fig. 46, it is clearly that the error between the EMP and VOF model is dependent on the mesh size. The more the meshes are refined, the less the error is given by both Eulerian multiphase models. Furthermore, the data series shows a clear view of a non-asymptotic convergence. Different from the averaged value, the maximum value may provide more discretization error and, thus, gives a stricter standard of convergence. It is found out that, in Fig. 47, the clear view of the convergence for maximum water temperature is not appeared since the case with 0.75 *mm* wall thickness from EMP model provides an out-trended temperature. As a result, an additional grid dependent study is needed to determine the convergence for the thermal hydraulic behavior on the surface of heater end.
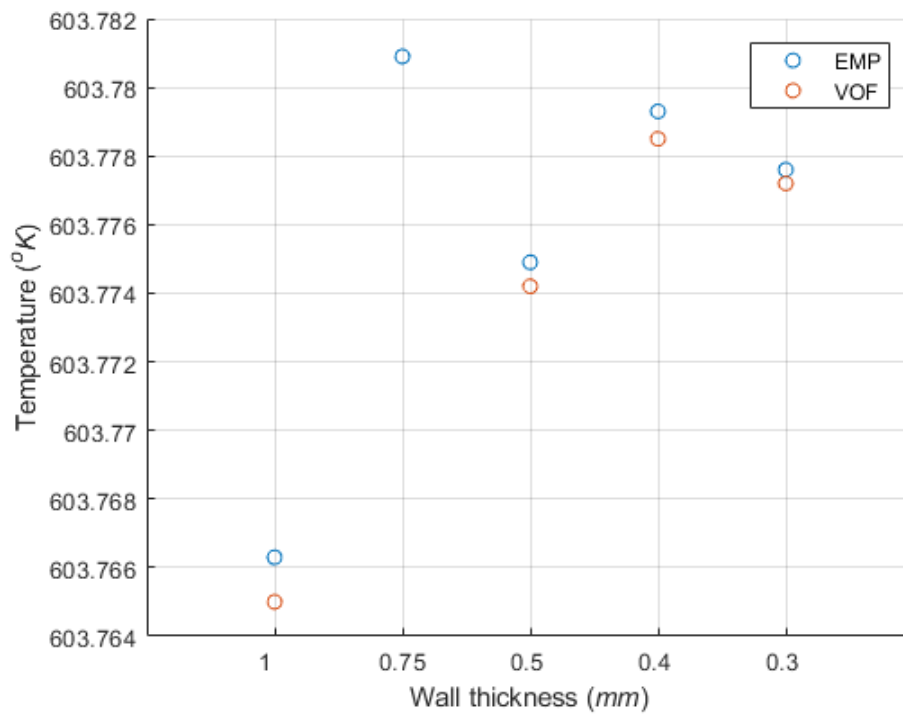
Fig. 46. Precursor simulation: heater end surface averaged temperature of liquid
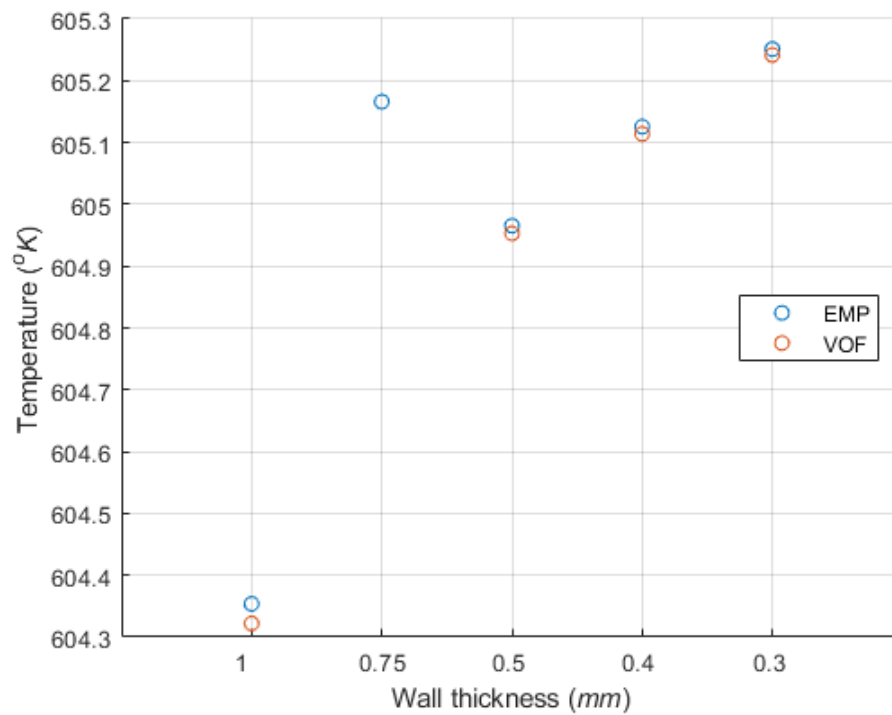
Fig. 47. Precursor simulation: heater end surface maximum temperature of liquid

Fig. 48 provides the surface averaged vapor volume fraction for all the precursor simulations. For VOF model, the prediction gives a perfect value for all the mesh size which is around 8.39E-5. However, for the EMP model, the prediction provides a large discretization error especially for the coarse mesh. This can be explained as the following reason. The EMP model considers continuous and dispersed phase independently while the VOF model considers a mixture phase only. The characteristic leads to a very different behavior of vapor volume fraction predictions from both models. Fig. 49 graphically shows the vapor volume fraction provided by EMP model at the end of the precursor simulation. The vapor is treated as dispersed phase and only occupied on the surface before the flow enters test section. The result is given by the modification of the inlet turbulent boundary condition as discussed in the stability maintenance section. On the contrary, as shown in Fig. 50, the vapor volume fraction from the VOF model gradually decreases along the flow channel though the same modification is made for the inlet boundary condition. Such fact provides a clear view that the vapor volume fraction is calculated as a global value of mixture phase instead of a local distribution of dispersed phase for the VOF model.
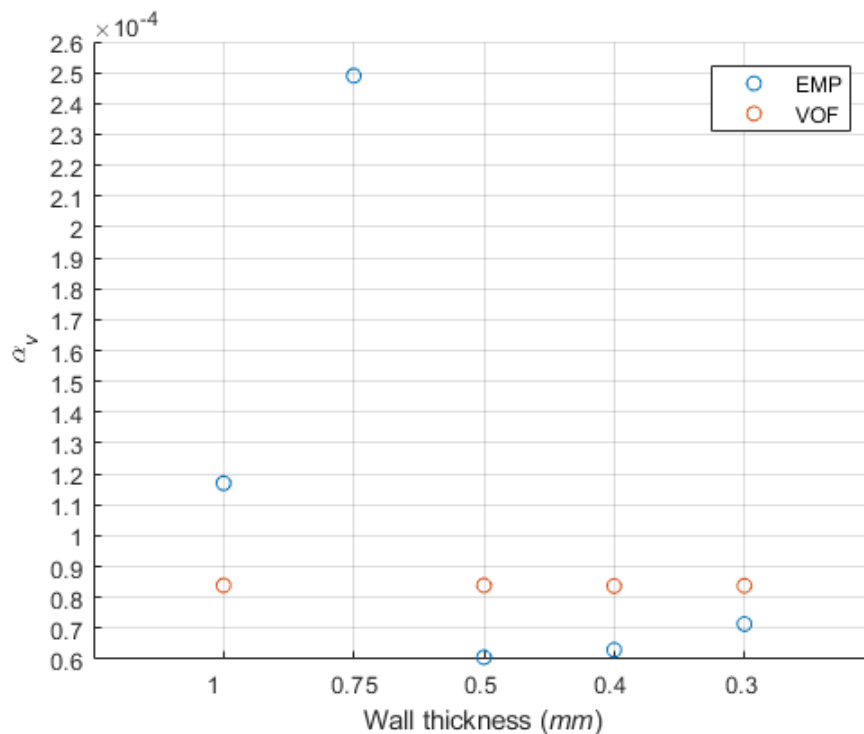
Fig. 48. Precursor simulation: surface averaged volume fraction of vapor
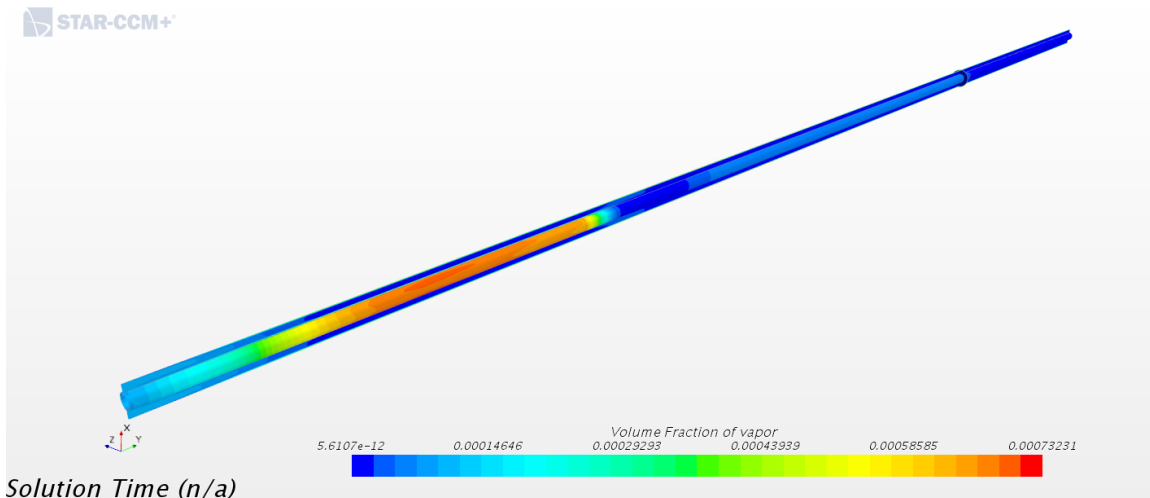
Fig. 49. Precursor simulation of EMP: vapor volume fraction of 0.4 *mm* wall thickness
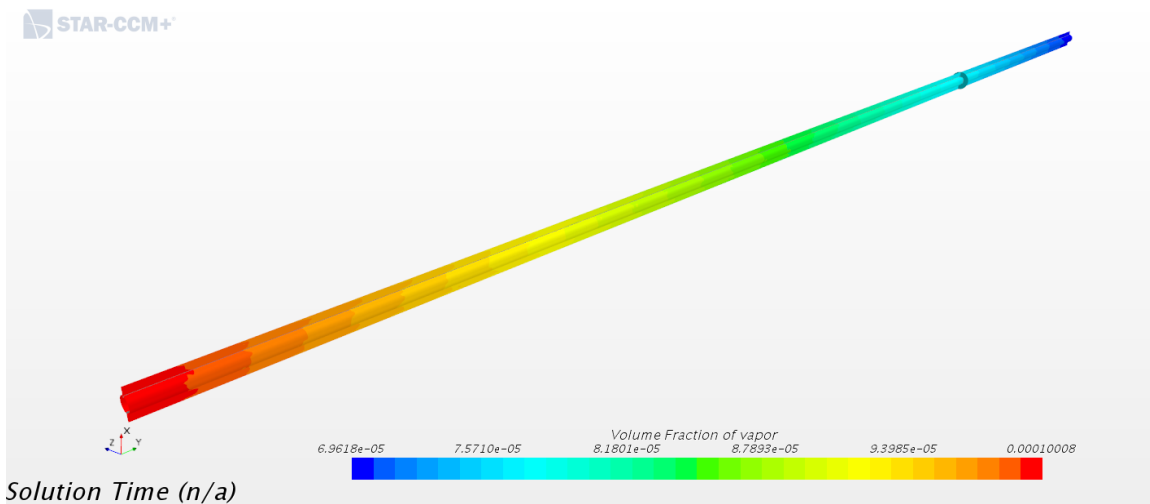
Fig. 50. Precursor simulation of VOF: vapor volume fraction of 0.4 *mm* wall thickness

4.2 Grid Independent Study

The discretization error is one of the most important concern that deciding the precision of the CFD studies. Typically, the discretization error is referred as the errors from the size of the spatial grid. In other words, the computation from a CFD software may show a very different result depends on the degree of mesh refinement. Theoretically, the more the mesh is refined, the more accurate the solution is. However, it is impossible to build an infinity small mesh set due the computational cost. Thus, to prevent the simulating results is highly influenced by the mesh size, a standard of judging discretization error is necessary.

Verification and Validation in Computation Fluid Dynamics and Heat Transfer (ASME, 2009), known as ASME V&V 20, was published by American Society of Mechanical Engineering (ASME) to provide a solution for identifying the discretization error from CFD simulations.

In the time-dependent case, for example, this study, the discretization error may further come from the size of temporal grid (time step). However, in most of the time-dependent case, the temporal grid is very likely decreasing due the stability concern. For all the time-dependent simulation included in this study, a time step of 1E-4 is considered. With the usable computational source, such time step is the lowest level that can be reached by the author. Thus, an additional time independent study is not performed in this study. It should be noticed that, though the time independent study is ignored, the influence of the time is still a consideration. As shown in Table. 38, all the grid independent studies are developed until reaching the physical time of 0.1 s by using implicit unsteady state time model.

Recall that the URFs are reduced to 0.1 for the stability maintenance. During the bench mark simulation with 50 ms heating period (the case with the largest heating rate in this study), it is found out that, due to the using of low URFs, the inner iteration with the number of 500 in each time step is necessary for the residual to reach an acceptable low value. Thus, the grid independent studies are developed with the same stopping criteria as using for the bench mark simulations. Moreover, all the simulations in the gird independent study are developed with the total heat source of 10 kW due to the consideration of the computational cost. Based on the precursor simulations mentioned in previous section, the total heat source is increased from 2.4 kW to 10 kW without delay in the beginning of the grid independent studies. Then, the predicted values at physical time of 0.1 s are collected to perform the grid independent study by the using of GCI method.

4.2.1 Data Series

To obtain a significant increasing rate of the cell number, the grid independent study is designed to adopted with wall thickness of 1.0, 0.5, 0.4 and 0.3 mm. However, it is found out that in the case with 0.3 mm wall thickness, the EMP model faces a challenge to

maintain stability and diverged at first several time step after the boiling incipience. Thus, the EMP case with 0.3 *mm* wall thickness is not provided in this study. Instead, for the EMP model, an additional case with wall thickness of 0.75 *mm* is provided in order to get a complete application of grid convergence index.

Fig. 51 is the boundary heat flux on heater-coolant interface. Though the precursor simulations provide close values for both EMP and VOF model, this is obviously not the case for the time-dependent simulations. The prediction gives the error between EMP and VOF model up to about 2.1E+4 *W/m²* for the case with 1.0 *mm* wall thickness. However, the discretization error within each model is less than 1 percent and a clear trend of convergence is presenting either by oscillatory or monotonic.
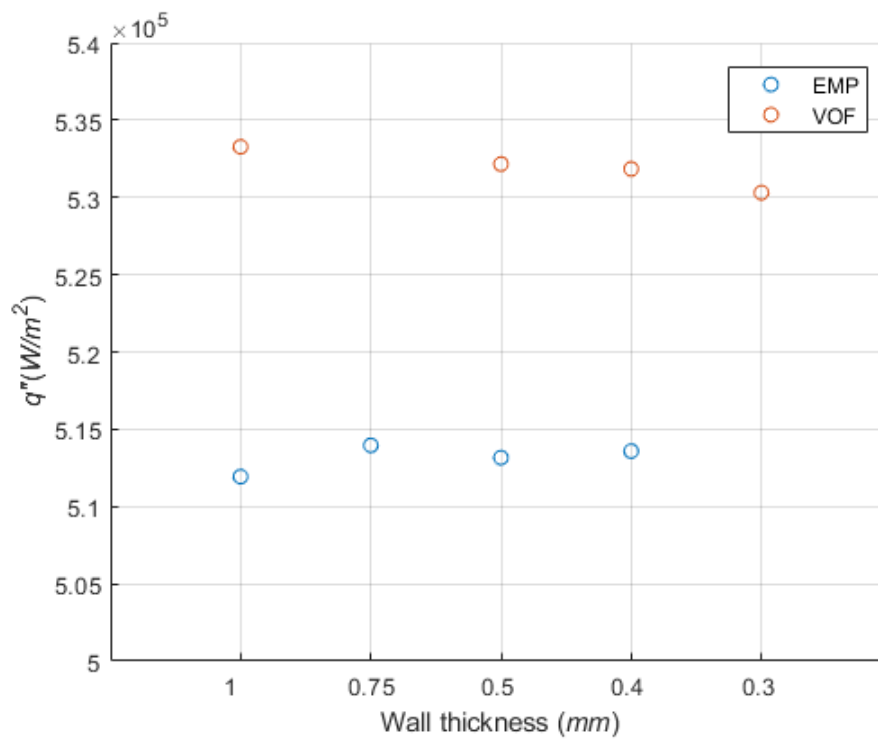
Fig. 51. 10 *kW*: surface average heat flux of the heater

Fig. 52 and Fig. 53 are the temperature behavior on the heater surface. The wall superheat, again, is calculated using (4.1). From Fig. 53, the conclusion that boiling is already incipient at the physical time of 0.1 *s* can be easily made since the wall superheat is more than 2 $°K$

for all the cases. Thus, it is reasonable to collect the results at physical time of 0.1 *s* to determine how two-phase simulations are influenced by spatial grid size. The surface averaged temperature shows almost the same trend as boundary heat flux. However, the EMP model predicts a higher value for surface temperature with lower boundary heat flux. This result is expected since the heat is removed slower from the heater and leads to a fast-rising temperature in the heater region. From the aspect of discretization error, the VOF model gives a better result since the surface averaged temperature is converged to a value asymptotically while the EMP model only provides an oscillatory convergence.
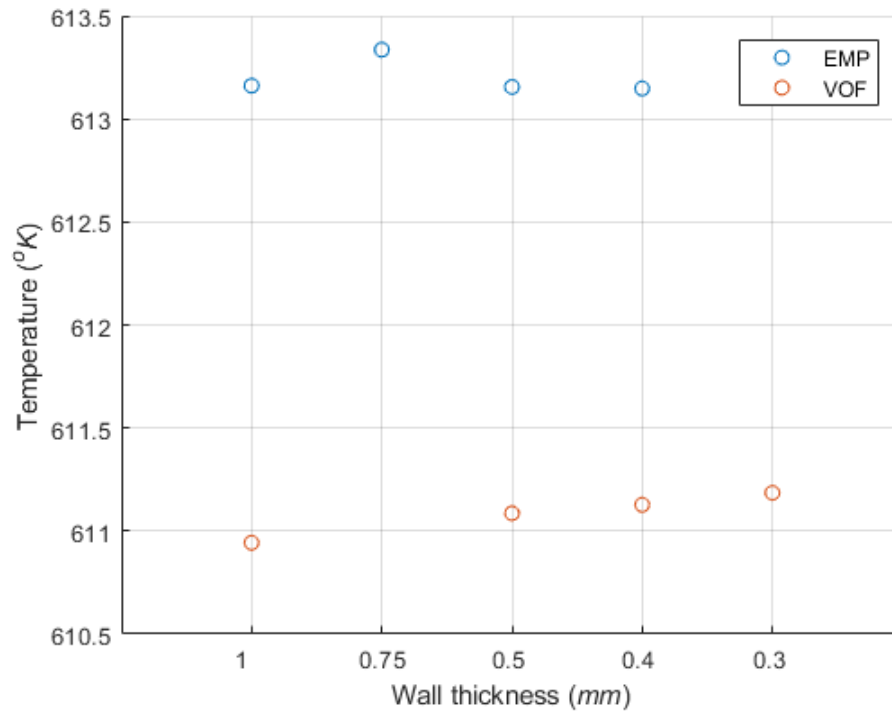
Fig. 52. 10 *kW*: surface averaged temperature of the heater
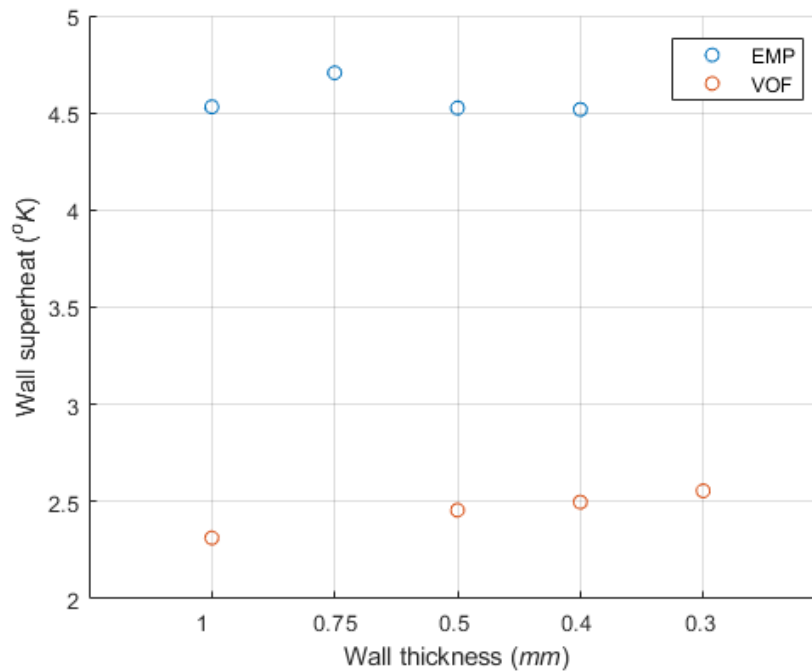
Fig. 53. 10 *kW*: wall superheat of the heater

The volume averaged temperature for the fluid and heater region are shown in Fig. 54 and Fig. 55, respectively. The predicted volume averaged temperature for the water bulk seems to be highly dependent on the spatial grid size for both models because of the oscillatory results. However, the low error between cases with different models and grid sizes may be concluded as the reason for the oscillatory convergence. As shown in Fig. 54, the converged discretization error from the volume averaged temperature is hard to distinguish only by the data series since the error is less than 0.3 $°K$ or 5E-2 percent for all the cases. Except the influence from the low error, the non-structured refined method that adopted in this study may serve as another candidate that should responsible for the oscillatory result. The low error with the oscillatory results is very likely to introduce since the predictions are based on the volume average of the entire fluid region while the refinement is only applied for the meshes near the surface. For the heater behavior, the predictions give a good view of converged discretization error for both model no matter in oscillatory or monotonic manner. However, the low error between different mesh sizes may become a potential issue for applying grid convergence index since the refinement factors are limited by the refinement method which is further limited by the geometry.
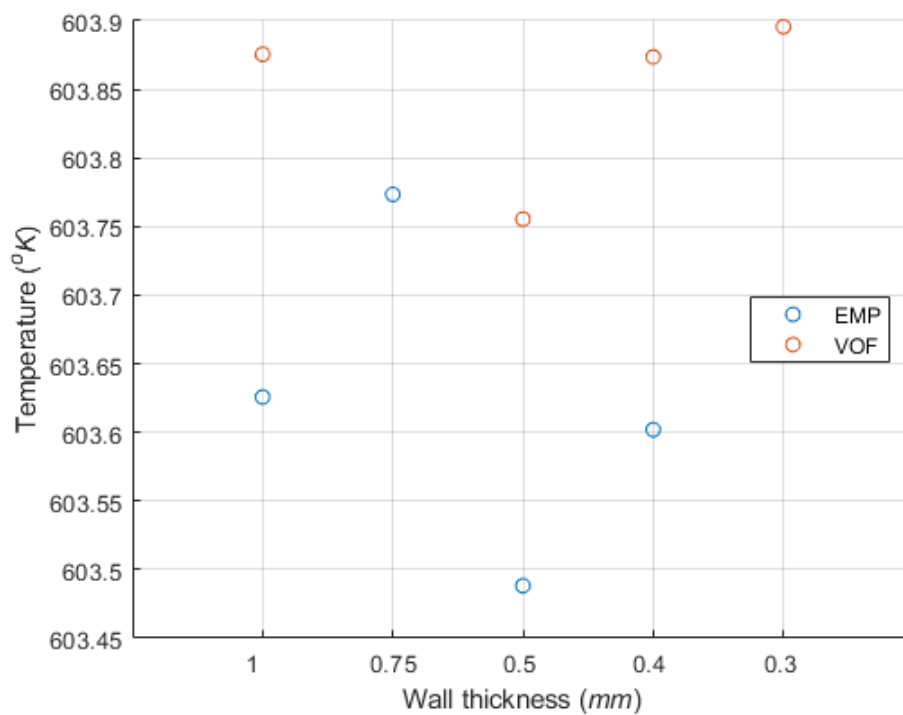
Fig. 54. 10 *kW*: volume averaged temperature of liquid
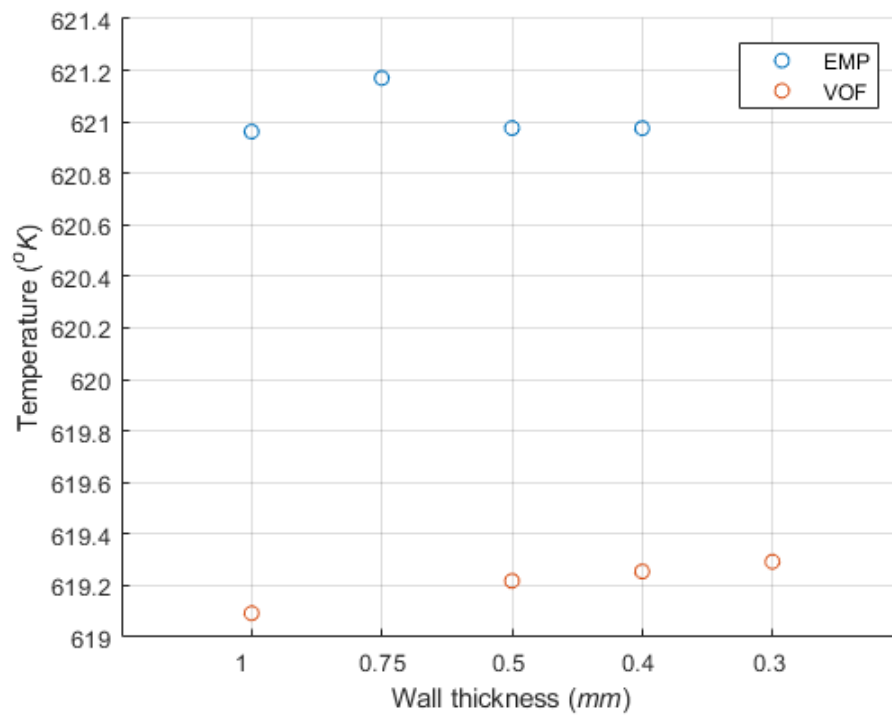
Fig. 55. 10 *kW*: volume averaged temperature of the heater

The surface temperature profile on the end of the heater is provided in Fig. 56 and Fig. 57 for averaged and maximum value, respectively. The surface averaged temperature is highly agreed with each other among the cases with different wall thickness. It should be noticed that the surface averaged temperature from the VOF model is predicted to be higher than the EMP model at 0.1 s which is different form the prediction from the precursor simulations as shown in Fig. 46. The results can be confirmed by the fact that the higher averaged boundary heat flux is provided by the VOF model. From the aspect of energy conservation, the higher rate of heat removal from the heater leads to an increasing of heat enter the fluid region and, thus, a higher temperature prediction for the liquid on the heater surface. This result is also confirmed by the surface and volume averaged temperature of the heater. For the maximum temperature, Fig. 57 provides the result with high discretization error among the cases with different spatial grid size. Although the maximum value is not preferred for grid independent study due to the possibility of error over estimated, a good view of converged discretization error still present by both VOF and EMP model for the maximum value.
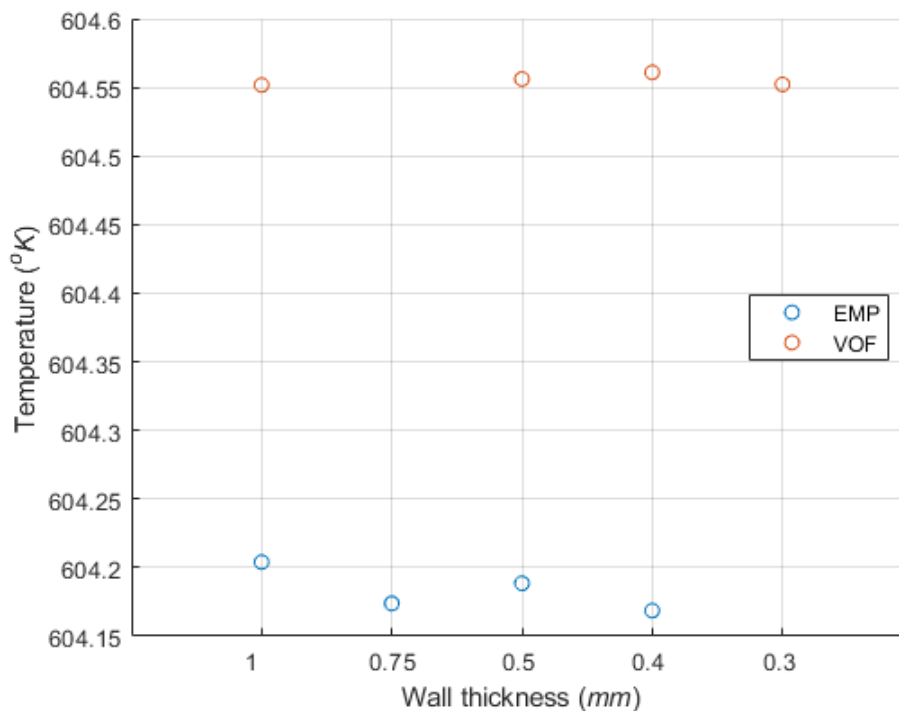
Fig. 56. 10 kW: heater end surface averaged temperature of liquid
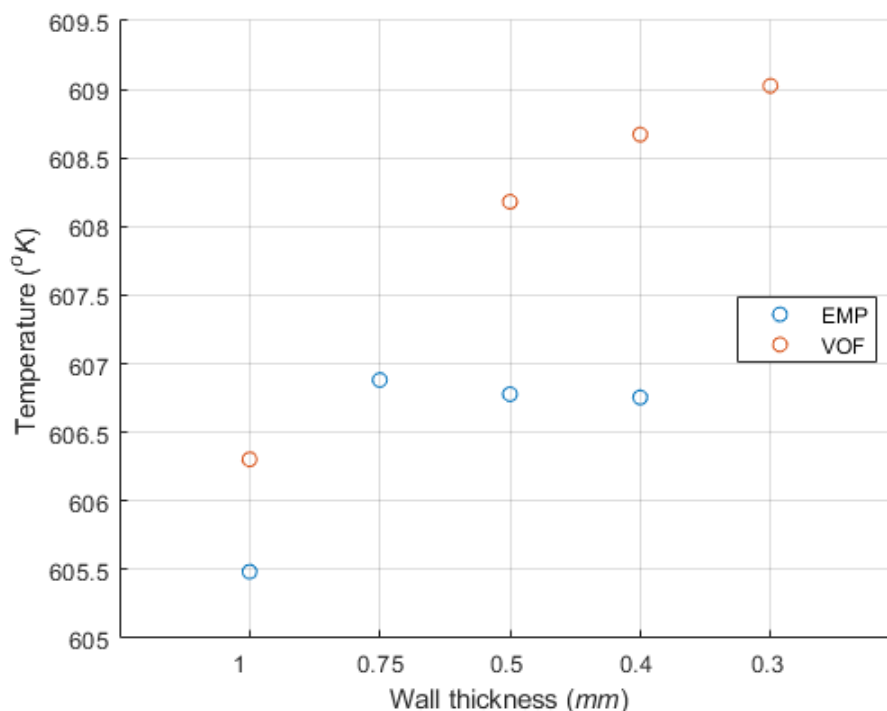
Fig. 57. 10 *kW*: heater end surface maximum temperature of liquid

For the vapor volume fraction, the simulations provide a highly scatter predication especially for EMP model. In Fig. 58, it is obvious that the EMP model provides a diverged result for the vapor volume fraction while the VOF model show a reasonable monotonically convergence. Two reasons can be attributed for the observation. First, the discretization error is very likely to be amplified by the complicated physics. As shown in Fig. 49 and Fig. 50, the complicated physics behind wall boiling and interphase mass transfer model provides a very different result of vapor volume fraction for EMP model compared to the VOF model. It is believed that most of the oscillatory convergence for the EMP model is contributed by the complicated model usage since VOF model shows a good ability of the convergence. Second, for the stability concern, the second order of precision is adopted for all the solvers in this study except for the volume fraction solver, the using of the first order of precision (this is also the default setting) may somehow influence the convergence behavior since a lower accuracy result is predicted by the simulations. It is expected that the determined order of accuracy from grid independent study may face challenge to reach a value higher than 2.
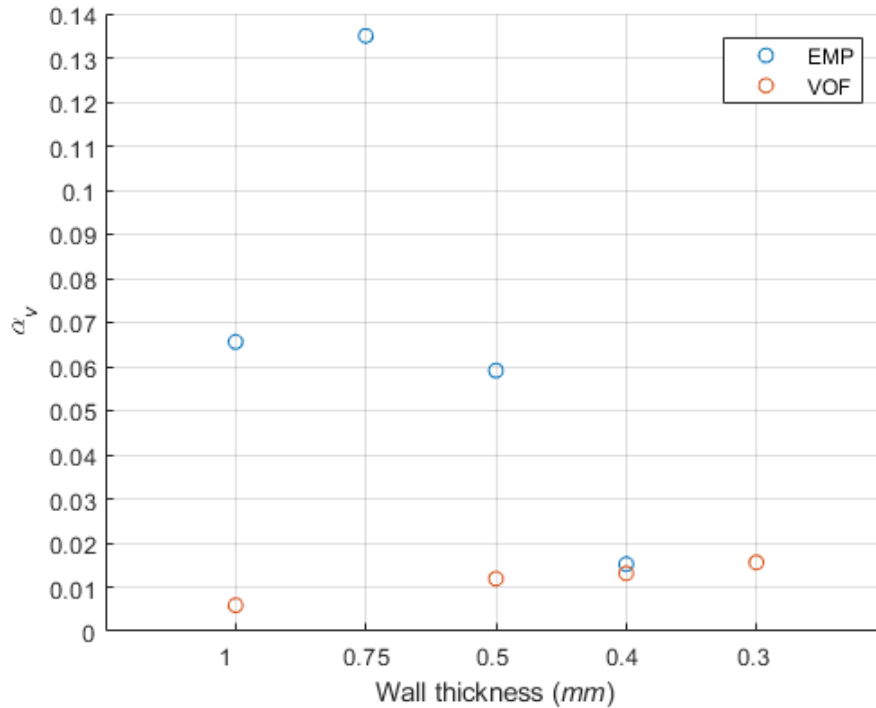
Fig. 58. 10 *kW*: surface averaged volume fraction of vapor

4.2.2 *Grid Convergence Index Method*

Grid Convergence Index (GCI) method is an industry standard for grid independent study which is recommended by ASME V&V 20 and admitted by the Journal of fluid Engineering (JFE). As a widely utilized method, GCI method provides a straightforward procedure to calculate the discretization error based on Richardson extrapolation (Richardson, 1911) as,

$$\bar{y} = y_k - ah_k^{P_f},$$ (4.2)

where $\bar{y}$, y_k and α are real solution, the grid-specific solution and unknown coefficient, respectively. The term, P_f, is the formal order of accuracy which should larger than 2 to comply with the standard. With the solution from different spatial grid size, the GCI method can be applied by following procedure.

- Define a representative mesh size, *h*. For the three-dimensional non-structured mesh, *h* can be calculated by

$$h = \left[(\sum_{i=1}^{N} \Delta V_i) / N \right]^{\frac{1}{3}}. \tag{4.3}$$

where ΔV_i is the volume of cell i and N is the total number of cells with in the geometry.

- Select three different solution to determine the grid refinement factor, r, using

$$\text{r} = h_{coarse} / h_{fine}. \tag{4.4}$$

It should be noticed that the grid refinement factor is recommended by (Celik et al, 2008) to be greater than 1.3. However, in this study, the refinement is only applied on the prism layer cell on the heated surface for several reasons including, the low influence of the core mesh refinement (indicated by the past study) to the surface heat transfer behavior, limited geometry (the ration of diameter to length is 0.03125) and computational cost. These facts force an application of unstructured refinement and cause a small grid refinement factor. Since the low value of refinement factor (about 1.0) may introduce the round-off noise for the observed order of precision, (Patrick JRoache, 1998) suggested that a minimum value of 1.1 can be considered for simple geometry. Thus, the refinement factor is keeping at least around 1.1 in this study.

- Calculate following equations by fixed point iterating while $h_1 < h_2 < h_3$:

$$P_y = [1 / \ln(\text{r}_{21})][\ln |\varepsilon_{32} / \varepsilon_{21}| + q(P_y)], \tag{4.5}$$

$$q(p) = \ln[(\text{r}_{21}^{P_y} - s) / (\text{r}_{32}^{P_y} - s)], \tag{4.6}$$

$$s = 1 \cdot sign(\varepsilon_{32} / \varepsilon_{21}), \tag{4.7}$$

where $\text{r}_{21} = h_2 / h_1$ and $\varepsilon = f_2 - f_1$.

- Calculate extrapolated value for fine grid and coarse grid by

$$y_{21,ext} = (\text{r}_{21}^{P_y} y_1 - y_2) / (\text{r}_{21}^{P_y} - 1), \tag{4.8}$$

and

$$y_{32,ext} = (\text{r}_{32}^{P_y} y_2 - y_3) / (\text{r}_{32}^{P_y} - 1), \tag{4.9}$$

respectively.

- Obtain the relative error from original solution and extrapolated solution using

$$e_{21} = \left| \frac{y_1 - y_2}{y_1} \right|, \tag{4.10}$$

and

$$e_{21,ext} = \left| \frac{y_{12,ext} - y_1}{y_{12,ext}} \right|, \tag{4.11}$$

respectively.

- Obtain the fine-grid convergence index by

$$GCI_{21} = \frac{FS \cdot e_{21}}{r_{21}^{P_y} - 1}, \tag{4.12}$$

where FS is the safety factor which is originally designed as 3. (P. J.Roache, 1994) suggested that, with a structured refinement, the safety factor can be following reduced to 1.25, however, this is not the situation for this study. With the consideration, the number of 3 is adopted.

4.2.3 Summary of Grid Independent Study

One of the most important limitation for the GCI method is that the method is only working with the monotonically convergence. Though the oscillatory convergence is not absolutely indicating an unreasonable formal order of accuracy, an unusual result from the GCI method is very likely to be introduced by the oscillatory convergence. To determine the type of convergence, a convergence factor as

$$R = \frac{y_1 - y_2}{y_2 - y_3}, \tag{4.13}$$

can served as a general standard. Again, y_k is the grid specific solution for different parameter. For the mesh size from refined to coarse, the k starts from 1 to 3. Different type of the convergence is given by

$$
\begin{array}{ll}
0 < R < 1 & \text{for monotonically convergence} \\
R > 1 & \text{for monotonically divergence} \\
R < 0 \wedge |R| < 1 & \text{for oscillatory convergence} \\
R < 0 \wedge |R| > 1 & \text{for oscillatory divergence}
\end{array}
\tag{4.14}
$$

It should be noticed that these standards are based on a constant refinement factor. In other words, to deal with the varied mesh refinement factor in this study, a normalization by the refinement factor is necessary. The normalized method is given by

$$R_{norm} = \frac{(y_1 - y_2)/r_{21}}{(y_2 - y_3)/r_{32}} .$$ (4.15)

Table. 39 provides the representative mesh size and corresponding refinement factor for all the grid independent simulation applied in this study. Due to the extreme geometry from TRTL facility (the ratio of diameter to length is 0.03125), the structural refinement on both radius and length axial may lead to unnecessary increasing of computational cost. Thus, to balance stability and computational cost, the refinement method leads to the cell number and represent mesh size as summarized in Table. 39. According to Roache's study (1998), the recommended refinement factor should be at least about 1.1. The refinement factor for the VOF model in this study provides a close value to the standard, however, this is not the case for the EMP model. Recall that EMP model faces an unrecoverable diverged result with wall thickness of 0.3 *mm*. For a decent choice, the usage of mesh size with 0.4 *mm* of wall thickness for the grid independent study leads to a limited refinement factor. It is believed that the low refinement factor is partially responsible for the oscillatory convergence shown in EMP cases, at least, in some degree.

Table. 39. Representative mesh size and refinement factor

	Wall thickness	$\Sigma\Delta V_i$	N	h	r
EMP	0.4 *mm*		185316	0.001133 (h_1)	1.150212
	0.75 *mm*		121781	0.001304 (h_2)	1.042344
	1.0 *mm*	2.698174E-4 (m^3)	107534	0.001359 (h_3)	
VOF	0.3 *mm*		230210	0.001054 (h_1)	1.098642
	0.5 *mm*		173602	0.001158 (h_2)	1.173103
	1.0 *mm*		107534	0.001359 (h_3)	

Table. 40 and Table. 41 provides the difference between grid specific solutions and their corresponding convergence factor. For the VOF model, most of the parameter provides a converged result in monotonically manner. The two exceptions for the divergence are surface averaged heat flux and volume averaged temperature of liquid. The reason for this

is unknown, however, the converged result for most of the parameters may indicate that the VOF model is suitable for the application of GCI method. For the EMP model, due to the complicated physics behind two-phase treatment and low refinement factor led by the limited geometry, most of the parameters provide an oscillatory convergence. This may indicate that GCI method may be inappropriate for the EMP model. It should be noticed that the convergence factor for vapor volume fraction provides an unreasonably large value. This is contributed by the scattered prediction for vapor volume fraction and the small predicted value. Recall that the first order of precision is adopted for volume fraction solver due to stability concern, the scattered prediction is expected. In addition, if the small predicted value due to the very beginning of the boiling is combined with the scattered prediction, the error is very likely to be amplified and, thus, causes a diverged convergence factor.

Table. 40. Normalized solution difference and convergence factor for VOF model

VOF	ε_{21}	ε_{32}	$\varepsilon_{21,norm}$	$\varepsilon_{32,norm}$	R
Surface averaged heat flux of the heater	1853.9	1113.1	1687.45	948.85	1.7784
Surface averaged temperature of the heater	-0.0993	-0.1429	-0.0904	-0.1218	0.7420
Wall superheat	-0.0993	-0.1429	-0.0904	-0.1218	0.7420
Volume averaged temperature of the liquid	-0.1402	-0.1201	-0.1276	0.1024	-1.2465
Volume averaged temperature of the heater	-0.0746	-0.1255	-0.0679	-0.1070	0.6347
Surface averaged vapor volume fraction	-3.71E-3	-7.24E-3	-0.0034	-0.0062	0.5466
Heater end surface averaged temperature	0.0039	-0.0044	0.0035	-0.0038	-0.9464
Heater end maximum temperature	-0.8455	-1.8775	-0.7696	-1.6	0.4809

Table. 41. Normalized solution difference and convergence factor for EMP model

EMP	ε_{21}	ε_{32}	$\varepsilon_{21,norm}$	$\varepsilon_{32,norm}$	R
Surface averaged heat flux of the heater	372.6	-2026.9	323.9404	-1944.56	-0.1666
Surface averaged temperature of the heater	0.1884	-0.1749	0.1638	-0.1678	-0.9762
Wall superheat	0.1884	-0.1749	0.1638	-0.1678	-0.9762
Volume averaged temperature of the liquid	0.1715	-0.1477	0.1497	-0.1417	-1.0523
Volume averaged temperature of the heater	0.1947	-0.2077	0.1693	-0.1993	-0.8495
Surface averaged vapor volume fraction	1.2E-1	6.56E-3	0.1046	0.0063	16.6311
Heater end surface averaged temperature	0.0053	0.03	0.0046	0.0288	0.1601
Heater end maximum temperature	0.1267	-1.3971	0.1102	-1.3403	-0.0822

Table. 42 and Table. 43 present the results for the grid independent study for both VOF and EMP model, respectively. For VOF model, most of the parameter with monotonically convergence provides a reasonable observed order of accuracy. The only exception is the volume averaged temperature of the heater. The result remains unknown since a nearly perfect monotonically convergence is given by the convergence factor. The observed order of accuracy for the vapor volume fraction provides a value of 0.6656 which is far away from the standard of 2. However, recall that the first order of accuracy is adopted in the volume fraction solver, the standard here should be the value of 1 instead of 2. Thus, an order of accuracy with the value 0.6656 is acceptable. It should be noticed that unreasonable order of accuracy provided for the surface averaged heat flux due to the monotonically divergence may indicate the order of accuracy for volume averaged temperature is also not reliable due to the oscillatory divergence though a good value of 2.7853 is provided. For the EMP model, almost all the parameter provides an unreasonable order of accuracy no matter high or low. This result is expected since most the convergence factor for EMP case reveals a pattern of oscillatory convergence. Such fact further confirms that the GCI method is not suitable for the EMP simulation in this study. Since this study is not focusing on the finite discretization method and its possible error from the grid size,

the GCI is the only method discussed in this study. For more detail about applying gird independent study with oscillatory convergence, other method should be considered.

As a conclusion, the VOF model in this study provides a fair result on the grid independent study by applying GCI method. Since VOF model contains less stability issue and complicated physics, the monotonically convergence is shown in most of compared parameters. With the monotonically convergence, GCI method provides a good ability to judge the error from the spatial grid, however, this is not the case for EMP model. The unsuccessful grid independent study for the EMP model can be attributed to two main reasons. First, a potential stability issues provided by the lower limit of the surface mesh size. Since a lower limit of surface mesh size is observed, an enough refinement factor is hard to satisfy. Second, the complicated physics from the wall boiling and interphase mass transfer model lead to potential issues that cause an oscillatory convergence. Since GCI method is only working well with monotonically convergence, other method should be considered for the EMP model in the future. It should be noticed that no matter how grid independent studies are performed in this study, the mesh refinement is considered to be fairly enough because the small diameter of the pipe. Furthermore, with the significant issues from stability and computational cost, the refinement performed in this study is the best solution that can be attained by the author.

Table. 42. GCI application for VOF model

VOF	y_1	y_2	y_3	P_y	$y_{21,ext}$	e (%)	$e_{21,ext}$ (%)	GCI (%)
Surface averaged heat flux of the heater	530306.2	532160.1	533273.2	21.6732	530030	0.21	5.23E-2	0.16
Surface averaged temperature of the heater	611.1854	611.0861	610.9432	2.7777	611.5179	1.62E-2	5.44E-2	0.16
Wall superheat	2.5554	2.4560	2.3132	2.7874	2.8870	3.89	11.5	38.9
Volume averaged temperature of the liquid	603.8957	603.7555	603.8756	2.7853	604.3637	2.32E-2	7.74E-2	0.23
Volume averaged temperature of the heater	619.2926	619.2180	619.0925	0.1427	624.8115	1.2E-2	0.88	2.67
Surface averaged Vapor volume fraction	1.56E-2	1.19E-2	5.87E-3	0.6656	0.0729	23.72	78.59	110.119
Heater end surface averaged temperature	604.552	604.5561	604.5517	0.9365	604.5099	6.45E-4	7.01E-3	2.1E-2
Heater end maximum temperature	609.0264	608.1809	606.3034	2.0954	612.9067	0.14	0.63	1.91

Table. 43. GCI application for EMP model

EMP	y_1	y_2	y_3	P_y	$y_{21,ext}$	e (%)	$e_{21,ext}$ (%)	GCI (%)
Surface averaged heat flux of the heater	513586.5	513959.1	511932.2	36.1304	513584.1	7.25E-2	4.65E-4	1.4E-3
Surface averaged temperature of the heater	613.1476	613.3360	613.1611	0.3912	609.7998	3.07E-2	5.5E-2	1.64
Wall superheat	4.5176	4.7060	4.5311	0.3916	1.1732	4.17	285	220
Volume averaged temperature of the liquid	603.602	603.7735	603.6258	0.7825	602.1201	0.25	2.84E-2	0.74
Volume averaged temperature of the heater	620.9755	621.1702	620.9626	0.7255	619.1536	3.14E-2	0.29	0.88
Surface averaged Vapor volume fraction	1.52E-2	1.35E-1	6.56E-2	2.7942	2.2352	788.16	106.46	4941.23
Heater end surface averaged temperature	604.1686	604.1739	604.2039	45.6875	604.1686	8.77E-4	1.47E-6	4.41E-6
Heater end maximum temperature	606.7548	606.8815	605.4844	55.5971	606.7547	2.09E-2	8.73E-6	2.62E-5

4.3   Transient Boiling

In this study, the transient simulation is performed with a heating period of 50, 75 and 100 *ms*, respectively. The performance of the simulation is briefly summarized as following:

- The VOF model is not able to perform a reasonable boiling process of a transient heat increasing.
- The EMP model is able to perform a transient heat increasing process with reasonable physics and CHF value.
- The higher CHF is observed in EMP cases with shorter heating period.
- The temperature overshoot (OV) is observed with EMP model. A trend of increasing of the OV is reveled with decreasing of heating period.
- A significant difference of the boiling process is observed with shorter heating period.

4.3.1   Heat Flux

Fig. 59 and Fig. 60 are the surface averaged heat flux with different heating period from the EMP and VOF model, respectively. The heat flux is acquired from the solid region side of the cladding-fluid interface. It is clearly that the VOF model is failed to predict the boiling process under the transient scenario. Since the VOF model adopts Rohsenow's correlation, which is developed under the frame of steady state boiling, it is foreseeable that the VOF model is lack of the ability to predict transient boiling process. In this study, all the VOF simulations remain in the nucleate boiling region even when the heat flux reaches a high level. It is found out that the extremely low vapor volume fraction is predicted by the VOF model during the heat flux build-up. Such fact leads to an unreasonable prediction of the boiling curve. Furthermore, most of the VOF cases diverged after the time step that transition boiling is observed in EMP model. The reason of the divergence is very likely due to the unreasonable prediction of physics and boiling pattern behind the simulation which leads to the accumulation of the error. When the surface heat flux reaches the transition boiling region, the simulating physics is no longer possible to maintain stable. In Fig. 60, the end of the curves indicates the diverged time step of the VOF model.

Fig. 59. EMP model: surface averaged heat flux against heating period
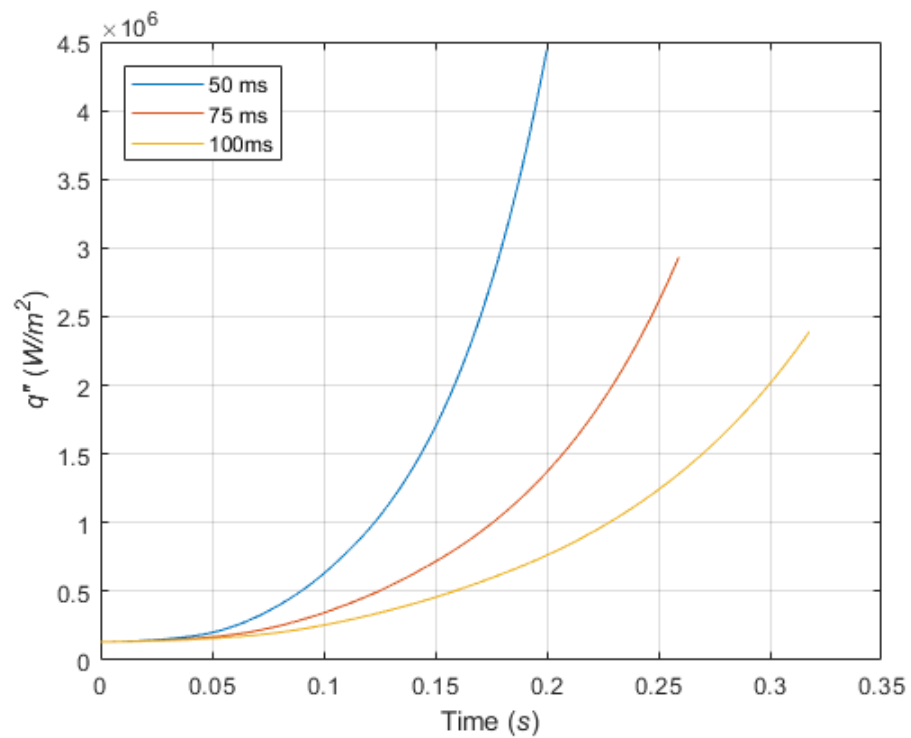
Fig. 60. VOF model: surface averaged heat flux against heating period

In the contrary, the EMP model provides a good ability of predicting the transient boiling. Table. 44 summarizes the CHF value and their corresponding time step. Recall that it is expected that the decreasing of the heating period leads to the increasing of the CHF. A clear trend of increasing of the CHF is revealed in Fig. 59. During the surface heat flux build-up, a significant difference of the boiling pattern is observed with the shorter heating period which causes a higher predicted value of transient CHF. It is believed that this behavior is introduced by the OV which is also discussed in literature survey. Nevertheless, it is surprised that such phenomenon can be predicted by the CFD code since the OV is believed to be introduced by a very different mechanism compared to steady state boiling. It should be noticed that the wall boing model is developed under the frame of steady state boiling which means the physics behind the model is based on the steady state scenario. The success of predicting OV and its corresponding higher value of CHF may indicate that the mechanism behind the transient boiling may not be very different from the steady state boiling. In the case with 50 *ms* heating period, two peaks are observed on the boiling curve. A suddenly vapor forming and detaching on the heated surface leads to the occurrence of the first peak. Followed by the suddenly vapor detaching from the heated surface, a higher heat flux is reached as CHF at second peak. A reasonable explanation for the second peak is that the rewetting caused by the sudden vapor detaching provides a duration for heat flux builds up before the CHF and transition boiling region reached. This mechanism is weakened by the increasing of the heating period. In the case with 75 *ms* heating period, two peaks are remaining observed on the boiling curves, however, the difference between the two peaks are considered to be very small compared to the simulation with 50 *ms* heating period. For 100 *ms* heating period, this phenomenon is no longer observed. In this study, all the EMP simulations are halted by the author after the confirmation of the CHF. The ends of the boiling curves in the Fig. 59 indicate the stopping time steps of the simulation which are 2000 *ms*, 3000 *ms* and 3500 *ms* for the heating period of 50 *ms*, 75 *ms* and 100 *ms*, respectively.

Table. 44. CHF and corresponding time step

	τ	CHF (MW/m^2)	CHF reached time (ms)	Halted time step
	50 ms	3.6-3.9	1800-1900	2000
EMP	75 ms	~2.5	~2620	3000
	100 ms	~2.15	~3060	3500
	50 ms	N/A	N/A	2000
VOF	75 ms	N/A	N/A	2591 (diverged)
	100 ms	N/A	N/A	3177 (diverged)

4.3.2 Temperature

Fig. 61 and Fig. 62 are the surface averaged temperature against heating period for the EMP and VOF model, respectively. The right y-axis is the surface averaged temperature obtained from the solid side of cladding-fluid interface and the left y-axis is the wall superheat calculated by (4.1). For the VOF model, the linear increasing of the temperature profile indicates all the boiling remains in the nucleate boiling region. It is clearly that no significant transfer from nucleate boiling is observed in any of the VOF simulation even with the wall superheat more than 20 $°K$ (a rule of thumb that indicates the occurrence of CHF). On the other hand, from the wall temperature aspect, the OV is revealed clearly in Fig. 61. In the simulation with heating period of 50 ms, the surface averaged OVs to about 650 $°K$ with about 40 $°K$ of wall superheat at the first peak of the boiling curve. According to past study, the reason for the OV is remaining debating since it is challenging to capture and study such fast phenomenon under extreme conditions. However, it is confirmed in this CFD study that such OV is caused by the fast increasing of nucleate site number density. The instantaneous vapor generation on the surface cause a deterioration of surface heat transfer and leads to fast increasing of surface temperature. Accompanying with the vapor detaches from the heated surface, the temperature drops to a relatively low point about 630 $°K$. Furthermore, as shown in Fig. 61, this behavior is strongly weakened by the increasing of the heating period. The OV is almost unobservable in the case with heating period of 75 ms and eliminates within 100 ms heating period case. It should be noticed that the phenomenon mentioned above is only based on the observation of the CFD simulation. More empirical application is necessary for the confirmation of true mechanism behind the OV.
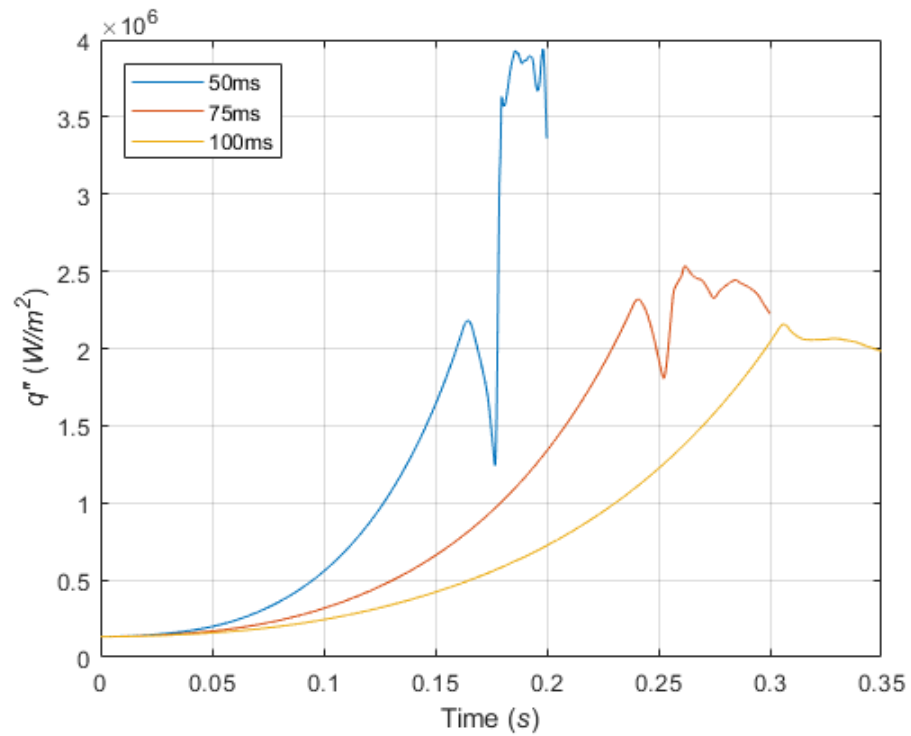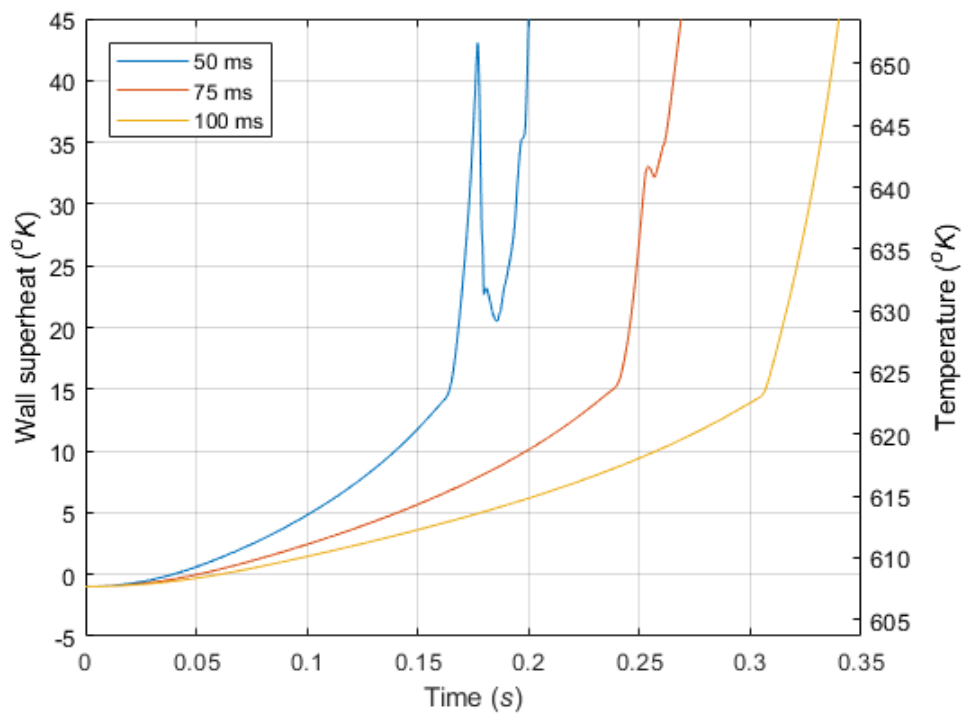
Fig. 61. EMP model: surface averaged temperature against heating period
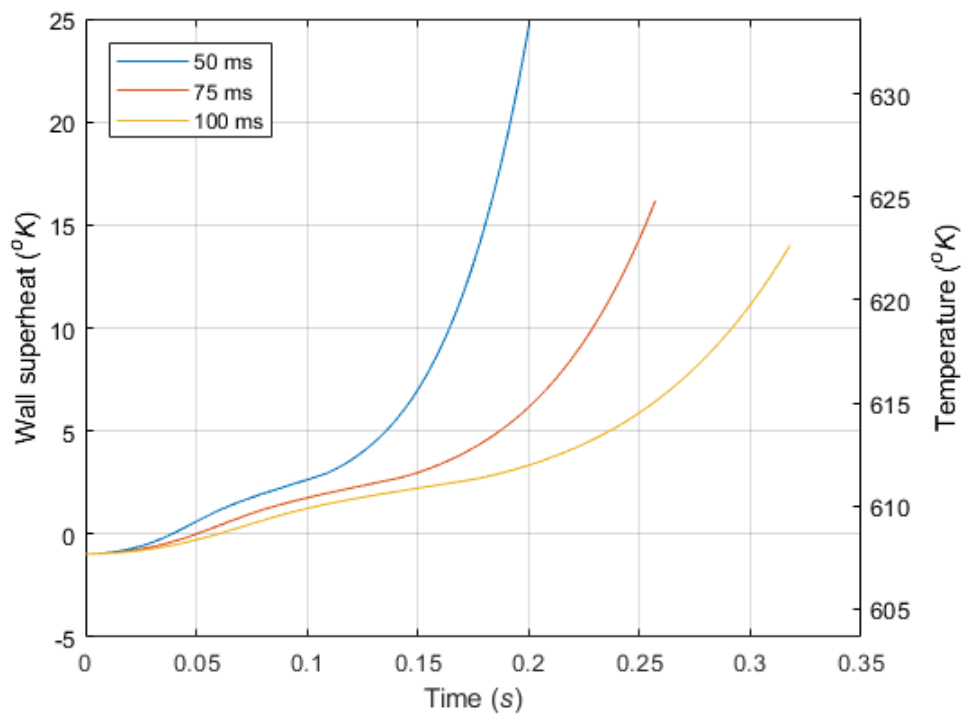
Fig. 62. VOF model: Surface averaged temperature against heating period

Fig. 63, Fig. 64 and Fig. 65 are the surface averaged temperature and heat flux respect to different heating periods. In general, the temperature is increased with the decreasing of the heat flux. Such behavior can be simply explained by Fourier's Law as

$$q'' = -k_{eff} \frac{\partial T}{\partial r} = k_{eff}(T_{Max} - T_{wall}) .$$
(4.16)

The decreasing of the surface heat flux due to reduction of heat transfer coefficient in the water bulk leads to the increasing of the heater surface temperature. Furthermore, with the simplified energy conservation equation,

$$\rho C_p(r,T) \frac{\partial T(r,t)}{\partial t} = \nabla \cdot \left[k_{eff}(r,T) \nabla T(r,t) \right] + q'''(r,t) ,$$
(4.17)

the time dependent heater energy behavior can be expressed as

$$\alpha(r,T) \frac{\partial T(r,t)}{\partial t} = -\nabla q''(r,t) + q'''(r,t) .$$
(4.18)

If the heat generates exponentially in the heat itself, the equation then becomes

$$\frac{P_0}{V_{heater}} e^{t/\tau} = \alpha(r,T) \frac{\partial T(r,t)}{\partial t} + \nabla q''(r,t) .$$
(4.19)

The left side of the equation indicates the total heat generating from the heater while the first term and second term on the right side indicate the heat deposit in the heater itself and the heat flux from the heater surface, respectively.

In Fig. 63, a clear view of OV caused by deterioration of heat removal ability due to the instantaneously explosive vapor generating is shown. With the continuous exponential heat input, the decreasing of the heat flux for the first peak followed by a sudden increasing of the wall temperature leads to the OV of more than 40 $°K$. Such phenomenon also observed from the simulation with 75 ms heating period, however, with the lower overshoot only about 30 $°K$. Nevertheless, from Fig. 65, since the first peak reaches CHF directly, the OV is no longer observed.
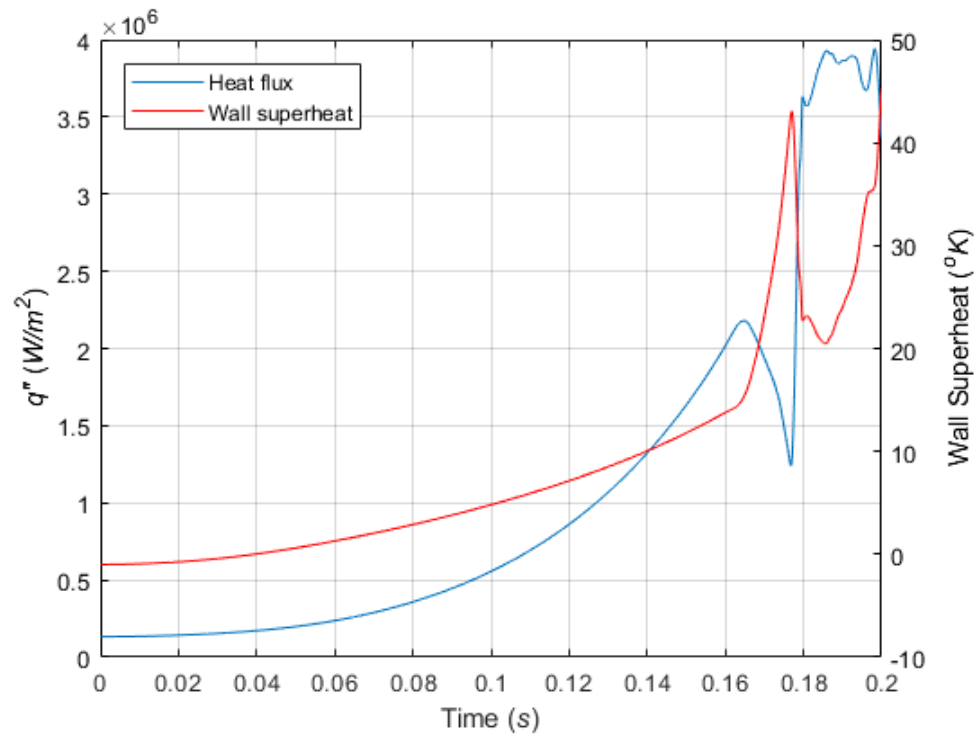
Fig. 63. Heating period of 50 *ms*: surface averaged temperature and heat flux
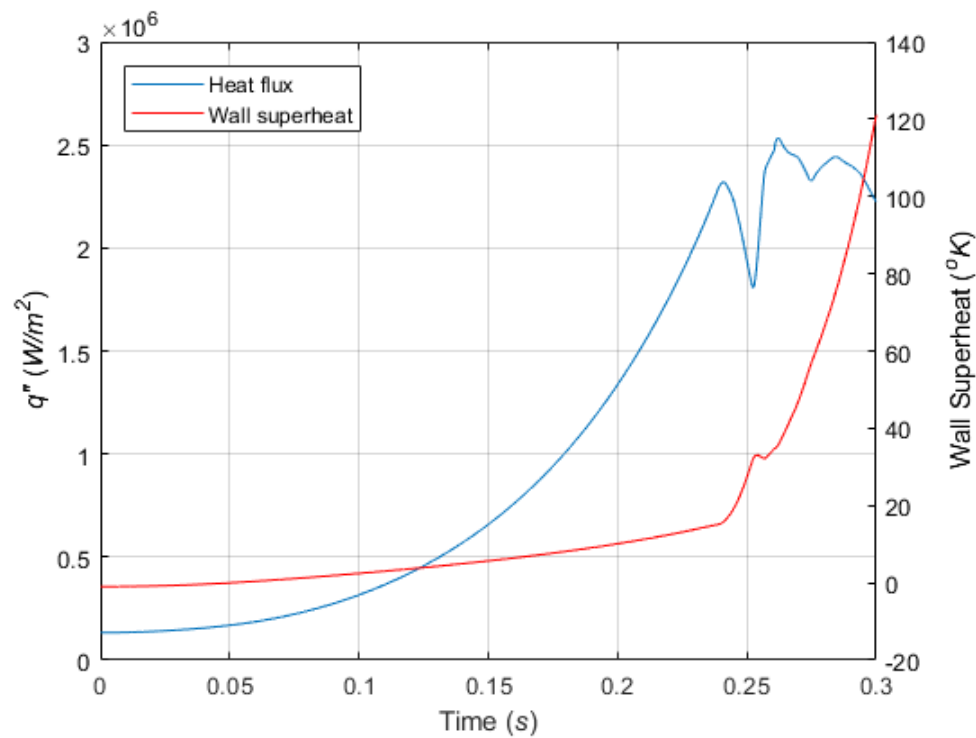
Fig. 64. Heating period of 75 *ms*: surface averaged temperature and heat flux
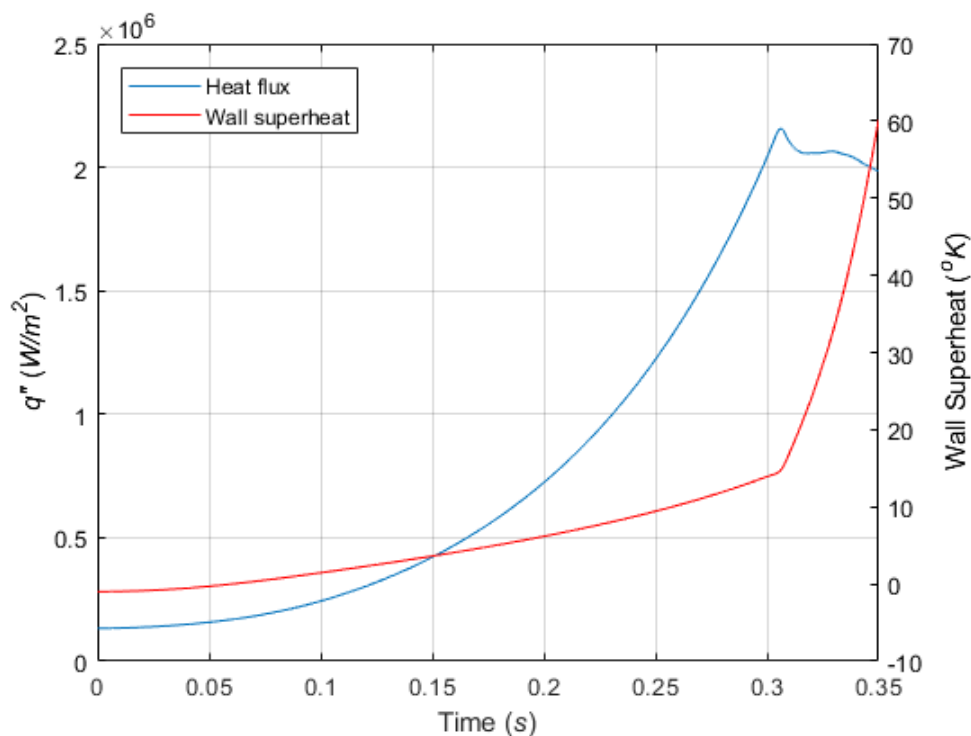
Fig. 65. Heating period of 100 *ms*: surface averaged temperature and heat flux

4.3.3   Boiling Pattern

From the vapor generating aspect, Fig. 66 and Fig. 67 provide the surface averaged vapor volume fraction for the EMP and VOF model, respectively. As discussion in previous section, the volume fraction in Fig. 67 proves that all the VOF simulations are remaining at the very beginning of nucleate boiling region. Even with the application of shortest heating period, the vapor volume fraction is about 0.18 which is far away from the vapor volume fraction that may induce CHF and transition boiling, however, this is not the case for EMP model. As shown in Fig. 66, the significant increasing of the vapor volume fraction on the heated surface provides a good view for the boiling with apparently different pattern against different heating period.
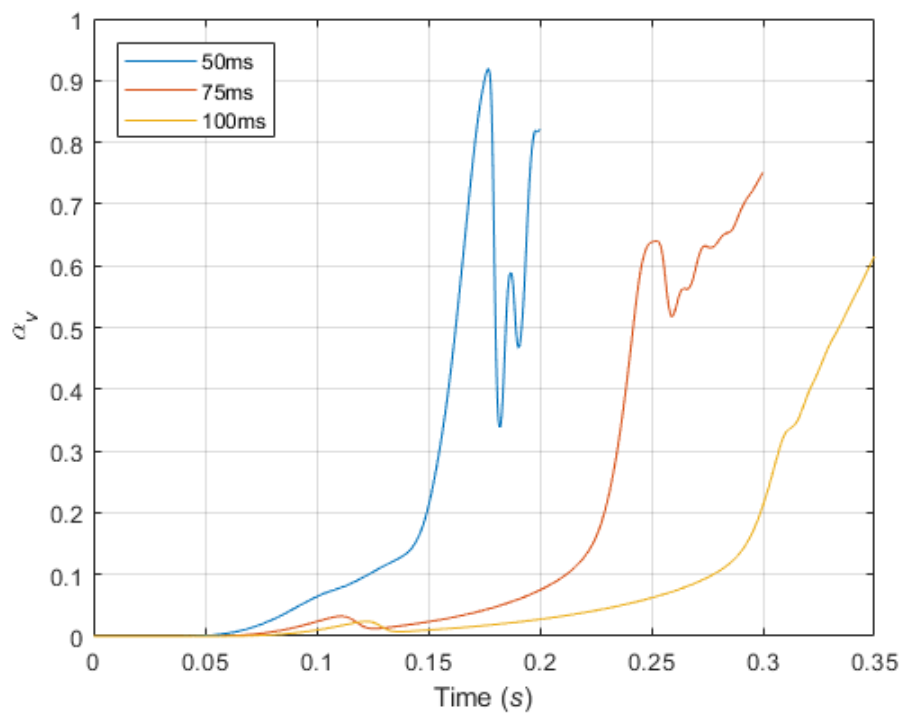
Fig. 66. EMP model: surface averaged vapor volume fraction against heating period
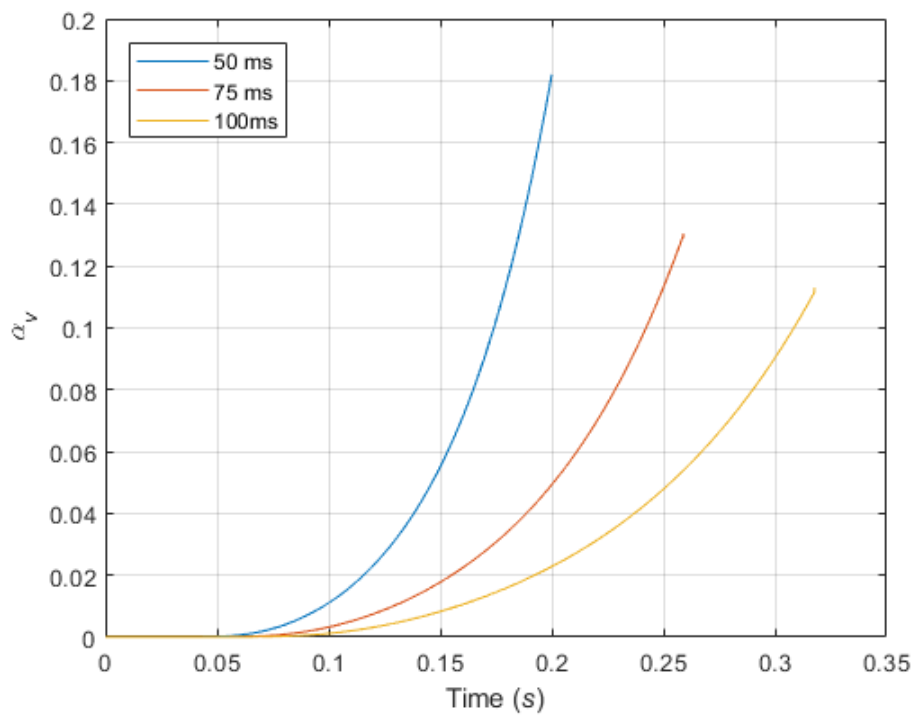
Fig. 67. VOF model: surface averaged vapor volume fraction against heating period

Fig. 68 is the vapor generating curve and its corresponding heat flux for the heating period of 50 *ms* case. It is clearly that the first peak of the heat flux is due to the fast accumulation of vapor on the heated surface. The instantaneous vapor generation starts at the physical time about 0.15 *s*. This fast vapor accumulating reaches the highest value of more than 0.9 at the physical time about 0.175 *s*. With such vapor accumulating, the heat flux decreases at the vapor volume fraction around 0.5 and reaches the lowest point when the vapor volume fraction shows the highest value. It should be noticed that all the vapor volume fraction and surface heat flux discussed in this study are the surface averaged value. This indicates that the vapor volume fraction is not necessary to be more than 0.8 (a typical standard of vapor volume fraction that may cause local film boiling) for CHF to occur. In addition, these surface averaged values provide a good view of a significant different boiling pattern for the case with short heating period. Fig. 69 and Fig. 70 are the surface averaged vapor volume fraction for the heating period of 75 *ms* and 100 *ms*, respectively. In both cases, the vapor volume fraction for CHF are located at a lower value, which are 0.5 to 0.7 for 75 *ms* case and 0.4 to 0.6 for 100 *ms* case, compared to the simulation with shortest heating period. Such fact indicates that, for the relatively longer heat period, the boiling crisis is preferred to be occurred more locally. In the case with heating period of 50 *ms*, this local boiling crisis is apparently not the case. The extremely high vapor volume fraction for the first peak in the heat flux curve represents that, instead of reaching a boiling crisis locally, the local boiling occurred among all the heated surface almost at same time. Followed by this type of global boiling, the vapor volume fraction rises again and reaches the CHF and transition boiling region. The vapor volume fraction for the "second" boiling in short heating period case shows an oscillatory value between 0.3 and 0.8. This may indicate that the boiling location on the heated surface are randomly and changing dramatically.
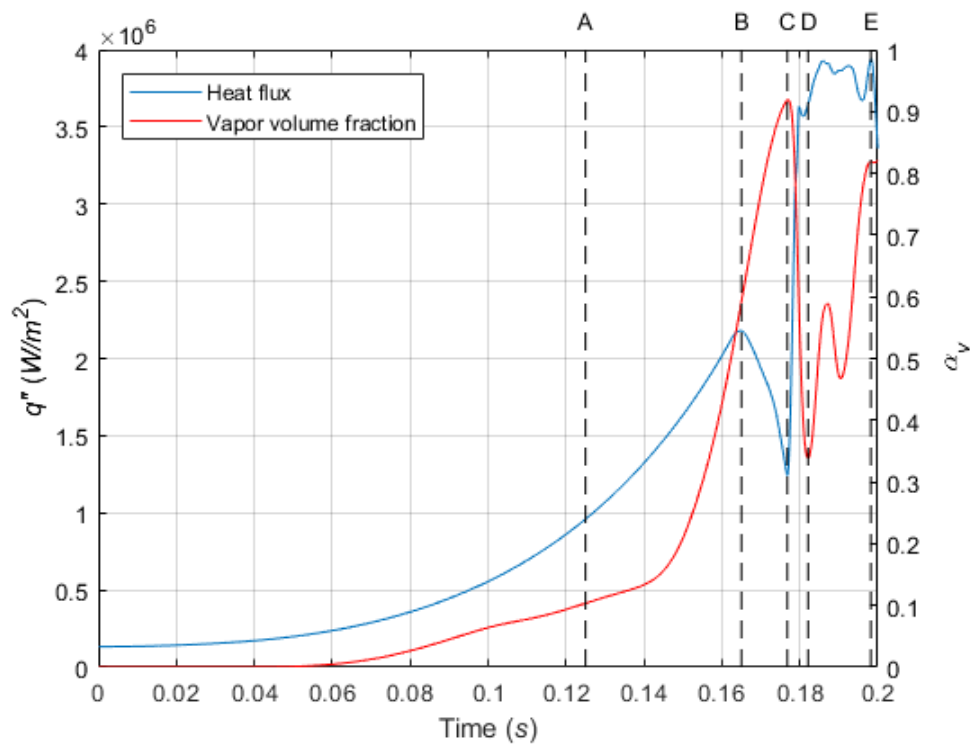
Fig. 68. Heating period of 50 *ms*: surface averaged volume fraction and heat flux
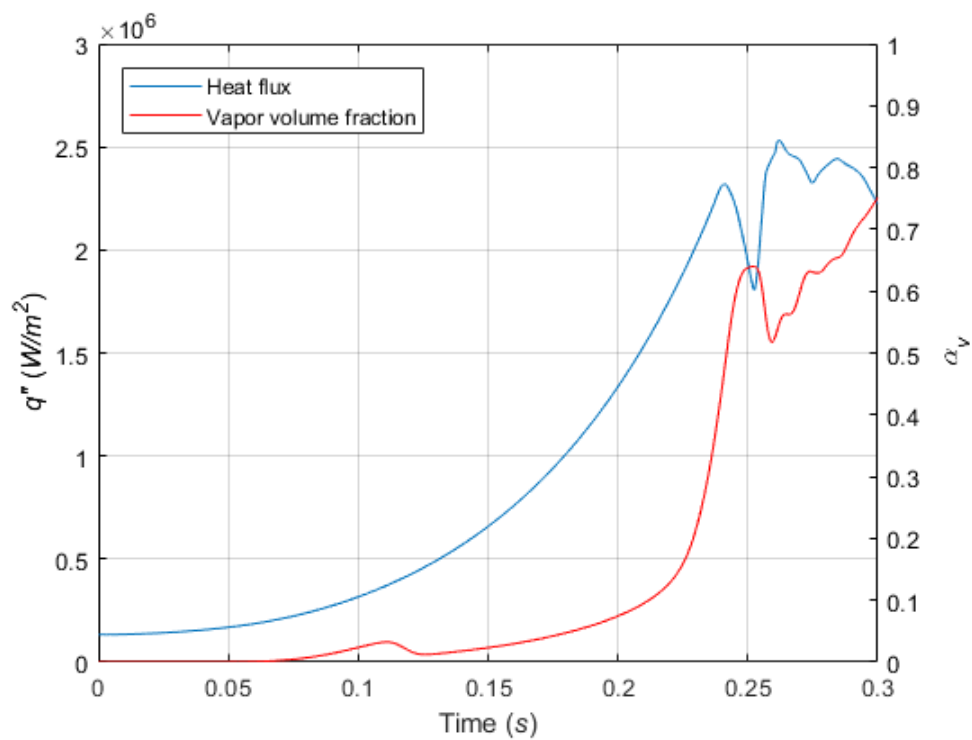
Fig. 69. Heating period of 75 *ms*: surface averaged volume fraction and heat flux
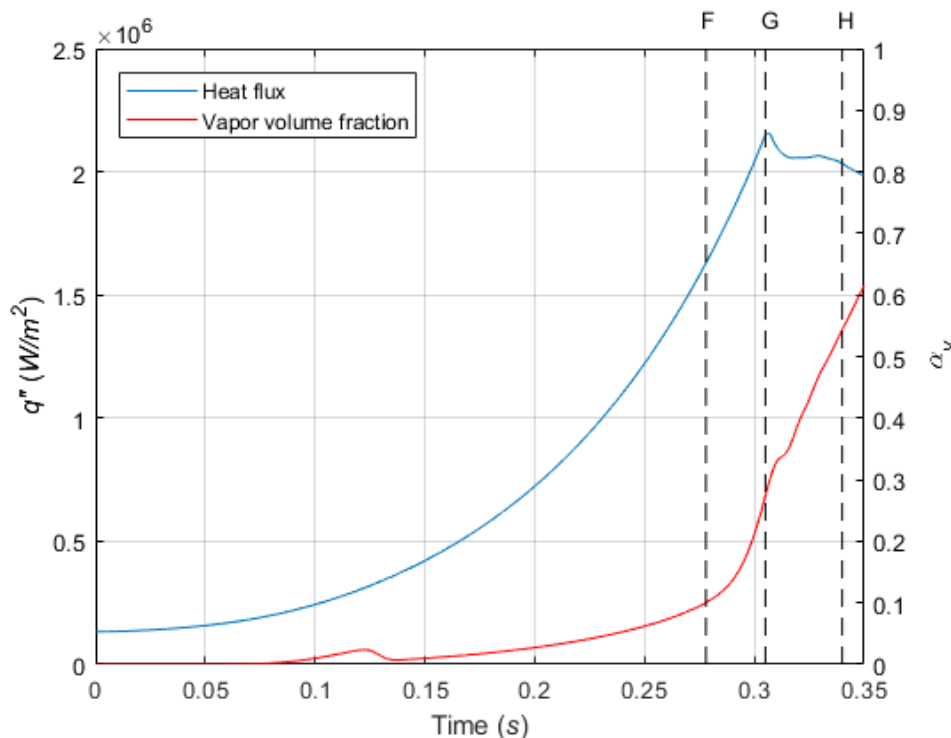
Fig. 70. Heating period of 100 *ms*: surface averaged volume fraction and heat flux

For the benchmark of above-mentioned mechanism, the videos for vapor volume fraction are recorded for the EMP simulations. For EMP simulation with short heating period, Fig. 71 to Fig. 75 are the boiling process corresponding to time *A* to *E* which is given in Fig. 68. The time *A* with low vapor volume fraction of 0.1 can be considered as the incipience of the boiling. As shown in Fig. 71, the boiling starts from the end of the heated surface with a significant increasing of vapor volume fraction. Followed by the incipient boiling, the maximum heat flux of the first peak is introduced at time *B*. As shown in Fig. 72, the vapor volume fraction increases smoothly on the entire heated surface in an extremely short period of 40 *ms*. Even though some of the surface area remain in a relative low vapor volume fraction level about 0.4, the surface averaged heat flux indicates that the heat transfer behavior for entire heated surface is already weakened by the local boiling crisis. After the first boiling crisis is occurred, the vapor keeps growing along entire heated surface until the heat flux drops to the lowest value at the time *C*. In Fig. 73, the extreme low vapor volume fraction (less than 0.01) in the water bulk region indicates that, for some reason, almost no vapor detaches from the heated surface at this moment. Due to the complication of the interphase momentum transfer and wall boiling model, it is challenging

to determine the true reason that cause such vapor accumulation without detaching. Nevertheless, as shown in Fig. 74, the increasing of the vapor volume fraction in water bulk region provides a good view of all the vapor detaches from the heated surface almost at same time. The low vapor volume fraction of the heated surface indicates that almost no vapor remains on the heated surface. After the end of the first boiling crisis, the vapor volume fraction starts increasing again until CHF is reached at time E. During the period between the time D and E, the heat flux curve oscillates heavily. The recorded boiling process shows that the reason for the oscillatory heat flux is due to the significant vapor films slide along the heated surface accompanying with the dramatically changing of the local boiling crisis. An interesting point for the above-mentioned process is that the "second" boiling starts from the beginning of the heated surface instead of the end of the heated surface which is the location of the "first" boiling took place. This pattern of the "second" boiling is also observed in the other two benchmark simulation.

Fig. 71. Time A: incipience of the boiling
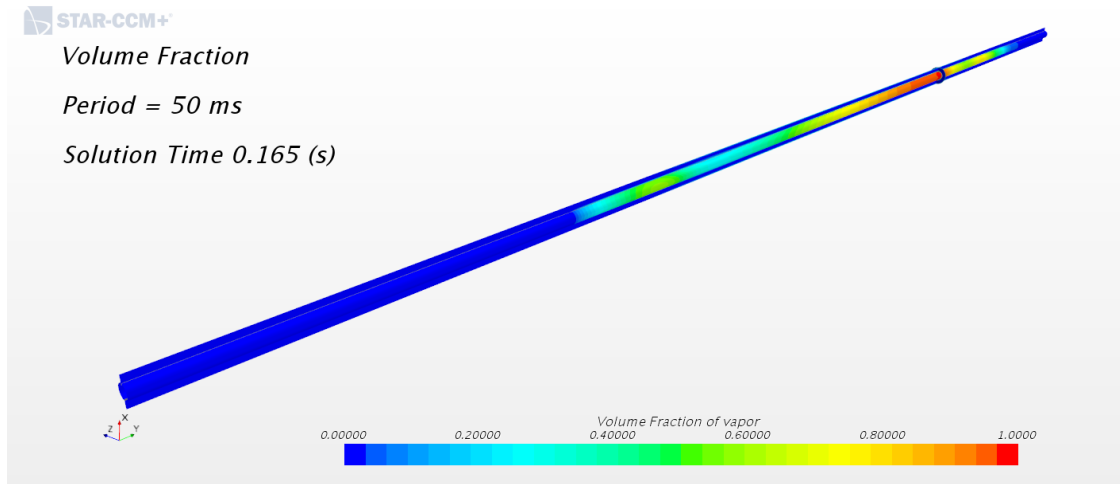
Fig. 72. Time *B*: boiling at the first peak of heat flux
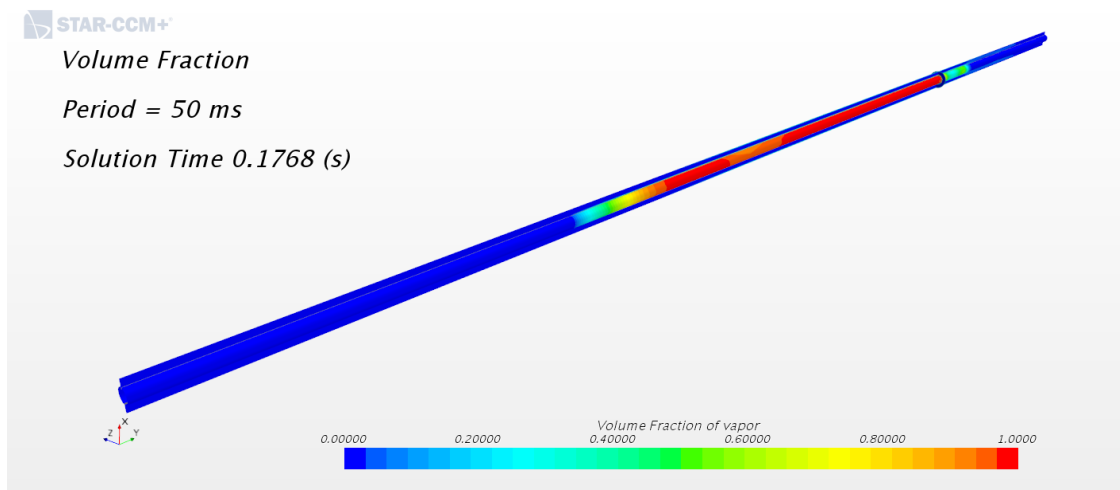
Fig. 73. Time *C*: boiling at the end of the first peak of heat flux
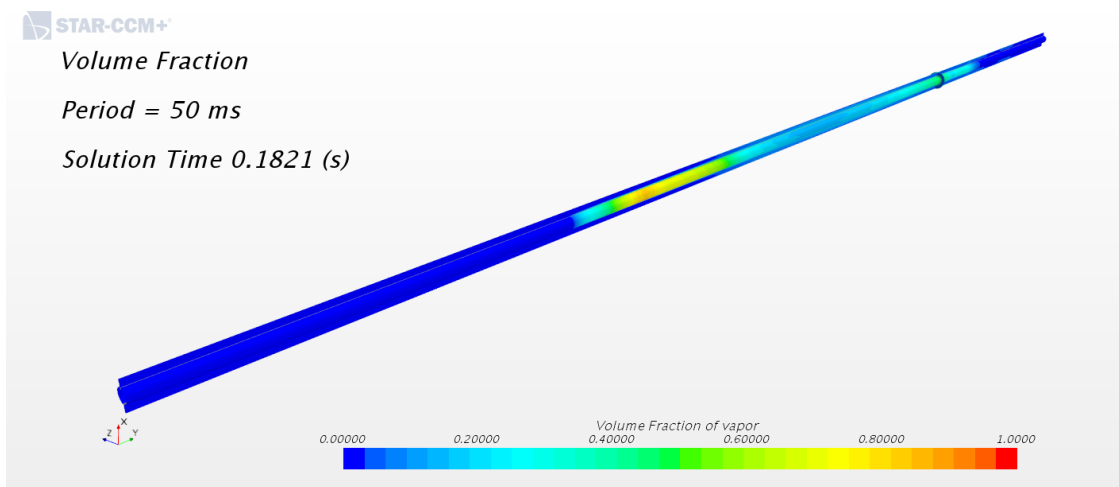
Fig. 74. Time *D*: boiling after the first boiling crisis
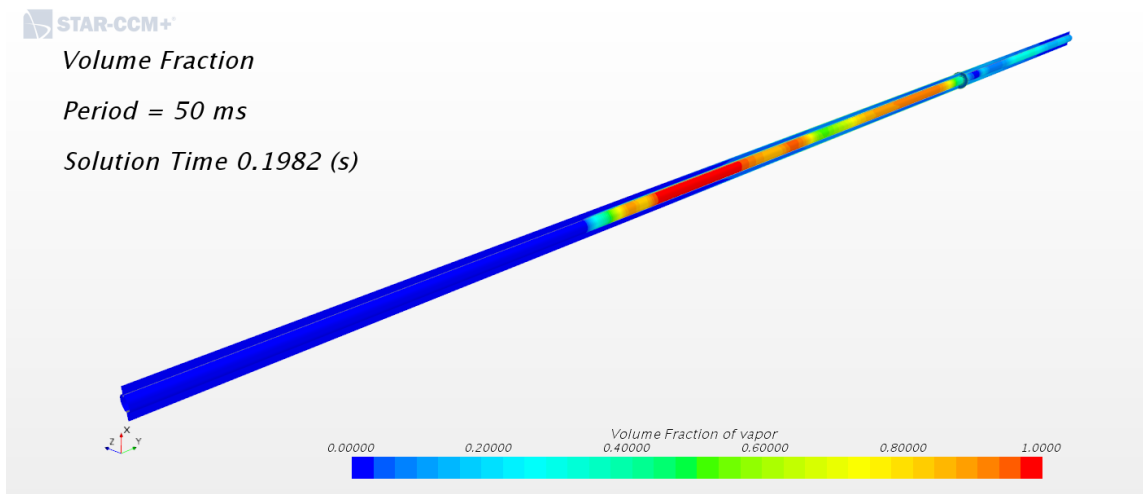
Fig. 75. Time *E*: boiling at the CHF

For the long heating period cases, the case with 100 *ms* heating period is taking as an example. Fig. 76 to Fig. 78 correspond to time *F* to *H* in Fig. 70. In Fig. 76, the incipient boiling takes place at the beginning of the heated surface which is different from the observation from the short heating period case. Furthermore, this pattern is also observed from the "second" boiling in the short heating period case. In this case, the CHF is reached around 0.305 *s*. The period between incipience of the boiling and CHF is about 0.227 s which is relatively longer than the observation from the first peak in the short heating period case (about 0.04s). In Fig. 77, it is clearly that the boiling pattern is very different from the short heating period case since the boiling crisis happens very locally with the vapor volume fraction of only 0.2 for the surrounded heated surface. Fig. 78, again, indicates a different boiling pattern in the post CHF region. Instead of fast changing of boiling crisis location, the simulation with long heating period shows a smooth extension of boiling crisis from local to entire surface.
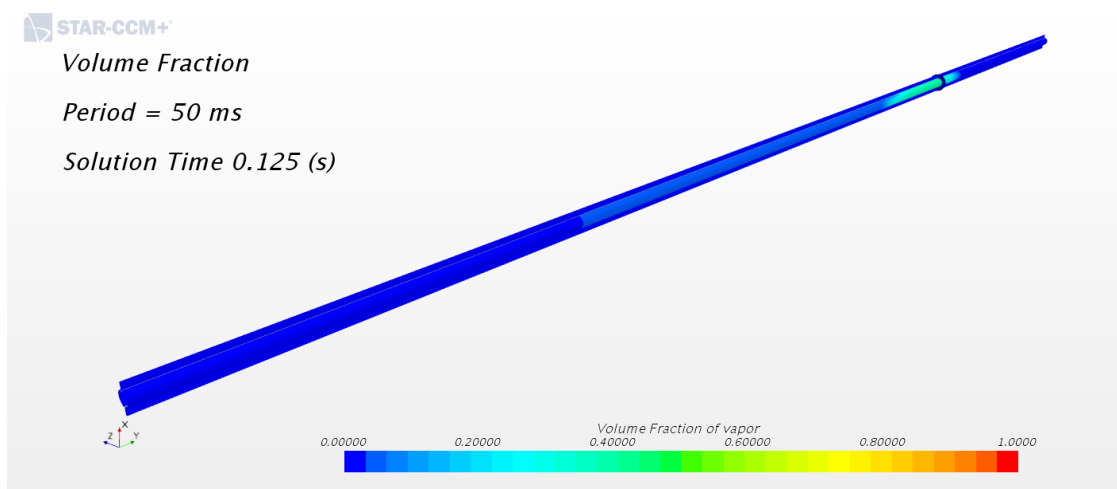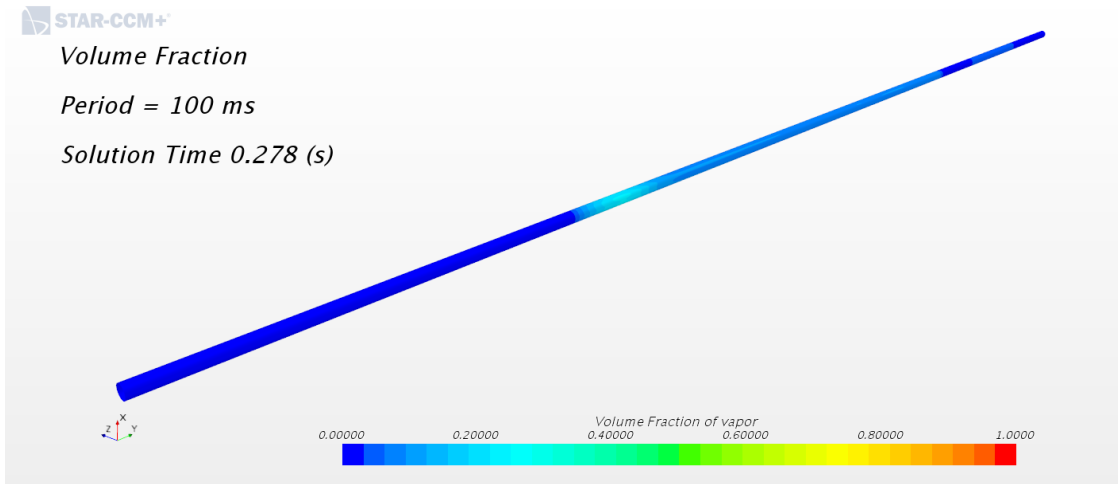
Fig. 76. Time *F*: incipience of the boiling
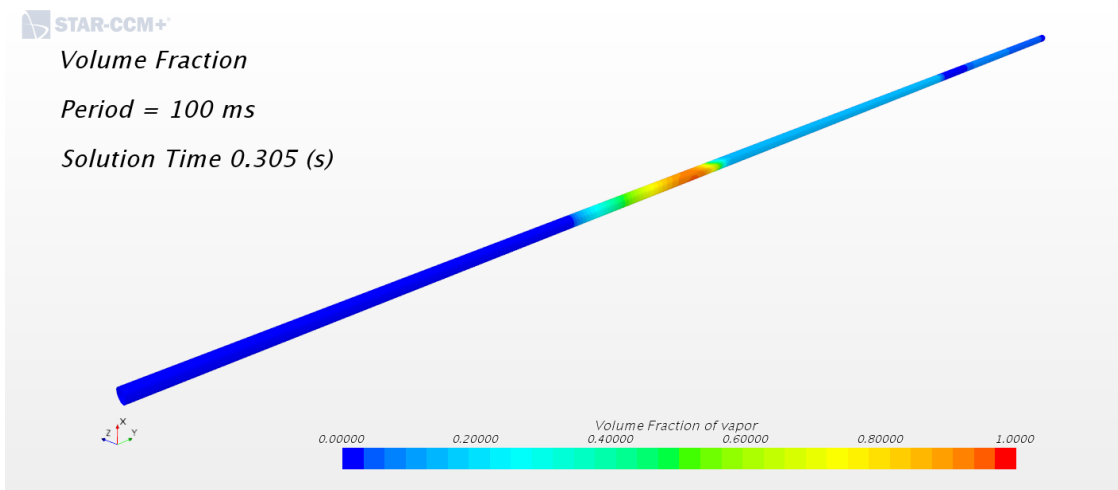
Fig. 77. Time *G*: boiling at the CHF
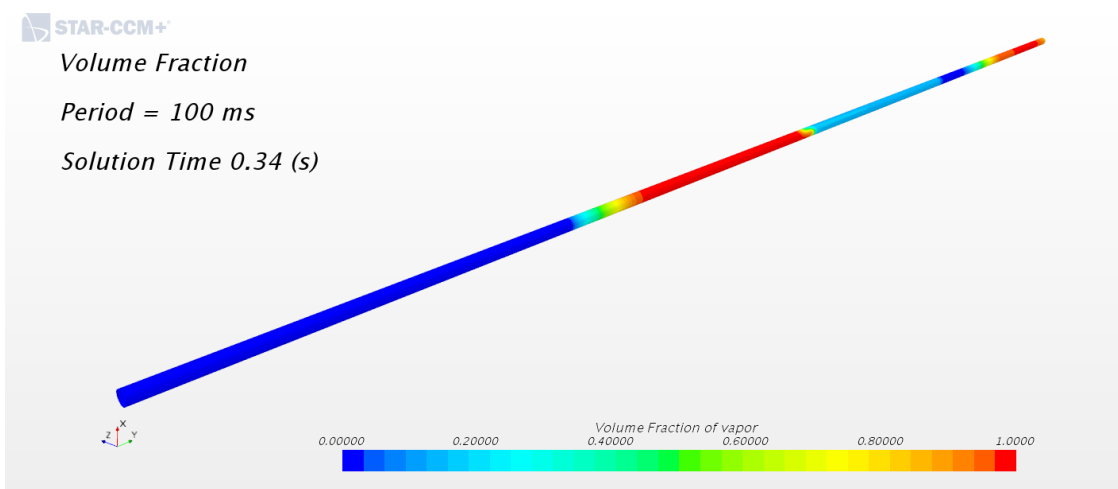
Fig. 78. Time *H*: boiling in the post CHF region

4.4   Benchmarking

The main purpose of this study is to provide a base line for studying RIA phenomenon by the using of CFD software. Yet, the validation of the simulating result is still a preference. Since this study is developed with the geometry from TRTL facility, the experimental data from TRTL facility becomes the first order of the data that selected for validation, However, during the time this study is developing, the TRTL facility is on the process of under construction. Even though, the experimental data from the TRTL facility is prepared for data validation, this study still trying to benchmark the simulating results from the past experimental studies by two aspects: the value of transient CHF and the irregular transient boiling patterns.

4.4.1   Critical Heat Flux

Recall that the CHF under transient scenario provides a higher value compared to quasi-steady state CHF. Thus, the CHF value from the quasi-steady state boiling may serve as a good reference to clip a reasonable value of CHF for this study. Table. 45 are some values for quasi-steady state CHF from different reference. (Groeneveld et al., 2007) is a look-up table for quasi-steady state CHF. In the look-up table, the liquid subcooling is defined by vapor quality instead of temperature directly. Due to the stability concern, the inlet flow in this study contains a very small amount of vapor (volume fraction of 1E-4). Thus, it is not suitable for translating the liquid subcooling directly to the vapor quality for the data benchmarked. Thus, for data benchmarked, a reasonable vapor quality is considered between -0.05 and 0.05. With the vapor quality, the CHF value of 2.2 and 3.3 MW/m^2 can be obtained from the look-up table under the condition of mass flux of 2500 and the pressure of 2030 psi. It should be noticed that it is not suitable to interpolate the CHF since the value in the look-up table may come from different reference. Another concern for the application is that the CHF value from the look-up table is obtained by applying the heat source on the pipe surface directly. This may lead to significantly heater geometry difference according to different wetted surface. For other experimental refernece, (Bessiron, 2007) provides a quasi-steady state test with the CHF value of 3.1 MW/m^2. Again, the value should be relatively higher compared to this study since both higher liquid subcolling and pressure are considered for the boundary conditions. Except the CHF value

under the experimental frame, other CFD study for quasi-steady state boiling may also a concern for the result benchmarked. Recall that the purpose of this study is to provide a new base line of boiling CFD study with the consideration of time and heater behavior. In other words, this study is served as an improvement of past CFD study which includes (Kim et al., 2016). Kim did a boiling CFD study by the using of steady state time model. The boundary heat flux is increased step by step manually on the pipe surface with 500 hundred inner iterations for convergence. Even though the temporal behavior is not included, the study still give a good reference for quasi-steady state boiling since the simulating results are validating with the 1958 ANL experimental CHF data from (Weatherhead &R.J., 1963). Under the boundary condition with pressure of 2000 *psi* and subcooling of 10 $°K$, about 2.0 MW/m^2 is obtained for the CHF. Though the boundary conditions are slightly different from this study, the value of CHF from the study still provide a good agreement for the CHF benchmarked in this study.

Table. 45. Reference for quasi-steady CHF

	Test metrics (psi / $°K$)	Flow condition (kg/m^2)	Heater type	$\tau(ms)$	CHF (MW/m^2)	Reference
Groeneveld (2007)	2031 / 0	2500	pipe	N/A	2.2~3.3	CHF look-up table
Bessiron (2007)	2117 / 60	3043	cladding	N/A	3.1	Experimental
Kim (2016)	2000 / 10:20:40	2650	pipe	N/A	2.0 (2000/10)	CFD
This study	2000 / ~5	2580	cladding	100	~2.1	CFD

Due to the concern of the safety and data collecting issues, the number of the studies that corresponding to transient boiling scenario is very limited during past decades. Table. 46 has summarized the test metrics for most of the transient boiling studies during past decades. As shown in Table. 46, the earlier studies tend to have an abnormally high value of CHF. For example, in (Rosenthal, 1957), the transient CHF is more than 3 MW/m^2 even with only the pressure of 1 *atm*. Since all these studies adopted different test metrics including: pressure, flow condition, liquid subcooling, heating period and heater geometry, it is difficult to determine a specific factor that causes an abnormally high value of the transient CHF. However, one of the very likely reason may be the heater geometry. In early studies, the ribbon heater is a very common heater type because a higher value of surface

heat flux can be easily reached with small amount of heat deposit in the heater itself. Nevertheless, the assumption of nearly no heat deposit in the heater may lead to a high uncertainty of the derived boundary heat flux and, thus, cause an unreasonably high value of the CHF. Among these studies, a similar test metric close to this study can be found in (Johnson, 1970). In Johnson's study, a large number of tests are done vie widely varied boundary conditions. Though the initial power output and the heater geometry are different form this study, the similar pressure, liquid subcooling, flow condition and heating period as this study can be found in the study. In the test, a value of about 8.52 MW/m^2 for transient CHF is observed under the same boundary conditions as this study. However, it should be noticed that the transient CHF value from the test is abnormally high even compared with the later study, (Bessiron, 2007), with similar boundary conditions. Furthermore, no OV is observed in any of the test from Johnson's study. With the above-mentioned concern, the most appropriate reference for the simulation benchmarked may lie to Bessiron's study. In the study, a series of test with pressure of 2100 psi and subcooling of around 60 $°K$ is done with the cladding shape heater. Even though the heating period is quantized as a FWHM of 30 ms, which is not suitable for comparison of the heating period from this study, the results still provide a good view of a reasonable transient CHF that should be observed in this study. With the current understanding of the transient CHF, typically, both higher pressure and liquid subcooling give a positive influence om the value of transient CHF. It is expected that a lower value of transient CHF should be obtained from the simulations compared to Bessiron's study due the lower pressure of 2000 psi and subcooling around 5 $°K$ are adopted as the boundary conditions for the simulations. With the fact, the transient CHF from Bessiron's study may serve as an upper limit to determine the reasonable value of the transient CHF for the simulations

Table. 46. Test metrics for past transient boiling studies

	Test metrics (psi / $°K$)	Flow condition (m/s)	Heater type	P_0 (W/m^2)	Heating period (ms)	CHF(MW/m^2)	OV
Rosenthal (1957)	14.7/0~68	Static	Ribbon	N/A	5~75	3.15~6.31 (14.7/33)	Yes
Hall&Harrison (1966)	14.7 0~80	Static	Ribbon	N/A	0.7~5	1~8 (14.7/0)	Yes
Tachibana(1967)	14.7/0	Static	Ribbon	1.16E+6	1.5~183 (ramp)	0.58~3.49	No
Sakurai (1977)	14.7 0~75	Static	Ribbon	N/A	4~1000	0.5~3 (14.7/0)	Yes
Johnson (1970)	14.7:500:1000:2000/ 0:5:23:62	<0.3:4.3	Ribbon	4.73E+4	5:15:50	8.517 (2000/5/4.3/5)	No
Sakurai (1977)	14.7~305/0	Static	Wire	4500	5~10000	5~13 (305/0)	Yes
Kataoka (1983)	14.7~305/0~70	1.35~4	Wire	4500	5~10000	5~10 (20.7/20/4)	Yes
Bessiron (2007	14.7:2117:2248/60	4	Cladding	N/A	30 (FWHM)	4.3 (2117/60/4)	N/A
Park (2009)	14.7~218/0~160	Static	Wire	N/A	5~50000	1~2 (14.7/0)	Yes
Su (2016)	14.7/10:25:75	0.75~2	Chip	N/A	5~500	Halted before CHF	Yes
This study	2000 ~5	4	Cladding	5.49E+5	50:75:100	3.6~3.8 (2000/4/4/75)	Yes

In a short summary, the quasi-steady state CHF from past study provides a good benchmarked standard for the simulation with relatively long heating period. Both the experimental and simulating study give an acceptable error which is less than 30 percent. However, for the transient scenario, the results from the past provide a high variance due to the different test metrics and complicated mechanism behind the boiling. Thus, it is challenging to determine a specific value of transient CHF for data validating. Still, Bessiron's study (2007) provides a decent reference for the data validating. With the upper limit of CHF given by Bessiron's study and lower limit from Table. 45. The statement that a reasonable transient CHF can be predicted by this study using the CFD software of Star-CCM+ can be made.

4.4.2   Boiling Pattern

With different test metrics from past empirical application, it is challenging to benchmark the boiling pattern under transient scenario, however, it is possible to examine the rationality by comparing boiling curves between studies. Fig. 79 and Fig. 80 are the boiling curves of wall temperature against time behavior from (Rosenthal, 1957) and (A.Sakurai &Shiotsu, 1977), respectively. Since the value of CHF is benchmarked by Bessiron's study (2007), it is a preference to compare the boiling curve from the simulation to Bessiron's. However, due to highly scattered and the ambiguity of the data, the above-mentioned two studies become a decent choice since clearer boiling curves are provided. Fig. 81 is the boiling curve with 50 ms heating period from the simulation. It is clear that a similar boiling pattern is revealed with the appearance of OV. By the definition of OV from Sakurai's study (1977), the difference between the peak value of wall temperature and saturated temperature of the coolant, a OV of about 40 $°K$ is both revealed in Fig. 79 and Fig. 80. However, it should be noticed that the physics behind the OV in this study is obviously different from the conclusion in the past. By comparison of heat flux and wall temperature curves in Fig. 81, the increasing of the wall superheat indicates that the OV is led by the fast increasing of vapor volume fraction from the heated surface. However, this is obviously not the case for the past studies. It is clearly shown in Fig. 80 that a significant increasing of the heat flux is introduced during the period that OV happens. Such thermal

hydraulic behavior is attributed to the delayed response of the convection from the coolant in the early studies, for example, Rosehthal (1957). In addition, the sudden drop of the wall temperature that happened after the OV is considered as a response of the delayed incipience of boiling. Under the hypothesis, the surface heat flux build-up due to the exponential type increasing of the heater power is relatively faster than the response of boiling in the coolant. Since the phase change of the coolant provides an additional heat removal from the heater, the wall temperature thus drops after the delayed incipience of boiling.
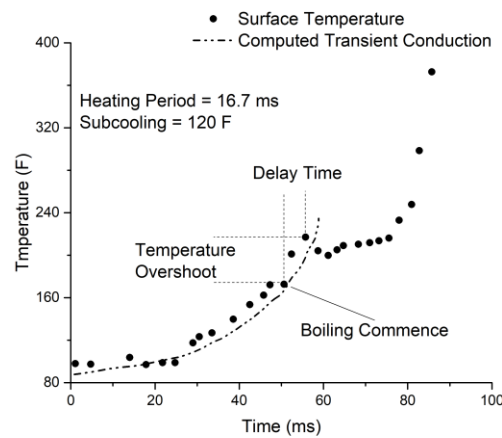
Fig. 79. Boililng curve of wall temperature [Rosentahl]
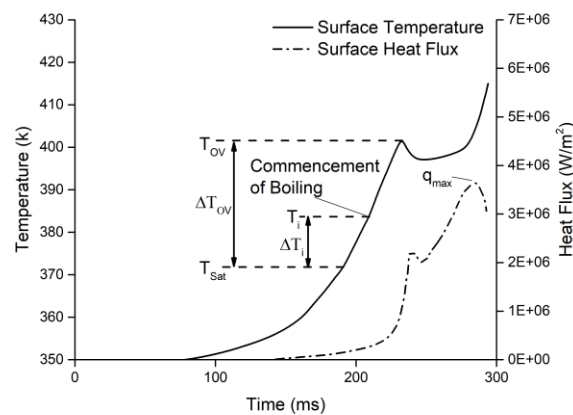
Fig. 80. Boiling curves of heat flux and wall temperature [Sakurai]
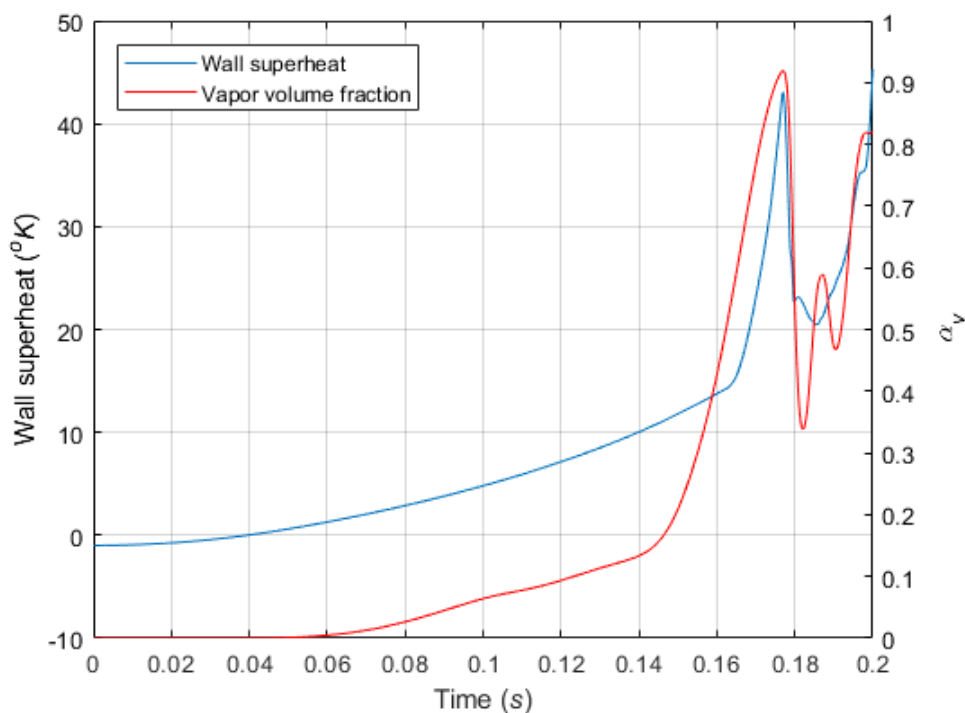
Fig. 81. Boiling curves of wall superheat and vapor volume fraction

The above-mentioned hypothesis is, however, argued by the later studies from both (Tachibana et al., 1968) and Sakurai's study (1977). In both studies, the incipience of the boiling is observed to be occurred before the OV reaches its peak value. Following is the observation from Tachibana's study (1968):

Though the clearly discernible inflection seen in the temperature curve for the 0.01 *mm* thick test section might appear to suggest abrupt nucleation over the whole surface, photographic records reveal that the first bubble has actually appeared appreciably earlier than this infection point. (Tachibana et al., 1968)

Fig. 80 from Sakurai (1977) shows a clear view that the earlier incipience of the boiling during the OV. If this is the case, the delayed of the boiling is no longer suitable for explaining the physics behind the OV. Nevertheless, the mechanism behind the temperature OV remains unknown since none of the later studies provide the detail of the examination of the temperature behavior. The observed difference between this CFD study

and past experimental application can be further detailed by the boiling curve with the heat flux and its corresponding wall temperature. Fig. 82 are the different types of the transient boiling which summarized by (Serizawa, 1983). The type *A* boiling corresponding to those transient cases with relatively longer heating period. During the surface heat flux build-up, the transient boiling curve tends to attach the extended steady state boiling curve when high heat flux is approaching. The type *C* is characterized by the short heating period cases with no attaching on the extended steady state boiling curve even when CHF is reached. At same time, the type *B* of boiling is served as the transition case between type *A* and type *C*. It should be noticed that the type *D* is not detailed anywhere in Serizawa's study (1983) and no reference can be found from past studies. In this study, Fig. 83, Fig. 84 and Fig. 85 are the boiling curves corresponds to the heating period of 50 *ms*. 75 *ms* and 100 *ms*, respectively. Recall that the VOF simulation is not suitable for predicting the transient boiling. However, since Rohsenow's correlation is adopted as the boiling model for VOF simulations and is commonly used for developing the steady state boiling curve in past studies, VOF simulations is useful and can serve as a good reference for extended steady state boiling curve from the CFD aspect.
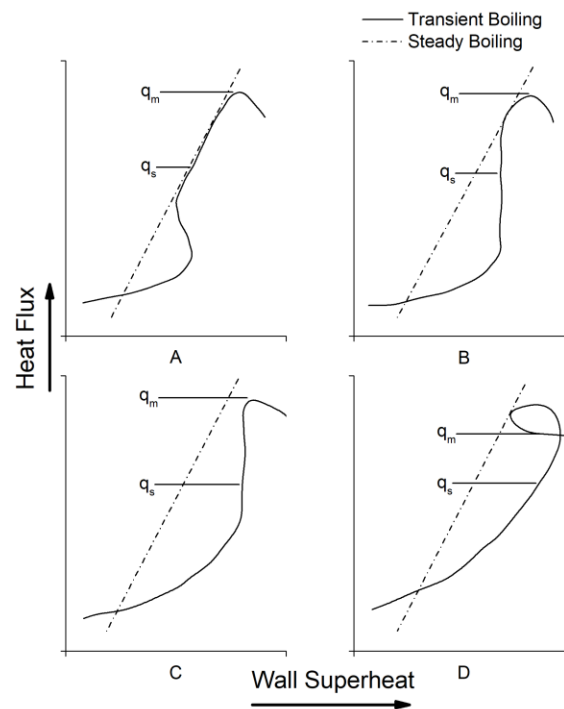
Fig. 82. Different types of transient boiling [Serizawa]
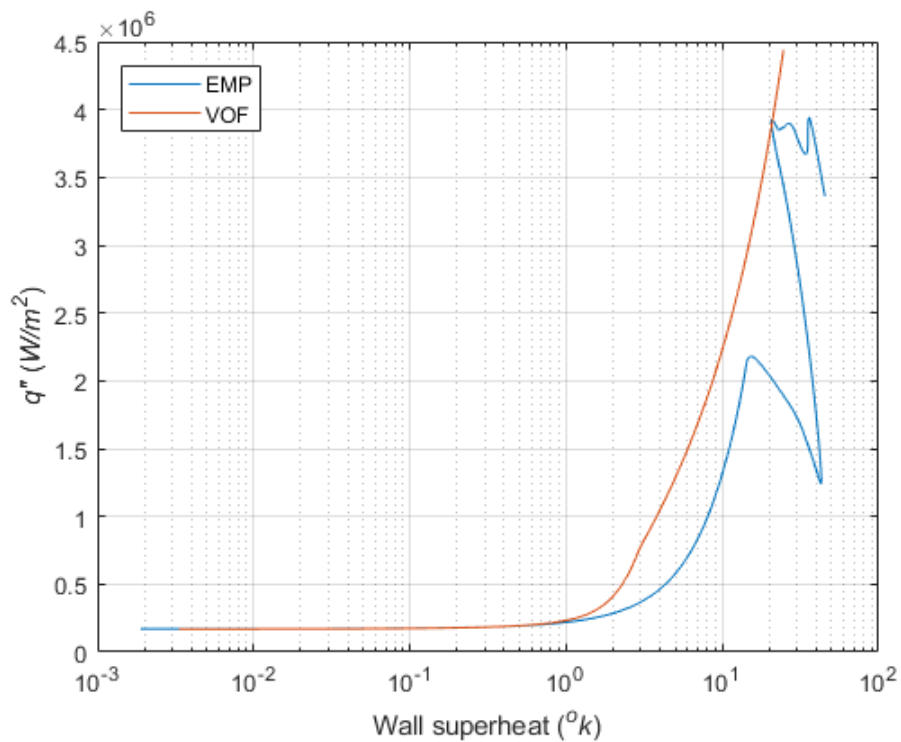
Fig. 83. Boiling curves of 50 *ms* heating period for EMP and VOF model
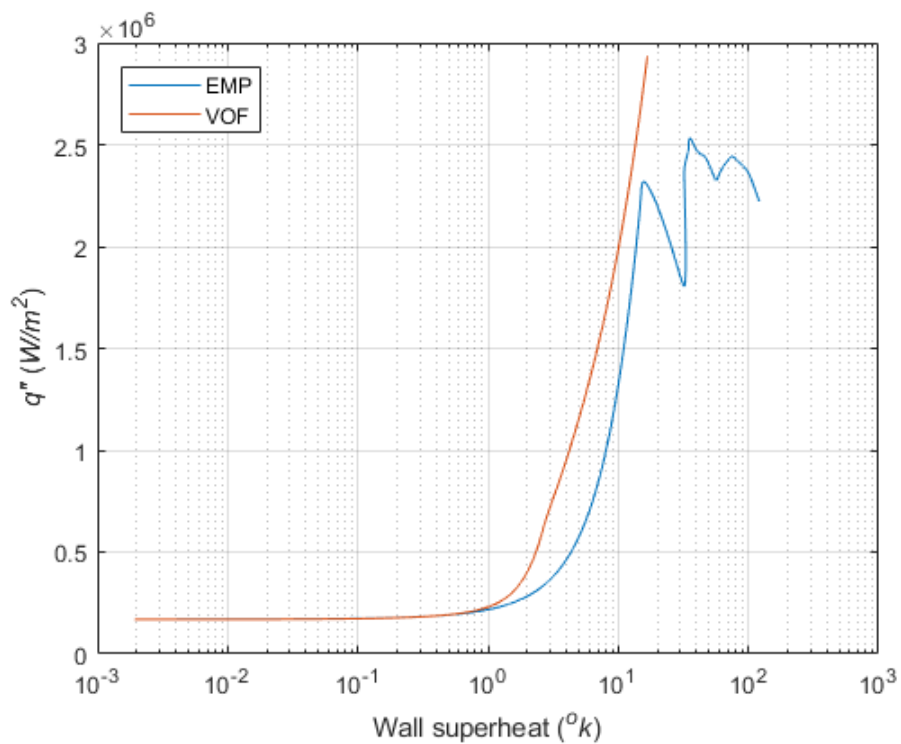
Fig. 84. Boiling curves of 75 *ms* heating period for EMP and VOF model
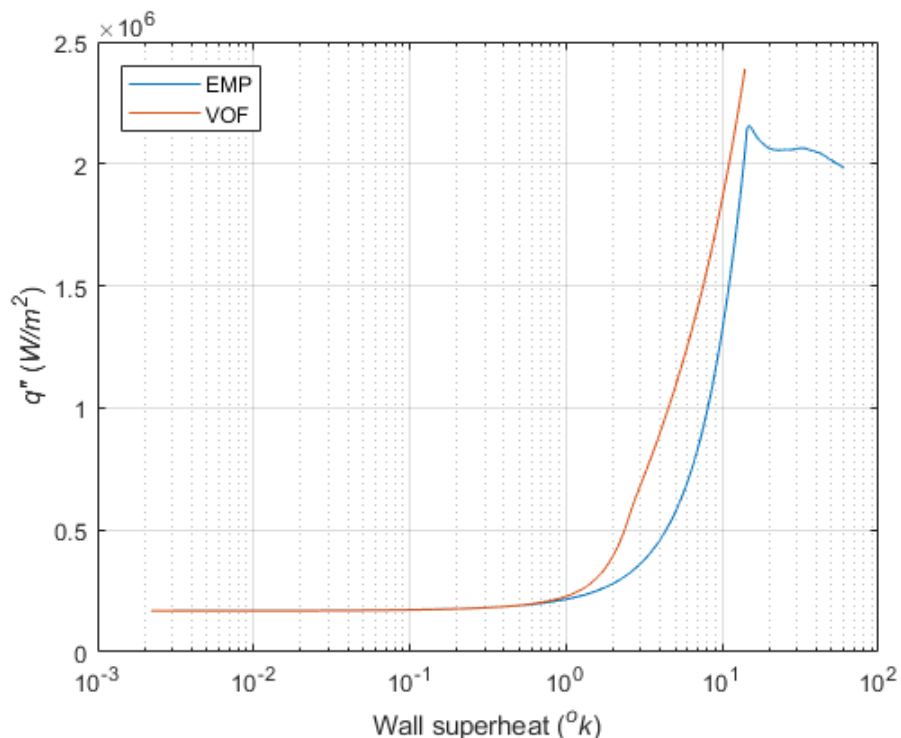
Fig. 85. Boiling curves of 100 *ms* heating period for EMP and VOF model

From the figures, it is clearly that all the simulations in this study can be related to the type *C* boiling. Even though type *C* is revealed only with extremely short heating period, it is reasonable for simulations to be predicted for two reasons:

- The heat deposit in the heater plays a crucial role for determining the wall temperature. Due to the larger heater compared to past studies, the significant effect of the heat deposition may lead to a higher wall temperature and, thus, forces the transient boiling curve shift away from the extended steady state boiling curve when the phase change is not enough to remove the heat from the heater.

- For the quasi-steady state boiling, the heating period is concerned to be more than 10 *s* according to past studies. Meanwhile, the longest heating period in this study is considered to be 100 *ms* which is two orders of magnitude smaller than the quasi-steady state boiling that mentioned in the past. Furthermore, unlike the experimental application, CFD simulations provide no delay from the instruments for both power output and data collecting.

Though the type *C* boiling pattern seems to be revealed in this study, several differences between Fig. 82 and Fig. 83 is significant and should not be ignored. First, a non-CHF peak (first peak shown on the heat flux curve) led by the significant decreasing of the surface heat flux is observed before the CHF peak. Recall that the physics behind this peak is the fast increasing of the vapor volume fraction on the heated surface. The explosive increasing of the vapor volume fraction on the surface is considered way faster than the bubble detaching cycle. Thus, a film-like vapor on the surface may cause the deterioration of the surface heat transfer. Different from the traditional understand of film boiling, the influence of heat transfer capability from this film-like vapor is only temporarily. For some reason, the film-like vapor detaches from the surface and the heat transfer capability is again improved by the rewetting. In the fact, this phenomenon is observed and mentioned by several past studies. Following is the description of the event from Rosenthal's study:

There was an almost explosive formation of bubbles, and the ribbon temperature decreased. This boiling surge expired, and a moment the surface was nearly free of bubbles. Then, boiling commenced which was similar in appearance to local boiling with steady generation of heat. (Rosenthal, 1957)

It should be noticed that the above-mentioned "temperature decreased" is considered as the temperature drop after the OV and caused by the delayed incipience of the boiling. However, it is confirmed by the later studies that the incipience of the boiling is introduced during the OV instead of the peak. This may indicate the time line for the event may be inaccurate though the event is recorded. In (Tachibana et al., 1968), a more detailed description of the event is provided. Following is the description:

The mechanisms that cause a high heat flux may be the rapid formation and evaporation of thin liquid film at the base of vapor bubbles. The rapid evaporation of liquid film, however, gives rise to the appearance of dryout areas, where the cooling ability sharply drops below the level of the wetted area. Thereupon, it is considered that the dryout area rapidly increases and makes the heat flux decline again after a peak point, bringing about a rapid rise of temperature. All the bubbles on the surface are still in the phase of the first

generation when the critical condition is reached. This is the case when the transient critical heat flux is very close to the steady rate. (Tachibana et al., 1968)

Fig. 86 is the boiling curves from Tachibana (1968). Even though the increasing of the peak value for non-CHF peak is not shown, it is clearly that a very similar pattern compared to the non-CHF peak from the simulations is appeared. That is, with the decreasing of the heating period, the decreasing of the surface heat flux tends to be significant. This trend also revealed in the simulation, for example, in the simulation with the heating period of 50 *ms*.
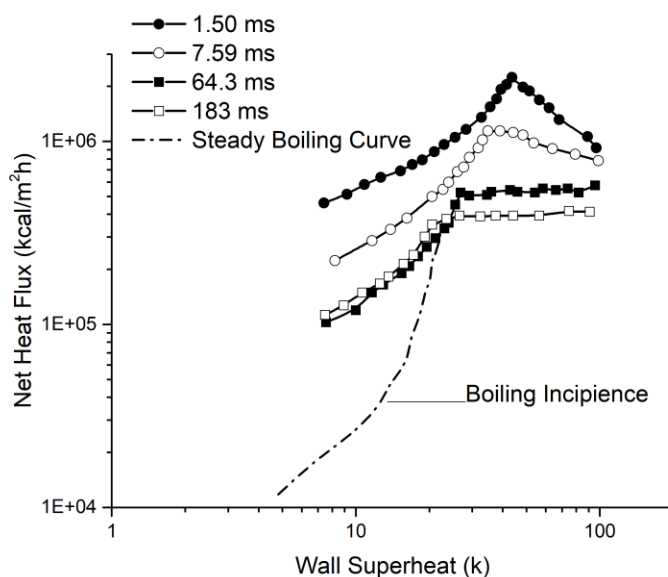
Fig. 86. Boiling curves for different heating period [Tachibana]

To explain the explosive formation of the film-like vapor, (Bessiron, Sugiyama, &Fuketa, 2007) provides a new hypothesis that is very similar to HSN mechanism, as shown in Fig. 87. The sudden increasing of the vapor volume fraction on the surface is led by the explosive increasing of the nucleation number site density due to the fast increasing of the wall temperature. The fast increasing of the nucleate sites forces the bubbles coalesce and forms a vapor film before the bubbles detaches from the surface. According to the hypothesis, this process may repeat several cycles before a steady vapor film is formed and, thus, leads to a higher value of CHF compared to the quasi-steady state boiling.

Quasi-stationary increase of clad temperature

Boiling crisis

Activation of a
limited number
of nucleate sites
according to
cavity radius.

Growth / detachment of
series of bubbles

Formation of
vapor columns

Instability of
vapor columns

Film boiling

Fast increase of clad temperature

Boiling crisis

Activation of a
considerable number
of nucleate sites.

Enhancement of heat flux due to
latent heat absorption + possibility
of several nucleation / departure
cycles in a steep fluid temperature
gradient

Coalescence of
bubbles

Film boiling

Fig. 87. Different heating pattern respect to the heating rate [Bessiron]

However, as the second difference that mentioned before, between Fig. 82 and Fig. 83, the simulating result shows a connection between transient boiling curve and quasi-steady state boiling curve. This may indicate that the boiling after the non-CHF peak is more similar to the quasi-steady state boiling instead of a HSN-similar mechanism. According to the simulations, a better explanation of the higher CHF value may stand for the global rewetting after the first-generation film-like vapor detachment. The rewetting with almost no bubbles remains on the surface provides an additional period for surface heat flux to build-up again during the bubble growth after the HSN-similar mechanism. Furthermore, the decreasing of the wall temperature is very likely to transfer the boiling pattern from the HSN-similar mechanism to the traditional HI mechanism and, thus, cause a quasi-steady state boiling pattern and the attachment of the extended steady state boiling curve.

With the boiling pattern benchmarked between CFD simulations and past experimental studies, the simulations may indicate that the non-CHF peak shares an extremely similar

physics with the HSN. It is believed by the author that the non-CHF may directly related to the HSN or, at least, based on the same physical mechanism for the following reasons:

First, the lower peak value compared to the experiment-recorded transient CHF is observed from the simulations. In (ASakurai et al., 1993), it is indicated that with the decreasing of the heating period, a CHF value that close to the quasi-steady state boiling or even lower is observed under the frame of the HSN phenomenon. In this study, the peak value of non-CHF peak shows the same behavior as from Sakurai's observation.

Second, the boiling curves from the simulations provide the same trend as provided by HSN mechanism. Recall that, in (Shiotsu et al., 1990), a directly transition from nucleate boiling to film boiling is observed under the frame of the HSN mechanism. A deterioration of the heat transfer between heated surface and coolant leads to the sudden drop of the surface heat flux. The same directly infection point as in (ASakurai et al., 1993) is also revealed with the non-CHF peak in this study. This is also the case for Tachibana (1968), however, it should be noticed that Tachibana's study is the only study that reveals this kind of boiling curve in the early stage. The reason why this kind of boiling curve is not recorded remains unknown. Yet, a very likely reason may stand for the derivation of surface heat flux. Different from the numerical method of finite volume discretization that adopted by CFD code, in most of the past studies, the surface heat flux is derived analytically as the global behavior according to temperature only. The difference between numerical and analytical method may lead to the neglecting of the heating process.

Third, even though no boiling curves from the past studies provides a clear view of HSN, the description of the sudden explosive vapor generation shares a similar characteristic with HSN. In this study, the burst of the vapor generation is clearly revealed with the same process that discussed in the past studies and HSN mechanism. Furthermore, the hypothesis provided by Bessiron (2007), typically shares the same description of the event with the HSN mechanism, however, the physics behind them may be slightly different. Since the heater geometry plays an important role on surface temperature, one would be noticed that the HSN provided by (ASakurai, 2000) is based on the wire heater which is considered to

have a smaller effect for heat deposition in the heater itself. In this case, the pre-pressurized step that mentioned in (ASakurai et al., 1993) and the extremely small heater surface (wire) may serve as an important role to force the occurrence of HSN mechanism. It is expected that the flooded cavities delay the incipient boiling and, thus, increase the heat deposition in the heater. Combing with the wire heater, the nucleate bubbles is very likely to crowd with each other even with the small bubble diameter and lead to the directly transition of the film boiling.

Fourth, in Sakurai's studies, all the boiling curves related to the HSN mechanism end after the sudden drop of the surface heat flux. Though the reason for the termination of the curves is not indicated, it is very likely that the experiments are postponed in order to prevent the heater from burnout, this is also the common reason for several past studies. If this is true, the simulations possibly provide an integral process of transient boiling. That is, HSN mechanism may serve as only partial of the transient boiling process. Moreover, the following boiling pattern after the non-CHF peak may successfully explain why a higher CHF can be achieved under the transient scenario.

With the above discussion, a new hypothesis that successfully combines HSN mechanism and traditional transient boiling can be issued. Under the fast-transient scenario, the HSN mechanism is very likely to be introduced with the sudden vapor crowded on the heated surface, especially, with fast increasing surface temperature led by the significant effect of heat deposition (This may not be the situation for Sakurai's studies). Followed by the occurrence of the HSN phenomenon, for some cases, there exists a possibility that the film-like vapor may detach and causes a period with almost no vapor on the heated surface. A higher transient CHF as traditional mechanism can be achieved by the HI mechansim which is caused by the rewetting on the heated surface. It should be noticed that, however, the above-mentioned hypothesis is only based on the observations from the CFD simulations and the results provided in the past studies. More experimental application and careful discussion is necessary for the confirmation of the speculation.

5   CONCLUSION

This study provides a new approach for studying transient boiling using the CFD software package of Star-CCM+. The main purpose is to test if the CFD software has the capability to simulate the CHF under the frame of the power transient. With the transient time model and CHF method, the temporal and heater behavior which used to be overlooked in the past now can be taken into account for reconstructing of the transient boiling curves.

The adopted models and their reference are discussed in this study. Due to the computational cost and stability issues which are very common problems for CFD studies, the choices of the models are limited. However, the prediction of transient CHF and its corresponding transient boiling pattern provide a reasonable result compared to available past studies.

To conquer the significant issues which is accompanied by the fast-transient physics, this study provides a complete view of the stability issues and their corresponding solutions. The convergence and grid independent studies are also provided for the precursor and following transient simulations (with constant power output). The methods that used for both studies are provided and discussed.

The observed transient boiling process is discussed from different aspects, including heat flux, heater surface temperature and the boiling pattern. These results are also benchmarked with the available past experimental studies. Furthermore, a new hypothesis of power transient boing is postulated based on the simulation observation and past experimental studies.

5.1   Observations

The stability is the key which leads to the success of those CFD studies under a transient scenario. Due to the using of the segregated flow solver under the multiphase frame, the stability issues become so significant. The issues become even worse since the complicated physics behind the wall boiling and interphase momentum transfer model are used. To

solve the problems, several efforts are made during the mesh generating and model selecting. With the extreme condition of the geometry (the length of the flow channel is far away larger than the radius), the mesh refinement becomes a challenge for not only stability issues but also for computational cost.

The refinement method in this study is developed with a balance between stability issues and computational cost. However, the results yield to the problems for the application of the grid independent study. A lower limit of the mesh size on the heater and fluid region interface is identified in the convergence study for EMP model. The instability is believed to be contributed from the wall boiling model for the reference bubble departure diameter. Due to the lower limit of the mesh size, the refinement factor for the EMP cases is hardly to satisfy the requirement of the GCI method and, thus, lead to an unreliable result for the grid independent study. However, this is not the case for the VOF model, the convergence study indicates that the VOF model is not highly influenced by the mesh size. With the additional refinement can be applied in VOF cases, the higher refinement factor can obtain and satisfy the requirement for the GCI method, thus, lead to a more reliable result for the grid independent study.

With the result benchmarked, it is confirmed that the VOF model is lacking the ability for performing power transient boiling process. This result is expected since the steady state boiling correlation from Rohsenow's study is adopted for simulating the boiling process. Though the VOF model provides a poor ability of simulating transient boiling, the results provide a good reference for serving as extended steady state boiling curve since Rohsenow's correlation is also commonly used for comparing the transient boiling process with quasi-steady state process in past studies. On the other hand, EMP model provides a reasonable result for not only the transient CHF value but also the entire boiling pattern. Since the simulating geometry performed in this study is based on the simplification of the geometry from TRTL facility, the benchmark is preferred to develope with the experimental result from TRTL facility though TRTL facility is not ready to produce the data for the benchmark during this study is developing.

For a decent choice, the past studies are searched for the benchmark. However, one significant drawback should be noticed is that all the past studies adopt different test metrics. This leads to the fact that an accurate benchmark is impossible and unfeasible. From the view of quasi-steady state, several of the CHF values from different reference, including look-up table, empirical application and CFD simulation, are selected for the benchmark. Though an accurate CHF value is not provided with the different studies, the results shows that, at least, a reasonable CHF for the quasi-steady state boiling is predicted by the Star-CCM+ between 2.0 and 3.0 MW/m^2. From the transient aspect, the benchmark becomes more challenging because of the initial power and heating period are also included into the test metrics. Additionally, the ambiguous information for the test metrics and data series from the past studies lead a more unreliable benchmark. Due to the heat deposit in the heater itself is significantly influenced by the heater geometry, (Bessiron, 2007) may serve as the best choice for the CHF benchmark for the transient cases. Although only an upper limit of CHF about 4.3 MW/m^2 is provided with a higher pressure and inlet subcooling, the result from the simulation which is between 3.6 and 3.8 MW/m^2 provides a good agreement between CFD and experiment.

The boiling pattern from the case with the short heating period perfectly reproduce the phenomenon of the temperature overshoot and a higher CHF value which is commonly observed in the past. It is believed in the past that the OV and a higher CHF value is based on a very different physics which is remaining unknown. Furthermore, the OV is only observed under transient scenario with enough short heating period. The appearance of both OV and higher CHF value from the simulation may indicate that the physics behind the transient boiling may not be so different from the quasi-steady state boiling since current wall boiling model adopted by the CFD software is based on a well understand physics. By the detailed benchmark, a slightly different boiling pattern that is different from most of the early studies is recognized. In fact, the bubble generating for this irregular pattern is observed in some of the early studies, however, for some unknown reasons, the response on the provided boiling curves in not shown. It is believed by the author that this irregular boiling pattern can be related to the HSN mechanism which is first proposed by (ASakurai et al., 1993). On the other hand, (Tachibana et al., 1968) may be the first study

that revealed the existence of HSN or similar mechanism since the boiling curves and event description from Tachibana (1968) are similar to the later studies for the HSN mechanism. Furthermore, a very similar pattern is also developed by the simulation. In the short heating period simulation, the first peak (non-CHF peak) in the boiling curve is typically based on the same physics. This leads to a new hypothesis that the HSN or similar mechanism may not describe a complete process of the transient boiling. Instead, HSN phenomenon may serve as an important role for developing the following higher transient CHF. Based on the new hypothesis that issued in this study, a complete boiling process under transient scenario is very likely to be:

- The fast increasing of the surface temperature (determined by the heat deposition in the heater itself) leads to a fast increasing of the nucleation site number density.

- HSN or similar mechanism is introduced by the bubble crowed before detaching. A temporarily film-like vapor is formed on the heated surface and causes a sudden decreasing of the surface heat flux. All the bubbles remain in their first generation for this stage.

- In some cases, there exist a possibility that all the first-generation bubbles leave the surface almost at same time. The wall temperature, thus, drops due to the rewetting of the heated surface.

- The decreasing of the wall temperature transfers the boiling pattern from the HSN or similar mechanism to the traditional HI mechanism. Thus, the boiling curves shift to the extension of the steady state boiling curve. At same time, the rewetting of the heated surface provides an additional period for the surface heat flux to build-up again and leads to a higher CHF.

It should be noticed that the above-mentioned process is only based on the observation from the simulation and the benchmark according to past studies. A careful and detailed experimental examination is needed for the supporting of the new hypothesis.

5.2 Assumptions and Limitations

The inner iteration of 500 and time step of 1E-4 *s* are chosen for the transient case. These criteria are developed with the stability concern for the simulation with heating period of

50 *ms* which is also the fastest power increasing rate in this study. It is expected that for a shorter heating period less than 50 *ms*, these criteria may no longer appropriate. If a shorter heating period is concerned, the number of the inner iteration should be increased, or the time step should be decreased. On the contrary, for the concern of computation cost, these criteria may be more flexible with longer heating period.

The simulating geometry in this study is based on the simplification of the test section from TRTL facility. Though a simplified geometry is adopted, the stability issue is remaining significant. As a result, an application of complicated geometry is believed to be unfeasible. However, for the purpose of studying transient power increasing, the assumption of simplified geometry is sufficient for the research purpose.

For the models selecting, first, the turbulent model of RKE-2L is selected in this study. Since DES and LES are not considered, the k-ε model is the only turbulent model that suitable due to the stability concern. If the stability issues can be conquered, it is worthy to test the model sensitivity of other RANS model, including k-ω models. Second, for phase momentum transfer, the model for the interaction length scale is selected to be Kurul-Podowski's correlation instead of an additional particle distribution model. The reason is, again, the stability concern. Finally, the same reason is served for the selection of a simpler model set of nucleation site number density and bubble departure diameter model under the frame of wall boiling model.

For some other limitations due to the stability concern, the detail is provided in the chapter of convergence and stability. However, it should be noticed that all the efforts for the stability maintenance are made under with assumption of the shortest heating period which is 50 *ms* in this study. For a shorter heating period, stricter criteria may be necessary.

5.3   Significance of Work

From the CFD view, this study developed a new approach to study the transient power increasing. The approach reflects both the heater and time behavior respect for the transient boiling curve. Moreover, the complete process of a CFD study, including mesh refinement,

model selecting, convergence study and grid independent study, is provided under the frame of EMP model which is notorious for its instability, especially for two-phase simulation. Two of the most challenging factors for the CFD studies, two-phase flow and changing boundary condition, are both included in this study. Thus, the most crucial, this study provide the solutions and criteria to deal with the significant instability accompanying with two-phase flow and changing boundary condition.

From the thermal hydraulic aspect, this study reveals two most significant characteristics for the transient boiling, the temperature overshoot and a higher CHF. The true physics behind these characteristics remain unknown. However, the appearance of both characteristics indicates that the true physics behind may not be so different from the well-known quasi-steady state mechanism. In addition, based on the observations from the simulation and the validation with past experimental studies, a new hypothesis combining with HI and HSN is postulated with the successful explanation of both characteristics. Finally, no matter the hypothesis is proved or not, the results in this study indicate the CFD software of Star-CCM+ do have the ability to predict a reasonable CHF under the frame of the transient boiling.

5.4 Future Work

The validation with the experimental data from the TRTL facility should be the most crucial work for the future. The accuracy of the prediction may directly response, if the CFD study is worthy or not, for the future CFD study developing under the frame of fast power transient including the two-phase flow. If the practicality of the interest region is proved, the further works become there of the follows. First, the application of different test metrics and boundary conditions, including subcooling, pressure and heating period, should be developed for the interest to fill up the missed piece of the past empirical applications. Second, there is an interest to examine the criteria provided for the stability issues in this study are remaining suitable for the different test metrics or not. Third, the sensitivity of different models may be another interest point. Due the stability concern, this study is developed under the simplest and most robust model set. The model sensitivity study may include turbulent models, interphase momentum transfer models, sub-wall

boiling models and particle distribution models. Furthermore, since a new hypothesis is postulated by this study, the examination of the new hypothesis becomes another important future work. If the discussed phenomenon is observed, the missed part of the hypothesis, for example, the mechanism behind the first-generation bubble detachment, would be an interesting topic for the future power transient studies.

6   NOMENCLATURE

6.1   Abbreviation

ASME = American Society of Mechanical Engineering

CFD = Computational Fluid Dynamics

CFL = convective courant number

CHF = Critical Heat Flux

CHT = Conjugate Heat Transfer

CLPHP = Closed Loop Pulsating Heat Pipe

DES = Detached Eddy Simulation

DNB = Departure from Nucleate Boiling

EMP = multiphase segregated flow

FWHM = Full Width Half Maximum

GCI = Grid Convergence Index

HI = Hydrodynamic Instability

HSN = Heterogeneous Spontaneous Nucleation

HPC = High Performance Cluster

INL = Idaho National Laboratory

ITER = International Thermonuclear Experimental Reactor

JFE = Journal of Fluid Engineering

LES = Lage Eddy Simulation

MMP = Eulerian multiphase mixture

NPP = Nuclear Power Plant

ONB = Onset of Nucleate Boiling

OSU = Oregon State University

OV= temperature OVershoot

PWR = Pressurized Water Reactor

RANS = Reynold-Averaged Navier-Stokes

RIA = Reactivity Initiated Accident

TREAT= Transient REActor Test facility

TRTL = Transient Reactor Test Loop

URF = Under Relaxation Factor

VOF = Volume Of Fluid

V&V20 = Verification and Validation in computation fluid dynamics and heat transfer

6.2 Latin Letters

c = Speed of sound

f = Body force

I = Identify tensor

k = Turbulent kinetic energy

Nu = Nusselt number

Pr_c = Prandtl number of continuous phase

Pr_l = Prandtl number of liquid

Pr_t = Turbulent Prandtl number

Pr_α^t = Turbulent Prandtl number against volume fraction

R = Convergence factor

R_{norm} = Normalized convergence factor

Re_d = Reynold number of dispersed phase

Re_w = Wall-distance Reynold number

r = Refinement factor

S = User defined coefficient for transition boiling model

Sc_t = Turbulent Schmidt number

T = Viscous stress tensor

T_t = Reynold stress tensor

T^m = Molecular stress

T^t = Turbulent stress

$\bar{v}$ = mean velocity

v_c = Velocity of continuous phase

v_{cd} = Phase relative velocity

v_d = Velocity of dispersed phase

v_l = Velocity of liquid

v_s = Velocity along stream line

v_v = Velocity of vapor

6.3 Italic Latin Letters

A_v = Effective vapor area

A_w = Effective wetted area

A_{cd}^D = Linear drag coefficient

a = Coefficient of Richardson extrapolation

a_{cc} = Discretized coefficient of current cell

a_{cd} = Interaction area density

a_{nc} = Discretized coefficient of neighbor cell

B = Blended function

C_{a0} = Coefficient used by RKE viscosity coefficient

C_{a1} = Coefficient used by RKE viscosity coefficient

C_{a2} = Coefficient used by RKE viscosity coefficient

C_{a3} = Coefficient used by RKE viscosity coefficient

C_{ew} = Heat flux ratio of vapor generating

C_M = Compressibility modification coefficient

C_p = Specific heat capacity

$C_{p,c}$ = Specific heat capacity of continuous phase

$C_{p,d}$ = Specific heat capacity of dispersed phase

C_{pl} = Empirical coefficient of Rohsenow's nucleate boiling correlation

$C_{qw} =$ Empirical coefficient of Rohsenow's nucleate boiling correlation

$C_{\varepsilon,1} =$ Coefficient used by turbulent dissipation rate transport equation

$C_{\varepsilon,2} =$ Coefficient used by turbulent dissipation rate transport equation

$C_{\varepsilon,2} = C$oefficient used by turbulent dissipation rate production term

$C_{\mu} =$ Viscosity coefficient

$C_{cd}^{D} =$ Standard drag coefficient

$C_{cd,\infty}^{D} =$ Single-particle drag coefficient

$C_{cd}^{L} =$ Lift coefficient

$C_{cd}^{TD} =$ Turbulent dispersion coefficient

$C_{cd}^{VM} =$ Virtual mass coefficient

$C_{max}^{VM} =$ Limited virtual mass coefficient

$C_{sphere}^{VM} =$ Sphere particle virtual mass coefficient

$cc =$ Current cell

$D =$ Test section diameter

$D_{max}^{d} =$ Maximum bubble diameter

$D_{min}^{d} =$ Minimum bubble diameter

$D_{cd}^{TD} =$ Tensor diffusivity coefficient

$d =$ Heater diameter

$d_{he} =$ Heated equivalent diameter, $(D^2 - d^2)/d$

$d_{w} =$ Bubble departure diameter

$d_{0} =$ Reference bubble departure diameter

$E =$ Total energy

$E_{0} =$ Eotvos number

$e =$ Discretization error

$e_{21,ext} =$ Extrpolated discretization error

F_{int} = Internal force

FS = Safety factor

F_{cd}^{D} = Drag force

F_{cd}^{L} = Lift force

F_{cd}^{TD} = Turbulent dispersion force

F_{cd}^{VM} = Virtulal mass force

f_{2} = Turbulent dissipation rate damping function

f_{d} = Bubble departure frequency

f_{μ} = Viscosity damping function

f_{cd}^{D} = Drag force correction

G = Mass flux

G_{b} = Buoyancy production

G_{k} = Turbulent production

GCI_{21} = Fine-grid convergence index

g = Gravitational acceleration

g_{c} = Unit conversion constant

H = Total enthalpy

H_{i} = Inlet subcooling enthalpy

$HTC \times Area$ = Empirical heat transfer coefficient multiplied by interaction area

h_{fg} = Latent heat of vaporization

h_{k} = Representative mesh size of mesh set k

h_{quench} = Quenching heat transfer coefficient

$h^{(cd)}$ = Averaged heat transfer coefficient

h^{ref} = Heat of formation

$h(T_{ij})$ = Evaluated phase interface enthalpy

$I =$ Turbulent intensity

$K =$ Empirical constant of Serizawa's macrolayer dryout model

$K_1 =$ User defined coefficient for transition boiling model

$K_2 =$ User defined coefficient for transition boiling model

$k =$ Linear increasing rate of heatoutput

$k_c =$ Thermal conductivity of continuous phase

$k_{dry} =$ Wall dryout area fraction

$k_{eff} =$ Effective thermal conductivity

$k_{quemch} =$ Bubble influence wall area fraction

$L =$ Length-scale

$L' =$ Dimensionless unit for different geometeries of heater

$l_{cd} =$ Interaction length scale

$l_0 =$ Laplace coefficient, $\{\sigma/[g(\rho_l - \rho_v)]\}^{0.5}$

$l_\varepsilon =$ Length scale function

$M =$ Interphase momentum transfer

$m =$ Mass transfer rate

$\dot{m}_{ec} =$ Mass transfer between phases

$\dot{m}_{ew} =$ Vapor generating mass rate for Rohsenow boiling model

$N =$ Total number of cells

$n'' =$ Nucleation site number density

$nc =$ Neighbor cell of cc

$np =$ Empirical coefficient of exponent of Prandtl number in Rohsenow boiling model

$P =$ power generation

$P_f =$ Formal order of accuracy

$P_k =$ Production term of turbulent kinetic energy

$P_y =$ Observed order of accuracy

$P_0 =$ Initial power

$P_\varepsilon =$ Production term of turbulent dissipation rate

$p =$ Pressure

$Q =$ Heat transfer rate from thermal diffusion

$Q_{max} =$ Maximum heater power

$Q^{ij} =$ Heat transfer rate from boiling

$q'' =$ Wall / surface heat flux

$q''' =$ Volumetric heat generation

$q_0'' =$ Initial surface heat flux

$q_{CHF}'' =$ Critical heat flux

$q_{CHF,f}'' =$ Critical heat flux for infinite flat plane

$q_{CHF,ss}'' =$ Quasi-steady state critical heat flux

$q_{CHF,tr}'' =$ Transient critical heat flux

$\dot{q}_{conv}'' =$ Convection wall heat flux

$\dot{q}_{conv,dry}'' =$ Convection wall heat flux on dryout surface

$\dot{q}_{conv,wet}'' =$ Convection wall heat flux on wetted surface

$\dot{q}_{evap}'' =$ Evaporation wall heat flux

$q_{max}'' =$ User defined maximum heat flux for transition boiling model

$q_{ONB}'' =$ Heat flux for onset of nucleate boiling

$\dot{q}_{quench}'' =$ Evaporation wall heat flux

$q_{Roh}'' =$ Surface heatflux for Rohsenow boiling model

$\dot{q}_w'' =$ Wall heat flux for wall boiling model

$\dot{q}_{w,c}'' =$ Wall heat flux of continuous phase

$\dot{q}_{w,cd}'' =$ Wall heat flux on continuous-dispersed interface

$\dot{q}_{w,d}'' =$ Wall heat flux of dispersed phase

$r =$ Residual of traport equations

$S =$ Mean strain rate tensor

$S^E =$ Energy source

$S^M =$ Phase momentum source

$S^m =$ Phase mass source

$T =$ Temperature

$\bar{T} =$ Mean temperature

$T_c =$ Temperature of continuous phase

$T_d =$ Temperature of dispersed phase

$T_l =$ Temperature of liquid

$T_{HSN} =$ Lower temperature limit of HSN occurrence

$T_{sat} =$ Saturated temperature of water

$T_w =$ Wall / surface super heat

$T_{wall,avg} =$ Averaged wall/surface temperature

$T_c^+ =$ Non-dimensional temperature of continuous phase

$T_d^+ =$ Non-dimensional temperature of dispersed phase

$t_w =$ Waiting time

$t_0 =$ Linear heating period

$u_c^* =$ Reference velocity of continuous phase

$u_d^* =$ Reference velocity of dispersed phase

$V_{heater} =$ Volume of heater

$W =$ Module of mean velocity tensor

$y_k =$ Solution of mesh set k

$y_{21,ext} =$ Extrpolated solution of Richardson extrapolation

$\bar{y} =$ Real solution of infinite refined mesh

6.4 Greek Letters

$\alpha = $ Heat trnasfer coefficient

$\varepsilon = $ Turbulent dissipation rate

6.5 Italic Greek Letters

$\alpha = $ Volume/Void fraction

$\bar{\alpha} = $ Averaged volume/void fraction

$\alpha_c = $ Volume fraction of continuous phase

$\alpha_d = $ Volume fraction of dispersed phase

$\alpha_{dry} = $ Dryout break point

$\alpha_{film} = $ Switching vapor volume fraction of film boiling

$\alpha_{sec} = $ Volume fraction of secondary phase

$\alpha_\delta = $ Bubbly layer thickness

$\gamma_M = $ Compressibility modification

$\Delta T_1 = $ User defined lower tmperature limit for transiton boiling A regime

$\Delta T_2 = $ User defined upper tmperature limit for transiton boiling A regime

$\Delta T_{D,\max} = $ Maximum bubble diameter corresponding liquid subcooling

$\Delta T_{D,\min} = $ Minimum bubble diameter corresponding liquid subcooling

$\Delta T_{\max} = $ Model defined maximum tmperature, $0.5(\Delta T_1 + \Delta T_2)$

$\Delta T_{sub} = $ Temperature subcooling

$\Delta T_{sup} = $ Wall superheat

$\Delta T_0 = $ Temperature subcooling correspinding to reference bubble departure diameter

$\Delta t = $ Temporal gird size

$\Delta V_i = $ Volume of cell i

$\Delta x = $ Spatial gird size

$\delta_c =$ Critical macrolayer thickness

$\delta_m =$ Mean thickness of macrolayer

$\delta_0 =$ Macrolayer thickness

$\varepsilon =$ Inlet subcooling coefficient, $0.00808(\rho_v / \rho_l)^{-1.09}[(H_i - H_{i,40}) / H_i], 40 < \Delta T_{sub} < 70$

$\theta =$ Contact angle

$\lambda_c =$ Critical Taylor wave-length

$\lambda_h =$ Helmholtz wave-length

$\mu =$ Viscosity

$\mu_l =$ Viscosity of liquid

$\mu_t =$ Turbulent eddy viscosity

$\mu_t / \mu =$ Turbulent viscosity ratio

$\nu =$ Kinematic viscosity

$\nu_c^t =$ Turbulent kinematic viscosity in continuous phase

$\rho_c =$ Density of continuous phase

$\rho_d =$ Density of dispersed phase

$\rho_l =$ Density of liquid

$\rho_v =$ Density of vapor

$\sigma =$ Surface tension

$\sigma_k =$ Turbulent kinetic energy coefficient

$\sigma_\varepsilon =$ Turbulent dissipation rate coefficient

$\tau =$ Exponential heating period

$\phi =$ Solution of transport equations

$\varphi =$ User defined coefficient used by transition boiling model

$\omega =$ Under Relaxation Factor

7   BIBLIOGRAPHY

Aoki, S., Inoue, A., &Kozawa, Y. (1974). Transient boiling crisis during rapid depressurization.   Retrieved   from https://inis.iaea.org/search/search.aspx?orig_q=RN:7220316

ASME. (2009). Standard for verification and validation in computational fluid dynamics and heat transfer. *American Society of Mechanical Engineers: New York, NY, USA*.

Bessiron, V. (2007). Modelling of clad-to-coolant heat transfer for RIA applications. *Journal   of   Nuclear   Science   and   Technology*, *44*(2),   211–221. https://doi.org/10.1080/18811248.2007.9711275

Bessiron, V., Sugiyama, T., &Fuketa, T. (2007). Clad-to-coolant heat transfer in nsrr experiments. *Journal of Nuclear Science and Technology*, *44*(5), 723–732. https://doi.org/10.1080/18811248.2007.9711861

CD-adapco. (2018). User Guide: STAR-CCM + v13.02.

CD-adapco, U. (2009). Guide: Star-ccm+. Version.

Celata, G. (1991). CHF behavior during pressure,power and/or flow rate simultaneous variations. Retrieved from https://access.library.oregonstate.edu/pdf/1034842.pdf

Celik, I., Ghia, U., {Engineering, P. R.-J. of fluids, &2008, U. (2008). Procedure for Estimation and Reporting of Uncertainty Due to Discretization in CFD Applications. *Journal of Fluids Engineering*, *130*(7), 78001. https://doi.org/10.1115/1.2960953

Chen, Z. (2009). CFD Investigation in Scale Effects on Propellers with Different Blade Area   Ratio.   *NTNUiA*,   (971),   71.   Retrieved   from https://brage.bibsys.no/xmlui/bitstream/handle/11250/301126/Chen%2C Zicheng_2015.pdf?sequence=1

Cole, R., &R. (1960). A photographic study of pool boiling in the region of the critical heat flux. *AIChE Journal*, *6*(4), 533–538. https://doi.org/10.1002/aic.690060405

Colombo, M., &Fairweather, M. (2016). Accuracy of Eulerian–Eulerian, two-fluid CFD boiling models of subcooled boiling flows. *International Journal of Heat and Mass Transfer*, *103*, 28–44. https://doi.org/10.1016/j.ijheatmasstransfer.2016.06.098

Davis, P. L., Rinehimer, A. T., &Uddin, M. (2012). A comparison of RANS-based turbulence modeling for flow over a wall-mounted square cylinder. *20th Annual*

Conference of the CFD Society of Canada, 8. Retrieved from http://www.sinmec.ufsc.br/~dihlmann/MALISKA/proceedings_cfd_society_of_cana da_conference_may_2012/papers/Davis_Rinehimer_Uddin.pdf

DelValle, V. H., &Kenning, D. B. R. (1985). Subcooled flow boiling at high heat flux. *International Journal of Heat and Mass Transfer*, *28*(10), 1907–1920.

Domalapally, P., Rizzo, E., Savoldi Richard, L., Subba, F., &Zanino, R. (2012). CFD analysis of flow boiling in the ITER first wall. In *Fusion Engineering and Design*. https://doi.org/10.1016/j.fusengdes.2012.01.024

Domalapally, P., &Subba, F. (2015). Computational thermal fluid dynamic analysis of Hypervapotron heat sink for high heat flux devices application. *Fusion Engineering and Design*, *98–99*, 1267–1270. https://doi.org/10.1016/j.fusengdes.2015.02.017

Drew, T., &Muller, A. (1937). Boilng. *Transaction of American Institute of Chemical Engineering*, *33*, 449–471. Retrieved from https://access.library.oregonstate.edu/pdf/1033184.pdf

Ellion, M. E. (1953). A study of the mechanism of boiling heat transfer. Retrieved from https://thesis.library.caltech.edu/1464/1/Ellion_me_1953.pdf

Fukuda, K., Shiotsu, M., Hata, K., &Sakurai, A. (1994). Transient boiling heat transfer from initial steady state caused by rapid depressurization. *Nuclear Engineering and Design*, *149*(1–3), 97–110. https://doi.org/10.1016/0029-5493(94)90277-1

Gaertner, R. F. (1965). Photographic Study of Nucleate Pool Boiling on a Horizontal Surface. *Journal of Heat Transfer*, *87*, 17. https://doi.org/10.1115/1.3689038

Groeneveld, D. C., Shan, J. Q., Vasić, A. Z., Leung, L. K. H., Durmayaz, A., Yang, J., …Tanase, A. (2007). The 2006 CHF look-up table. *Nuclear Engineering and Design*, *237*(15–17), 1909–1922. https://doi.org/10.1016/J.NUCENGDES.2007.02.014

Hall, W. B., &Harrison, W. C. (1966). Transient Boiling of Water at Atmospheric Pressure. In *International Heat Transfer Conference* (pp. 186–192).

Haramura, Y., &Katto, Y. (1983). A new hydrodynamic model of critical heat flux, applicable widely to both pool and forced convection boiling on submerged bodies in saturated liquids. *International Journal of Heat and Mass Transfer*, *26*(3), 389–399. https://doi.org/10.1016/0017-9310(83)90043-1

Hernandez-Perez, V., Abdulkadir, M., &Azzopardi, B. J. (2011). Grid Generation Issues in the CFD Modelling of Two-Phase Flow in a Pipe. *The Journal of Computational Multiphase Flows*, *3*(1), 13–26. https://doi.org/10.1260/1757-482X.3.1.13

Hibiki, T., &Ishii, M. (2003). Active nucleation site density in boiling systems. *International Journal of Heat and Mass Transfer*, *46*(14), 2587–2601. https://doi.org/10.1016/S0017-9310(03)00031-0

Ishigai, S., &Nakanishi, S. (1974). Effect of transient flow on premature dryout in tube. *Dl.begellhouse.com.* Retrieved from http://www.dl.begellhouse.com/download/article/69a588db7fa9fe8a/300-304.pdf

Iwamura, T. (1987). Transient burnout under rapid flow reduction condition. *Journal of Nuclear Science and Technology*, *24*(10), 811–820. https://doi.org/10.1080/18811248.1987.9735884

Jabardo, J. M. S., Silva, E. F.Da, Ribatski, G., &Barros, S. F.De. (2004). Evaluation of the Rohsenow Correlation through Experimental Pool Boiling of Halocarbon Refrigerants on Cylindrical Surfaces. *Journal of the Brazilian Society of Mechanical Sciences and Engineering*, *26*(2), 218–230. https://doi.org/10.1590/S1678-58782004000200015

Johnson, H. A. (1970). Transient Boiling Heat Transfer. *Heat Transfer*, *5*(3.1), 1–11. Retrieved from https://access.library.oregonstate.edu/pdf/1038369.pdf

Kataoka, I., &Serizawa, Akimi, Sakurai, A. (1983). Transient boiling heat transfer under forced convection. *International Journal of Heat and Mass Transfer*, *26*(4), 583–595. https://doi.org/10.1016/0017-9310(83)90009-1

Kim, S. J., Okhuysen, B., Demarly, E., &Baglietto, E. (2016). CFD study of a multi-phase subcooled flow boiling model and the evaluation of the model ' s predictive capability for boiling characteristics. *Nuthos-11*, 1–15.

Krepper, E. (2007). CFD modeling of subcooled boiling - concept, validation and application to fuel assembly design, *237*, 716–731. https://doi.org/10.1016/j.nucengdes.2006.10.023

Kurul, N., &Podowski, M. Z. (1990). Multidimensional effects in forced convection subcooled boiling. In *Proceedings of the Ninth International Heat Transfer Conference* (Vol. 2, pp. 19–24). Hemisphere Publishing New York.

Kutateladze, S. S. (1948). On the transition to film boiling under natural convection. *Kotloturbostroenie*, *3*(152–158), 20. Retrieved from https://ci.nii.ac.jp/naid/10027011442/

Lamb, H. (1945). Hydrodynamics Dover. *New York*, *43*.

Lance, M., &Bataille, J. (1991). Turbulence in the liquid phase of a uniform bubbly air–water flow. *Journal of Fluid Mechanics*, *222*(1), 95. https://doi.org/10.1017/S0022112091001015

Lemmert, M., &Chawla, J. M. (1977). Influence of flow velocity on surface boiling heat transfer coefficient. *Heat Transfer in Boiling*, *237*, 247.

Leung, J. C. M., Gallivan, K. A., Henry, R. E., &Bankoff, S. G. (1981). Critical heat flux predictions during blowdown transients. *International Journal of Multiphase Flow*, *7*(6), 677–701. https://doi.org/10.1016/0301-9322(81)90038-0

Li, Q., Avramova, M., Jiao, Y., Chen, P., Yu, J., Pu, Z., &Chen, J. (2018). CFD prediction of critical heat flux in vertical heated tubes with uniform and non-uniform heat flux. *Nuclear Engineering and Design*, *326*(August 2017), 403–412. https://doi.org/10.1016/j.nucengdes.2017.11.009

Liaw, S.-P., &Dhir, V. K. (1986). Effect of Surface Wettability on Transition Boiling Heat Transfer from a Vertical Surface. *Heat Transfer*. Retrieved from https://access.library.oregonstate.edu/pdf/1036652.pdf

Lienhard, J. H., &Dhir, V. K. (1973). Hydrodynamic prediction of peak pool-boiling heat fluxes from finite bodies. *Journal of Heat Transfer*, *95*(2), 152–158. https://doi.org/10.1115/1.3450013

Lobón, D. H., Valenzuela, L., &Baglietto, E. (2014). Modeling the dynamics of the multiphase fluid in the parabolic-trough solar steam generating systems. https://doi.org/10.1016/j.enconman.2013.10.072

Nagwase, S. Y., &Pachghare, P. R. (2013). Experimental and CFD analysis of closed loop pulsating heat pipe with DI-water. *2013 International Conference on Energy Efficient Technologies for Sustainability, ICEETS 2013*, 185–190. https://doi.org/10.1109/ICEETS.2013.6533380

Nukiyama, S. (1934). The maximum and minimum values of the heat Q transmitted from metal to boiling water under atmospheric pressure. *International Journal of Heat and*

Mass Transfer, *9*(12), 1419–1433. https://doi.org/10.1016/0017-9310(66)90138-4

Pan, C., &Lin, T. (1990). A model for surface wettability effect on transition boiling heat transfer. *Proc. 9th Int. Heat Transfer Conf*, *2*, 147–152. Retrieved from http://www.dl.begellhouse.com/download/article/3f09815c42190ca9/BO-25.pdf

Pan, C., &Lin, T. L. (1991). Predictions of parametric effect on transition boiling under pool boiling conditions. *International Journal of Heat and Mass Transfer*, *34*(6), 1355–1370. https://doi.org/10.1016/0017-9310(91)90280-R

Pasamehmetoglu, K. O., Nelson, R. A., &Gunnerson, F. S. (1990). Critical heat flux modeling in pool boiling for steady-state and power transients. *ASME J. Heat Transfer*, *112*(4), 1048–1057. https://doi.org/10.1115/1.2910477

Povolny, A., &Cuhra, M. (2014). Two-phase CFD of channel boiling for boiling transition problems. *International Conference on Nuclear Engineering, Proceedings, ICONE*, *5*, 1–8. https://doi.org/10.1115/ICONE22-30970

Ranz, W., Prog, W. M.-C. E., &1952, undefined. (n.d.). Evaporation from drops. *dns2.asia.edu.tw*. Retrieved from http://dns2.asia.edu.tw/~ysho/YSHO-English/1000 CE/PDF/Che Eng Pro48, 141.pdf

Richardson, L. F. (1911). The Approximate Arithmetical Solution by Finite Differences of Physical Problems Involving Differential Equations, with an Application to the Stresses in a Masonry Dam. *Philosophical Transactions of the Royal Society A: Mathematical, Physical and Engineering Sciences*, *210*(459–470), 307–357. https://doi.org/10.1098/rsta.1911.0009

Roache, P. J. (1994). Perspective: A Method for Uniform Reporting of Grid Refinement Studies. *Journal of Fluids Engineering*, *116*(3), 405. https://doi.org/10.1115/1.2910291

Roache, P. J. (1998). *Verification and validation in computational science and engineering*. Hermosa.

Rohsenow, W. M. (1951). A method of correlating heat transfer data for surface boiling of liquids. *Mit*, 969–976. Retrieved from http://iibraries.mit.edu/docs

Rosenthal, M. W. (1957). An Experimental Study of Transient Boiling. *Nuclear Science and Engineering*, *2*(5), 640–656. https://doi.org/10.13182/NSE57-A25431

Sakurai, A. (2000). Mechanisms of transitions to film boiling at CHFs in subcooled and

pressurized liquids due to steady and increasing heat inputs. *Nuclear Engineering and Design*, *197*(3), 301–356. https://doi.org/10.1016/S0029-5493(99)00314-3

Sakurai, A., &Shiotsu, M. (1977). Transient pool boiling heat transfer part 1: Incipient Boiling Superheat, *99*(November 1977), 547–553.

Sakurai, A., &Shiotsu, M. (1977). Transient Pool Boiling Heat Transfer Part 2: Boiling Heat transfer and Burnout, *99*(November 1977), 547–553.

Sakurai, A., Shiotsu, M., &Hata, K. (1979). Transient boiling caused by rapid depressurization from initial nonboiling state. Retrieved from https://inis.iaea.org/search/search.aspx?orig_q=RN:12641601

Sakurai, A., Shiotsu, M., &Hata, K. (1993). New transition phenomena to film boiling due to increasing heat inputs on a solid surface in pressurized liquids. In *American Society of Mechanical Engineers, Heat Transfer Division, (Publication) HTD* (Vol. 260, pp. 27–39). Retrieved from https://access.library.oregonstate.edu/pdf/1037559.pdf

Sakurai, A., Shiotsu, M., Hata, K., &Fukuda, K. (1995). Transition phenomena from non-boiling regime to film boiling on a cylinder surface in highly subcooled and pressurized water due to increasing heat inputs. In *American Society of Mechanical Engineers (Paper)*. Retrieved from https://access.library.oregonstate.edu/pdf/1037558.pdf

Sakurai, A., Shiotsu, M., Hata, K., &Fukuda, K. (2000). Photographic study on transitions from non-boiling and nucleate boiling regime to film boiling due to increasing heat inputs in liquid nitrogen and water. *Nuclear Engineering and Design*, *200*(1), 39–54. https://doi.org/10.1016/S0029-5493(99)00325-8

Sakurai, A., Shiotsu, M., &Mizukami, K. (1970). Experimental studies on transient boiling heat transfer and burnout. In *Proceedings of the 4th Intern. Heat Transfer Conference* (Vol. 4, pp. 1–11).

Serizawa, A. (1983). Theoretical prediction of maximum heat flux in power transients. *International Journal of Heat and Mass Transfer*, *26*(6), 921–932. https://doi.org/10.1016/S0017-9310(83)80116-1

Shiotsu, M., Hata, K., &Sakurai, A. (1990). Heterogeneous spontaneous nucleation temperature on solid surface in liquid nitrogen. *Advances in Cryogenic Engineering*, *3*, 437–445. https://doi.org/10.1007/978-1-4613-0639-9_52

Shirvan, K., &Azizian, R. (2015). Simulation of Orientation Effects on Critical Heat Flux in Downward-Facing Channel for Ivr, 8022–8035.

Sontireddy, V. R., &Hari, S. (2017). Sub cooled boiling: Validation by using different CFD models. In *Proceedings - 23rd IEEE International Conference on High Performance Computing Workshops, HiPCW 2016* (pp. 90–99). https://doi.org/10.1109/HiPCW.2016.18

Tachibana, F., Akiyama, M., &Kawamura, H. (1968). Heat Transfer and Critical Heat Flux in Transient Boiling, (I). *Journal of Nuclear Science and Technology*, *5*(3), 117–126. https://doi.org/10.1080/18811248.1968.9732415

Tolubinsky, V. I., &Kostanchuk, D. M. (1970). Vapour bubbles growth rate and heat transfer intensity at subcooled water boiling. In *International Heat Transfer Conference 4* (Vol. 23). Begel House Inc.

Tomiyama, A., Tamai, H., Zun, I., &Hosokawa, S. (2002). Transverse migration of single bubbles in simple shear rows. *Chemical Engineering Science*, *57*, 1849–1858. Retrieved from www.elsevier.com/locate/ces

Torika, K., Hori, M., Akiyama, M., Kobori, T., &Adachi, H. (1964). Boiling Heat Transfer and Burnout mechanism in boiling-water reactor. In *Third UN Int. Conf. On the Peaceful uses of atomic Energy*. Retrieved from https://www.osti.gov/scitech/biblio/4027293

Weatherhead, R. J., &R.J. (1963). *NUCLEATE BOILING CHARACTERISTICS AND THE CRITICAL HEAT FLUX OCCURRENCE IN SUBCOOLED AXIAL-FLOW WATER SYSTEMS*. Argonne, IL (United States). https://doi.org/10.2172/4727562

Weisman, J., &Pei, B. S. (1983). Prediction of critical heat flux in flow boiling at low qualities. *International Journal of Heat and Mass Transfer*. https://doi.org/10.1016/S0017-9310(83)80047-7

Youchison, D. L., Ulrickson, M. A., &Bullock, J. H. (2011). Prediction of Critical Heat Flux in Water-Cooled Plasma Facing Components Using Computational Fluid Dynamics. *Fusion Science and Technology*, *60*(1), 177–184. https://doi.org/10.13182/FST11-A12348

Zuber, N. (1959). *Hydrodynamic Aspects Of Boiling Heat Transfer (Thesis)*. https://doi.org/10.2172/4175511